A design technique for geometric optimisation of resonant coil sizes in low to mid frequency inductive power transmission systems.

HEIDARIAN, M.

2021

A DESIGN TECHNIQUE FOR GEOMETRIC OPTIMISATION OF RESONANT COIL SIZES IN LOW TO MID FREQUENCY INDUCTIVE POWER TRANSMISSION SYSTEMS

Maryam Heidarian

PhD   2021

A DESIGN TECHNIQUE FOR GEOMETRIC OPTIMISATION OF RESONANT COIL SIZES IN LOW TO MID FREQUENCY INDUCTIVE POWER TRANSMISSION SYSTEMS

Maryam Heidarian

A thesis submitted in partial fulfilment of the

requirements of

Robert Gordon University

for the degree of Doctor of Philosophy

in Electrical Engineering

November 2021

To my parents

ACKNOWLEDGEMENTS

TABLE OF CONTENTS

LIST OF TABLES

LIST OF FIGURES

xi

NOMENCLATURE

Abbreviations

ACC	Air-Cored Coil
APT	Acoustic Power Transfer
AUV	Autonomous Underwater Vehicle
AV	Autonomous Vehicle
CPT	Capacitive Power Transfer
EM	Electromagnetic
EV	Electric Vehicle
FCC	Ferrite-Cored Coil
FF-WPT	Far-Field Wireless Power Transfer
FoM	Figure-of-Merit
IMD	Implantable Microelectronic Device
IoT	Internet of Things
IPT	Inductive Power Transfer
KVL	Kirchhoff's Voltage Law
LOS	Line-Of-Sight
LPT	Laser Power Transfer
MPT	Microwave Power Transfer
NF-WPT	Near-Field Wireless Power Transfer
OOK	On-Off Keying
PDM	Pulse Density Modulation
PP	Parallel-Parallel Capacitive Compensation
PS	Parallel-Series Capacitive Compensation
PTE	Power Transfer Efficiency

PZT	Piezoelectric Transducer
RFID	Radio Frequency IDentification
RIPT	Resonant Inductive Power Transfer
RPT	Radiative Power Transfer
Rx	Receiver
Rx-FoM	Receiver Figure-of-Merit
SAR	Specific Absorption Rate
SS	Series-Series Capacitive Compensation
SP	Series-Parallel Capacitive Compensation
Tx	Transmitter
Tx-FoM	Transmitter Figure-of-Merit
UAV	Unmanned Aerial Vehicle
WPT	Wireless Power Transfer
WSN	Wireless Sensor Network

Symbols

α	Higher boundary range around maximum PTE (for air-cored coil)
α_{wf}	Higher boundary range around maximum PTE (for ferrite-cored coil)
β	Lower boundary range around maximum PTE (for air-cored coil)
β_{wf}	Lower boundary range around maximum PTE (for ferrite-cored coil)
c	Speed of light, $= 3 \times 10^8$ m/s
δ	Skin depth/penetration depth
Δ	Efficiency boundary around optimum load resistance
$\eth$	Representative of skin effect losses inside winding wire
η	Power transfer efficiency (for air-cored coil)
η_{wf}	Power transfer efficiency (for ferrite-cored coil)

η_{max}	Maximum achievable power transfer efficiency (for air-cored coil)
$\eta_{max_{\text{wf}}}$	Maximum achievable power transfer efficiency (for ferrite-cored coil)
λ	Wavelength
μ	Magnetic permeability
μ_o	Magnetic permeability of free space, $4\pi \times 10^{-7}$ H/m
μ_r	Relative magnetic permeability
μ'_r	Real component of complex relative permeability
μ''_r	Imaginary component of complex relative permeability
ρ	Resistivity of winding wire material (copper), 1.72×10^{-8} Ω.m
σ	Electric conductivity
φ	Winding distribution over the spiral disk
X	Proximity range around maximum achievable power transfer efficiency
C	Resonant compensation capacitor
C_p	Primary compensation capacitor
C_s	Secondary compensation capacitor
D	Diameter of coil
d_w	Diameter of winding wire
d_t	Distance between the coil windings
f	Frequency of the EM wave emission
f_o	Resonance frequency of an LC tank
i_p	Primary current in time domain
i_s	Secondary current in time domain
$\boldsymbol{I_s}$	Phasor of primary current
$\boldsymbol{I_L}$	Phasor of secondary current
I_s	RMS value of primary current
I_L	RMS value of secondary current
K	Coupling coefficient

L	Coil self-inductance
L_s	Self-inductance of receiver ACC
L_p	Self-inductance of transmitter ACC
L_{wf}	Self-inductance of FCC
l_c	Length of a coil winding
l_{f}	Length of ferrite core
M	Mutual inductance between the coils
N	Number of turns of a coil winding
P_{scf}	Strong coupling factor
Q_i	Intrinsic quality factor of ACC
$Q_{i_{\mathrm{wf}}}$	Intrinsic quality factor of FCC
Q_{i_s}	Intrinsic quality factor of receiver ACC
$Q_{i_{s_{\mathrm{wf}}}}$	Intrinsic quality factor of receiver FCC
Q_{i_p}	Intrinsic quality factor of transmitter ACC
$Q_{i_{p_{\mathrm{wf}}}}$	Intrinsic quality factor of transmitter FCC
Q_L	Loaded quality factor
Q_{L_s}	Loaded quality factor of receiver
Q_{L_p}	Loaded quality factor of transmitter
R	Ac ohmic resistance of air-cored coil
R_{cs}	Ac ohmic resistance of receiver ACC
R_{cp}	Ac ohmic resistance of transmitter ACC
R_{wf}	Parasitic resistance of ferrite-cored coil
R_{f}	Magnetic loss in ferrite core
R_L	Load resistance
R_{L_O}	Optimum load resistance (for ACC)
$R_{L_{O_{\mathrm{wf}}}}$	Optimum load resistance (for FCC)
R_s	Source resistance

r_c	Radius of a coil winding
r_f	Radius of ferrite core
v_s	Source voltage in time domain
v_L	Load voltage in time domain
$\boldsymbol{V_s}$	Phasor of source voltage
$\boldsymbol{V_L}$	Phasor of load voltage
V_s	RMS value of sinusoidal ac source voltage
V_L	RMS value of load voltage
W	Conductor width
ω	Angular frequency, $= 2\pi f$
ω_o	Angular resonance frequency of an LC tank, $= 2\pi f_o$
$\boldsymbol{Z_t}$	Phasor of total impedance

ABSTRACT

Wireless power transfer (WPT) is a well-established method of energising electrically-powered devices. Among the different available WPT techniques Resonant Inductive Power Transfer (RIPT) has been adapted for use in a wide range of applications. The primary reason is the relatively higher Power Transfer Efficiency (PTE) which RIPT can provide. RIPT systems operate on the principle of magnetic resonance coupling between a Transmitter (Tx) and a Receiver (Rx) coil. Maximising the PTE is a key driver for improving the performance of RIPT systems. In a RIPT link the PTE is influenced by three factors: (i) inductive linkage between the Tx and Rx, (ii) terminating circuitry of Tx and Rx sides and (iii) Tx/Rx coil's geometrical size. In considering these impacting factors, different techniques to improve PTE have been extensively presented in the literature and are comprehensively reviewed in this thesis.

The research work undertaken focuses on the geometrical optimisation of Tx/Rx coils to help maximise PTE in RIPT systems for operation over low- and mid-frequency bands (i.e.: between few kHz to several MHz.). Conventional methods for maximising PTE require defining various design parameters (i.e.: figure-of-merits.) which assist in finding the optimum Air-Cored Coil (ACC) geometry. However, traditional techniques for working with Figure-of-Merit (FoM) parameters are very time consuming and process demanding. In this thesis the number of required FoMs have been reduced to one and incorporated into a process to accelerate production of the optimum geometry design. A unique FoM parameter (i.e.: P_{scf}.) is developed by consolidating the PTE's impacting factors.

Considering the RIPT application and its physical size constraints, a proper selection method for identifying the numerical value of P_{scf} is investigated. A novel iterative algorithm has been developed to assist in selection of the most favourable P_{scf} value which provides the optimum ACC geometry. Theoretical design examples of two RIPT systems operating at $10\,\mathrm{kHz}$ (low-frequency band) and $300\,\mathrm{kHz}$ (mid-frequency band) are used to

investigate the functionality of the ACC design approach, for which successful results are achieved. The novel iterative algorithm is also experimentally validated by developing four prototyped Tx/Rx ACC pairs, with real-world applications, which operate over low- and mid-frequency bands: $1.06\,\text{MHz}$, $100\,\text{kHz}$, $50\,\text{kHz}$, $15\,\text{kHz}$. For the designed ACC geometries, maximum PTEs of 85.63% at $1.06\,\text{MHz}$, 83.10% at $100\,\text{kHz}$, 72.85% at $50\,\text{kHz}$ and 34.57% at $15\,\text{kHz}$ are practically measured in bench top tests. The measured PTE values are in close correlation (within 14%) with the calculated PTEs at these frequency ranges, and thus validate the novel ACC design procedure.

The RIPT system's maximum achievable PTE can be further increased by adding ferrite cores to the Tx/Rx ACC pair. In this thesis an advanced iterative algorithm is also presented to support the design of geometrically optimised coil pairs employing ferrite cores. The advanced iterative algorithm is an extension of the initial work on optimising ACC geometries. Optimum Ferrite-Cored Coil (FCC) geometries, produced using the advanced iterative algorithm, for RIPT systems operating at $10\,\text{kHz}$ and $300\,\text{kHz}$ have been investigated. In comparing the FCC and ACC geometries designed for these frequencies, it is demonstrated that RIPT systems with ferrite cores reduce the ACC's geometrical size and additionally improve PTE. To validate the performance of the advanced FCC design algorithm over low- and mid-frequency bands, two RIPT systems are physically constructed for operation at $15\,\text{kHz}$ (low-frequency) and $50\,\text{kHz}$ (mid-frequency). For the prototyped RIPT systems, maximum PTEs of 45.16% at $50\,\text{kHz}$ and 50.74% at $15\,\text{kHz}$ are practically measured. The calculated and physically measured PTE values are within 2% difference; hence validating the advanced FCC design process.

Index Terms: Wireless power transfer (WPT), inductive power transfer (IPT), power transfer efficiency (PTE), resonant magnetic coupling, optimal coil design, electromagnetic induction, near-field power transfer.

CHAPTER 1

INTRODUCTION

1.1 Background

The conventional method of energising electric-driven devices is through a wired connection to a power source. In portable devices wired connection to the electrical supply is not possible and batteries are employed to provide electrical energy. Despite the recent advancement in battery manufacturing technology, such as development of novel energy storage elements and materials, operating battery-powered equipment is often very challenging [1–4]. Batteries do not necessarily have a long operational life and must be regularly recharged and/or replaced. The charging process of batteries is very slow and time consuming. Depending on the device, application and environment, battery replacement can also impose a great difficulty. For example, in a gastrostimulator implant the batteries must be changed every 3 to 5 years through major invasive surgery that lasts 2 to 4 hours [4]. In addition to this, batteries have a very limited energy storage capacity (i.e.: energy density.). For example, a Lithium-ion battery pack, which is commonly used to power up electric vehicles (EVs), has energy density of 90–100 watt-hour per kilogram (Wh/Kg) and can run less than 220 kilometres per charge [5]. To extend the electric vehicle's driving range per battery charge, the quantity of the batteries installed on the EV must be significantly increased [1]; which increases weight, size and the associated costs [2]. Wireless power transfer (WPT) is the promising alternative to address problems that come with traditional methods of energising stationary and mobile electric equipment.

History of WPT dates back to 1862 when James Clerk Maxwell provided mathematical equations for electromagnetic (EM) waves and fields following Ampere's circuit law and Faraday's law of induction [6]. Later in 1888, Heirich Rudolf Hertz, by investigat-

ing and confirming Maxwell's prediction on EM wave propagation (known as Maxwell's equations), paved the way for practical use of electromagnetic waves [2]. The initial idea of transmitting power using EM waves was empirically pursued by inventors including Nikola Tesla, Hutin and Leblance in 1890s [6, 7]. Among them, Tesla's experiments on wireless power transmission made the most profound impact on today's WPT systems [2, 3, 6–8]. However, Tesla's innovative efforts could not last longer than 1900s due to lack of financial support and interest in cordless delivery of electrical energy [7]. Also, the equipment and technology required for Tesla's investigations were not developed back in the early 20th century [6–8].

In the late 1950s, development of advanced semiconductors and modern power supplies eased the WPT investigations pioneered during Tesla's era [8]. With technological enhancement the demand for cordless delivery of electrical energy also gradually increased. Over the last few decades, WPT has emerged as an ideal solution for operations in hostile and inaccessible locations. For example in industrial manufacturing sectors many hazardous operations, due to the environment and safety concerns, must be kept inside sealed and insulated metallic containers to avoid leakage of internal fluid, gas, substances, etc. Safe management of tasks inside such metallic enclosures demands the ability to remotely monitor and control the operations from outside. In addition to this, regular structural health monitoring of enclosures and housing is necessary to ensure the insulator's reliability and safety. To evaluate both the internal operational process and the armour's structural condition in a sealed metallic container different types of inspection equipment, based on requirements, will often be deployed inside the enclosure [9]. For instance, two typical sensing applications used for monitoring purposes are shown in Fig. 1.1. A passive radio frequency identification (RFID) transponder is shown in Fig. 1.1a, which measures the pressure and temperature inside a sealed metallic whipped cream device [10]. Fig. 1.1b shows optical sensor arrays installed on pipe inspection robots travelling in an oil and gas pipeline to monitor the pipe's structural health and defects [11]. Wired power delivery to
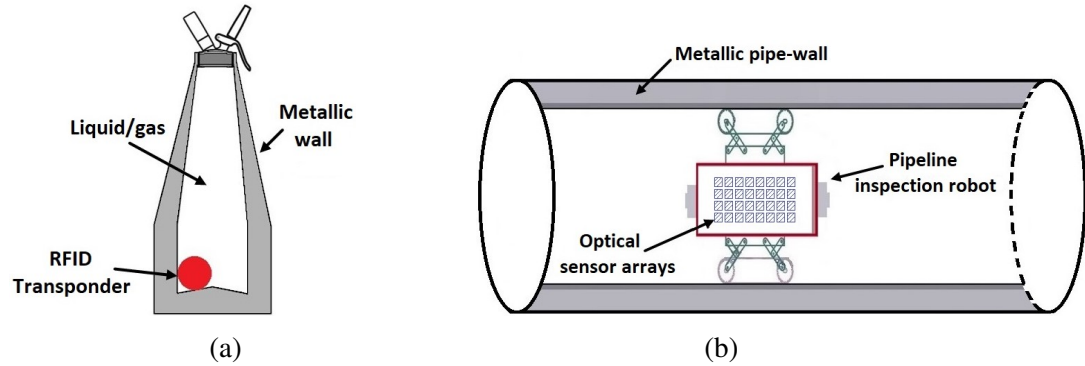
Figure 1.1: Examples of sensing equipment to monitor inside the metallic enclosures: (a) RFID transponder, (b) optical sensor array.

such remote sensing/monitoring systems enclosed in metallic containers requires perforation in the armour. This method can endanger the strength and structural integrity of the insulator housing and may lead to release of internal material to the surrounding environment. Using replaceable battery packs to power such systems is not feasible in many cases due to the need to unseal housings/enclosures, which can be time consuming, costly and possibly dangerous. The requirement for an effective method of energising such enclosed electric-driven devices in a manner which maintains the structure's integrity makes wireless power transfer a viable solution.

WPT systems operate based on a similar mechanism used for wireless signal communication; hence, they can be used to transmit information signal to out-of-reach areas as well as power. Considering these, wireless power transfer can benefit an extremely diverse range of applications including:

- Energising portable electronic consumers (i.e.: low power charging.) such as smartphones [12], cameras, laptops [13] and electric toothbrush as shown in Fig. 1.2a [14];

- Power and signal delivery to/from sensors and RFID tags located within harsh environment, automotive manufacturing industries and clean factories. For example, underwater surveillance sensor networks, underground sensor networks located within

mining tunnels, condition monitoring sensors in food containers [15], seismic activity sensors integrated in building walls [16], wireless sensor networks (WSN) in pipeline environment [17], sensor-based internet of things (IoT) and smart homes appliances as shown in Fig. 1.2d [14];

- Dynamic and/or stationary wireless charging of batteries in transportation vehicles (i.e.: high power charging.) such as electric cars, as shown in Fig. 1.2b [2, 18, 19] and public transport buses, as shown in Fig. 1.2c [20–22];

- Wireless power and signal transmission to autonomous vehicles such as unmanned aerial vehicles (UAVs) [23] and autonomous underwater vehicles (AUVs) [24];

- Cordless energy delivery to/from rotating equipment such as well drilling tools [25] and wind turbines [26];

- Wireless power and data transfer to mobile robots such as pipeline inspection robots [9] and endoscope micro-robots (capsule robots) [27];

- Powering and signal transfer to biomedical implants such as gastrostimulator implants [4], retinal prostheses capable of measuring intraocular pressure [28, 29], cochlear implants [30], brain-computer interfaces and neuroprosthesis [31], drug delivery and cardiac pacemakers [32];

- Power and data transmission to/from wearables such as smart shoes, wearable electrocardiograms, health monitoring watches and smart orthopaedic patches [33, 34], etc.

Over the last century different approaches have been adapted to wirelessly transmit electrical energy from a power source (i.e.: transmitter, Tx.) to an electric load (i.e.: receiver, Rx.). WPT techniques, with respect to the transmission distance between the Tx and Rx, can be divided into two categories: far-field (FF-WPT) and near-field (NF-WPT) [1, 3, 7, 13, 14]. To transmit power over a long distance, far-field WPT relies on EM wave radiations

(a)   (b)

(c)   (d)
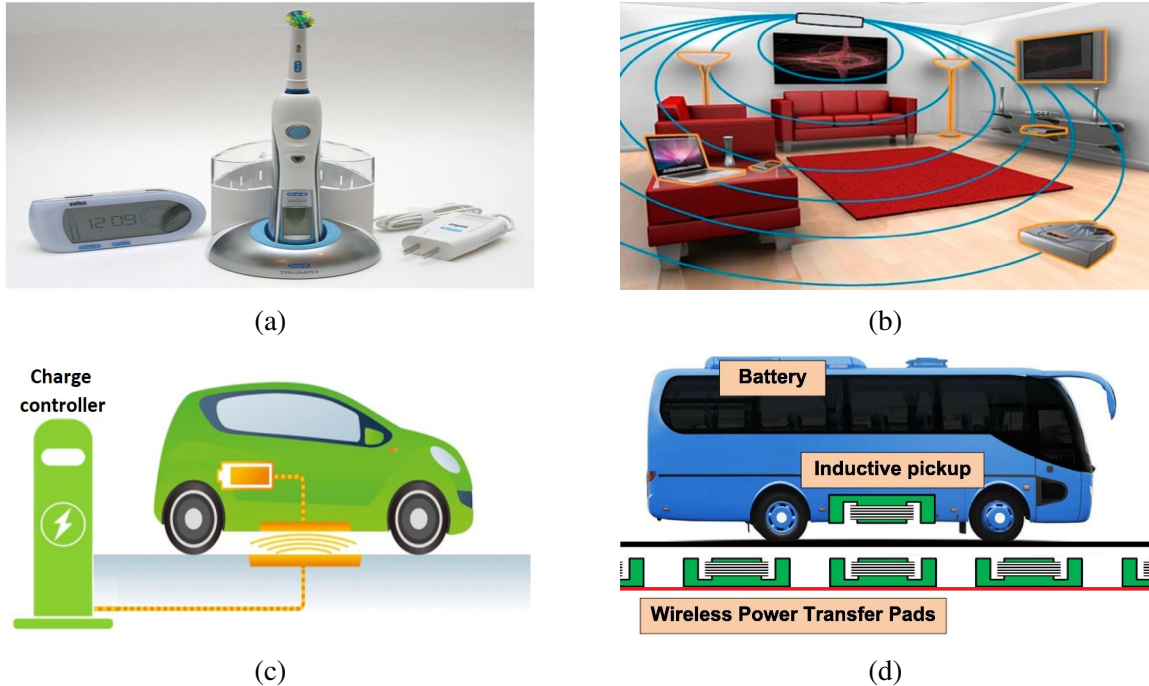
Figure 1.2: Typical WPT applications: (a) powering an electric toothbrush [14], (b) wireless power delivery to smart home appliances [14], (c) stationary wireless charging of batteries in an EV [19], (d) dynamic wireless charging of batteries in a bus [22].

which exist in the microwave frequency spectrum and higher (i.e.: mostly $> 300\,\mathrm{MHz}$.) [7, 35]. The electromagnetic radiations, especially at high frequency ranges, potentially have damaging effect on biologically live tissues including human tissues. Based on safety regulations the transmission power level in the FF-WPT systems must be kept below a few hundred mW [3, 7, 35], unless the power is being transmitted between human-free zones such as space and isolated locations [7, 36]. Considering this, far-field WPT is not a suitable technique for the majority of wireless power transfer applications [7, 14].

Near-field WPT refers to short- and mid-range (i.e.: power transmission distance $\leq$ several times of the dimension of the transmitter structure [6, 8].) cordless delivery of electrical energy. In this technique, the system operating frequency is mostly at megahertz or sub-megahertz range [37]. For short- and mid-range energy delivery, power can be transmitted through sound vibrations, electric field coupling, magnetic field coupling and magnetic resonant coupling between the Tx and Rx [3, 36]. Among the NF-WPT techniques, magnetic

resonant coupling (i.e.: resonant inductive power transfer, RIPT.) can provide the highest power transfer efficiency (i.e.: the ratio of power received at the electric load to the power level driving the Tx.) [8, 14, 21, 36]. Hence, RIPT has been extensively adapted as an ideal solution for diverse short- and mid-range wireless power delivery applications [8, 38].

1.2 Problem Statement

Resonant inductive power transfer is a well-established WPT method. The operation principle of this wireless power transfer technique is based on resonant coupling of a magnetic field between a primary and a secondary coil. The key performance parameter in development work on RIPT systems is power transfer efficiency (PTE). PTE in a RIPT system is affected by transmission medium, terminating circuitry of both receiver and transmitter, and coil size (i.e.: diameter, length and number of turns.). In the bulk of WPT systems, the transmission medium and its influence on PTE is an intrinsic feature of the application which cannot be modified. The Tx and Rx terminating circuitries also are mainly affected by the application's required power level. Considering these factors, coil geometry optimisation is an essential requirement for designing an efficient power transfer link [30–32, 39–44].

The resonant inductive power transfer systems usually operate at low- and mid-frequency ranges (i.e.: $<$ a few MHz.) in the EM wave spectrum [8, 12, 21, 35]. The system's operating frequency strongly impacts the Tx/Rx coil geometry. Based on the fundamentals of antenna design theory in an efficient power transmission system the dimensions of Tx/Rx coils must be comparable with the operating EM wavelength frequency [14, 31, 45]. The wavelength (λ), based on [46], can be calculated as:

$$\lambda = \frac{c}{f} \tag{1.1}$$

in which c is the speed of light ($c = 3 \times 10^8$ m/s) and f is the frequency of the EM wave

emission. Considering this, having an efficient RIPT system, which is operating at low- and mid-frequency bands, requires physically large Tx/Rx coils. It should be noted that physically large coils have higher internal resistance which significantly increases the amount of power loss (in the form of heat) inside the coil [14, 30–32]. A high level of power loss in Tx and Rx coils does reduce the power level that can be delivered to the load; thus leading to low PTE in these systems. Considering the challenges associated with operating resonant inductive power transfer systems, improving PTE necessitates optimising the Tx/Rx coil geometry [30–32, 39–42].

In addition to improving PTE, coil geometry optimisation by miniaturising the system's overall design can extend the range of existing wireless power transfer applications. Coil geometrical optimisation lends itself well to WPT applications where the physical size of a transceiver is limited; such as contact-less power delivery through metallic pipes [3, 9] and IMDs [30, 31, 42]. In cordless power delivery to IMDs, a miniaturised coil geometry can also reduce the implant's harmful impacts on the tissue, which typically includes potential cell death, inflammation and damage to blood vessels near the implant site [31]. Miniaturised coil geometries can also pave the way for new WPT applications. For example, currently wireless power delivery to dynamic vehicles is limited to public transportation systems such as buses. This is due to high expenses associated with massive road excavations which are required to bury physically large coils. Employing smaller coils by reducing the volume of excavations and the associated costs can promote the use of WPT in dynamic EVs as well.

1.3 Aim and Objectives

The aim of this research work is to develop a comprehensive technique to design the optimum coil geometry which can maximise overall PTE in the RIPT systems operating over low- and mid-frequency bands. Geometrical optimisation of Tx/Rx inductive coils, with the purpose of maximising PTE, has been well researched over the last few decades. An exten-

sive review of these methods can be found in this thesis. To improve PTE, the traditional geometry design techniques focus on increasing the intrinsic quality of the Tx/Rx air-cored coil (ACC) pair, by modifying the coil's winding layout. Employing a high quality Tx/Rx ACC pair can improve the energy transmission between the pair, however maximising the RIPT system's source-to-load PTE requires compensating the loading effects of the Tx and Rx concurrent with configuring the coil's geometry.

With the motivation to maximise the RIPT system's source-to-load PTE, different ACC geometry design algorithms have been reported in the literature. As a common approach in these techniques, first the system's overall PTE is formulated as an equation. Then based on the derived equation, various design parameters (i.e.: figure-of-merit parameters.) are defined to help improve PTE. In these techniques, designing the optimum ACC geometry requires determining proper numerical values for the set of figure-of-merit (FoM) parameters. It will be shown in this thesis that depending on the number of required FoMs, the available geometry design algorithms are very time consuming.

Building upon the previous techniques, the motivation for this research study is to accelerate the geometry design procedure by reducing the number of FoM parameters to one. Determining this unique FoM parameter requires a comprehensive analysis of the RIPT system and the physical factors which impact PTE. In the present thesis, a unique FoM parameter (called P_{scf}) is developed by combining PTE's impacting factors. Considering the RIPT application and its physical size constraints, a proper selection method for identifying the numerical value of P_{scf} is essential to design the optimum ACC geometry. Finding the most favourable value for the developed FoM parameter demands investigating the effect of P_{scf} on the coil's geometrical size. Considering these requirements, in this thesis a novel iterative algorithm is developed to assist in selecting the most favourable P_{scf} value. The established design algorithm, through selecting the proper P_{scf} value, will provide the optimum Tx/Rx ACC geometry.

In a RIPT link, maximum achievable PTE is affected by the system application and

its spatial limitations. Ferrite cores have been widely added to the Tx/Rx coil pairs in the RIPT systems to boost PTE [18, 21, 27, 44, 47–54]. In a RIPT system with the Tx/Rx ferrite-cored coils (FCC), PTE is affected by ferrite's magnetisation and demagnetisation effects [27, 31, 55]. Ferrite's magnetisation effect improves the inductive link's PTE [27, 55–58], while its demagnetisation effect reduces PTE [27, 50, 55, 58, 59]. Considering these effects, the main challenge in utilising ferrite cores is to design a geometry which can increase the system's PTE level. With a motivation to further increase PTE in the RIPT links, this research work aims to design geometrically optimised Tx/Rx FCC pairs.

Designing the optimum FCC geometry demands studying the coil's analytical model. Investigating the analytical model indicates that having the optimum FCC geometry requires a geometrically optimised winding (i.e.: air-cored coil.). It will be shown in this thesis that designing the optimum FCC also necessitates to verify if adding a ferrite core to the optimum winding geometry can yield an improvement in PTE. A common technique in the literature to design a geometrically optimised FCC is to initially find the optimum coil winding (i.e.: ACC geometry.) and fill the winding with a ferrite core. The developed FCC geometry then must be modified to ensure it can provide the maximised PTE. Following this approach, in the present research work an advanced iterative algorithm is developed based on the novel ACC design algorithm, which is established in this thesis. The advanced iterative design algorithm, through selecting the most proper numerical value for P_{scf}, provides the optimum Tx/Rx FCC geometry which can maximise PTE with respect to the ferrite's magnetisation and demagnetisation effects.

Two coil topologies commonly used in RIPT applications are spiral and helical inductors. The available coil design algorithms in the literature mainly focus on optimising spiral coils or low power (i.e.: $\ll 1\,\text{W}$.) mm-sized helicals. However, geometrical optimisation of regular-size helicals can be equally important. To fulfill this research gap, in the present thesis the iterative design algorithms (i.e.: for the air-cored and ferrite-cored coils.) are developed through geometrical optimisation of solenoids (i.e.: a type of helical coils.). The

ACC and FCC design algorithms in this research work can be employed in high-power (i.e.: $\geq$ several hundred mW.) RIPT systems as well as low-power applications.

Validating a coil geometry design technique necessitates developing a PTE measurement setup with Tx/Rx coils that are constructed based on the proposed iterative algorithm. For this purpose, in the present research work various air-cored and ferrite-cored solenoids have been constructed based on the developed novel ACC geometry design algorithm and advanced FCC design algorithm, respectively. Close correlations between the experimental and calculated PTE measurements validate the developed design techniques.

1.4 Contributions

Main novelties and contributions to knowledge in this research work are:

1) The process of designing the optimum Tx/Rx coil geometry is accelerated by developing a unique FoM parameter. The previously reported geometry design algorithms mainly require determining numerous FoM parameters to assist in improving the RIPT system's PTE. In this research work a new design parameter (i.e.: P_{scf}.) is defined which enables reducing the number of required FoMs to a single factor.

2) A novel iterative algorithm is developed to design the optimum Tx/Rx air-cored coil geometry which can maximise PTE for the required RIPT application. The key novelty of this technique is that the provided design algorithm requires determining the numerical value of a single FoM parameter, which is called as strong coupling factor (P_{scf}). A coil geometry design algorithm based on such unique FoM parameter has not been reported previously in the literature on coil geometry optimisation techniques.

3) An advanced recursive algorithm is provided to design the optimum Tx/Rx ferrite-cored coil geometry which can boost PTE. In RIPT systems, that are operating over low- and mid-frequency bands, achieving maximised PTE requires significantly large

coil geometries, which are not feasible in many applications. The advanced FCC design algorithm is developed based on the novel ACC design approach and can further improve PTE in RIPT systems with restrictive spatial limitations.

4) The developed iterative algorithms in this research work provide the optimum Tx/Rx solenoid geometries that can increase PTE in high-power RIPT applications as well as low-power systems.

5) In this thesis to validate the developed iterative algorithms, various design examples have been selected from real-world RIPT applications. These examples showcase the ability of the provided geometry design techniques in benefiting industrial RIPT systems by reducing their physical size and maximising PTE.

1.5 Resulting Publications

Contributions to journal articles

1) M. Heidarian and S. J. Burgess. "A Design Technique for Optimizing Resonant Coils and the Energy Transfer of Inductive Links". In: IEEE Transactions on Microwave Theory and Techniques 69.1 (2021), pp. 399–408.

2) M. Heidarian and S. J. Burgess. "A Design Technique for Optimizing Ferrite-cored Coils and the Energy Transfer of Resonant Inductive Links". Under preparation to submit to IEEE Transactions on Industrial Electronics.

Contributions to conference proceedings

1) M. Heidarian, S. J. Burgess, and R. Prabhu. "Improving the Design Approach to Developing Through-Metal Communications for Use in Subsea Pipeline Robots". In: Global Oceans 2020: Singapore – U.S. Gulf Coast. 2020, pp. 1–5.

2) M. Heidarian et al. "Maximising Inductive Power Transmission using a Novel Analytical Coil Design Approach". In: 2019 IEEE Wireless Power Transfer Conference (WPTC). IEEE. 2019, pp. 158–161.

3) M. Heidarian et al. "Optimal Coil Design for Maximum Power Transfer Efficiency in Resonantly Coupled Systems". In: 2019 USNC-URSI Radio Science Meeting (Joint with AP-S Symposium). IEEE. 2019, pp. 73–74.

1.6   Thesis Outline

The rest of this thesis is organised as follows:

Chapter 2 provides an extensive overview of WPT techniques from the perspective of power transfer efficiency and feasibility for implementation in wide range of applications. Resonant inductive power transfer is shown to provide the highest PTE level for a wider range of WPT applications. The key performance parameter in development work on RIPT systems is maximising PTE. In this chapter the available techniques to increase PTE in resonant inductive links are comprehensively reviewed. Among the available methods, geometrical optimisation of Tx/Rx coils is presented as the essential requirement to maximise PTE. A comprehensive literature survey on coil geometry optimisation methods is also provided in this chapter.

Chapter 3 discusses the requirements for maximising PTE in the RIPT system. In this chapter the theoretical model of a resonant inductive link with Tx/Rx air-cored coils is expressed to assist formulating PTE. Based on the derived PTE equation the physical parameters affecting maximised inductive linkage between the Tx and Rx are identified. Through theoretically analysing the PTE's impacting factors a new FoM parameter (i.e.: P_{scf}) is developed to maximise the RIPT system's PTE.

Chapter 4 analyses the effects of P_{scf} parameter on the RIPT system and the Tx/Rx coil's geometrical dimension. Based on these investigations a novel recursive algorithm is developed to design the geometrically optimised Tx/Rx ACC pair which can maximise PTE.

This chapter also demonstrates functionality of the developed novel iterative ACC design algorithm by optimising the coil geometries for various real-world RIPT systems operating over low- and mid-frequency bands. The practical PTE measurements of the exemplified RIPT systems are also presented to validate the optimum ACC geometry design procedure. **Chapter 5** presents the effects of adding ferrite cores to the Tx/Rx coils on the RIPT system's PTE. Considering these effects an advanced iterative algorithm is developed to design the optimum Tx/Rx FCC geometry which maximises PTE. In this chapter functionality of the developed advanced iterative algorithm is demonstrated by optimising the FCC geometries for various RIPT systems with industrial applications. The FCC geometry design technique is also validated with practical measurements of PTE in the RIPT systems operating over low- and mid-frequency bands.

Chapter 6 summarises contributions to knowledge and main findings of this research work. It also includes suggestions on future work in RITP and promoting further WPT applications.

CHAPTER 2

LITERATURE REVIEW

This chapter provides an overview of the available WPT approaches and presents resonant inductive power transfer as a contact-less energy delivery technique suitable for a wide range of near-field applications. Maintaining maximum power transfer efficiency is one of the main challenges in resonant inductive WPT systems. Reviewing the available methods to improve PTE in RIPT systems highlights the need for designing an optimum coil geometry to maximise PTE. This chapter ends with reviewing the available geometry optimisation techniques which maximises PTE in the RIPT systems.

2.1   Wireless Power Transfer Techniques

Wireless power transfer refers to cordless delivery of electrical energy from a power source to a target electric load. WPT methods, with respect to the power transmission distance between the transmitter and receiver, are commonly classified as two cordless power transmission approaches [1–3, 8]: *a) near-field*, and *b) far-field* energy delivery techniques.

2.2   Far-field Power Transmission

Far-field power transfer is the long-range power delivery approach where the distance between the transmitter and receiver is far greater than a wavelength (in meters) [46, 60]. FF-WPT employs electromagnetic fields emitted from a radiating structure (i.e.: transmitting antenna.) to deliver energy to an electric load (i.e.: receiving antenna.) [3, 7, 8, 35, 36]. Hence, far-field WPT is also called radiative power transfer (RPT) [7, 8]. It should be noted that the underlying mechanism used for RPT is similar to the technique deployed for transmitting information signals via EM waves [3].
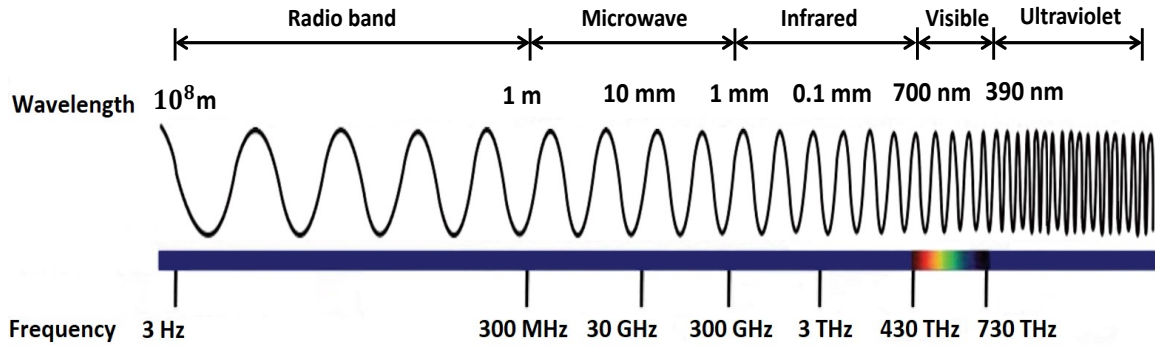
Figure 2.1: Electromagnetic wave spectrum, adapted from [61].

Radiative WPT can be further classified as two techniques [3]: *I) microwave power transfer*, and *II) laser power transfer*.

2.2.1 Microwave Power Transfer

Microwave radiations as an energy carrier were initially used by William C. Brown to propel a model helicopter in 1963 [7]. As can be deduced from Fig. 2.1, the electromagnetic waves involved in microwave power transfer (MPT) are mainly in GHz frequency range [2, 3, 7, 14, 35]; enabling cordless energy transmission to locations up to several kilometers away from the Tx location. In this far-field WPT technique either omni- or uni-directional patterns can be employed to radiate the Tx antenna in the microwave frequency band [3].

Omni-directional MPT can benefit simultaneous power delivery to multi-receivers such as low-power wireless sensor networks (WSNs) [3, 7] and sensor-based IoT applications [35]. However, this wireless power transfer technique suffers from low PTE [7]. The low PTE in the omni-directional MPT is due to the isotropic nature of the transmission pattern which yields the majority of power to be wasted in the antenna's surrounding environment [3, 7, 35]. High PTE can be achieved using uni-directional MPT; however, it requires sophisticated wave tracking techniques [3, 35, 62]. A typical application of uni-directional MPT is space solar power transfer [3, 7]. In these systems space satellites, carrying massive solar panels as shown in Fig. 2.2, are used to convert solar energy to microwave radiations

Figure 2.2: Solar panels mounted on a space satellite to transmit microwave power to earth.

before transmission to dedicated receivers on earth. Uni-directional MPT has been also used to energise unmanned aerial vehicles flying above the ground-based transmitter [23].

A major concern in WPT systems is related to human exposure under electromagnetic fields and specific absorption rate (SAR) [3, 8, 13, 14, 31]. SAR is a ratio to measure the power level that is absorbed by a biological tissue. High-power electromagnetic waves with a short wavelength can have adverse effects on biologically live tissues. In compliance with radio frequency (RF) exposure regulations, such as IEEE guidelines as shown in Fig. 2.3 [63], the required power level in WPT applications must be limited to less than $1\,\mathrm{mW/cm^2}$ [3, 63]. A typical example of such systems are MPT to miniature UAVs with mW power requirements [3]. The applications which require higher power transmission levels must be kept in human-free zones (e.g.: space, offshore installations, isolated islands, desert areas, mountains, etc.) [3, 7, 8].

In addition to this, high power MPT systems require physically large antennas to transmit energy over a long distance [14]. Such wireless power transfer systems are highly expensive and can be afforded only in military and terrestrial projects where cost is not an issue [3, 7, 14, 35]. One of the earliest high-power MPT demonstrations is NASA JPL (Jet Propulsion Laboratory) project in which microwave radiations at $2.39\,\mathrm{GHz}$ were used to transmit $32\,\mathrm{kW}$ power over a mile range at Raytheon in 1975 [23].
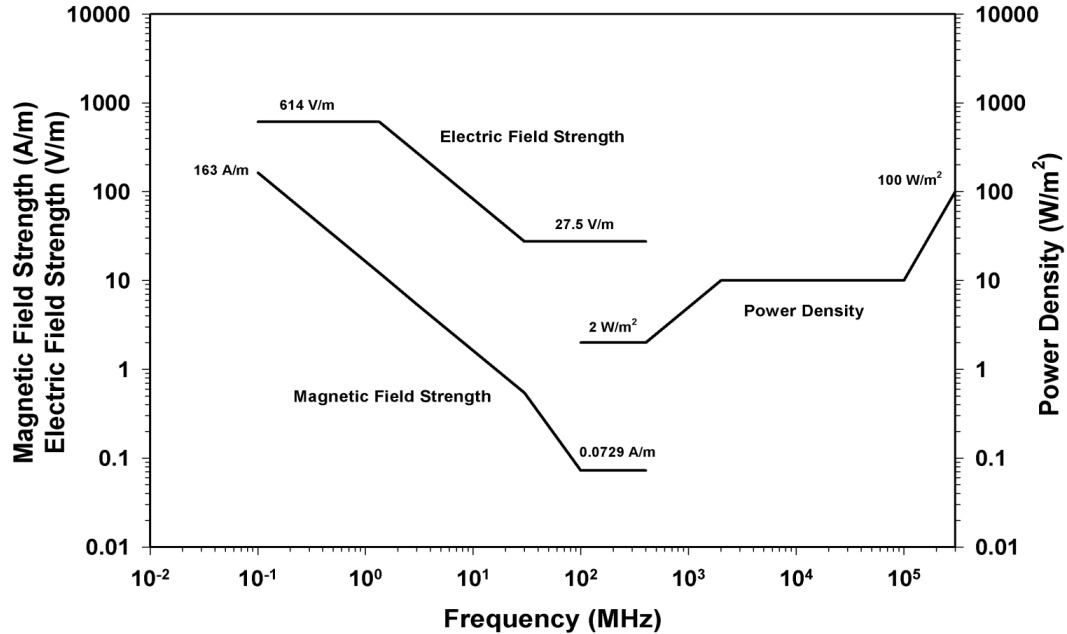
Figure 2.3: IEEE reference level for maximum permissible exposure to electromagnetic fields [63].

2.2.2 Laser Power Transfer

Light amplification by stimulated emission of radiation is commonly known as laser [64]. Laser power transfer (LPT) employs radiations of EM waves, which are lying in the visible or near infrared frequency spectrum, as the energy carrier [3, 64]. This frequency spectrum starts from several THz to several hundred THz, as can be seen in Fig. 2.1. Similar to MPT, laser power transfer can be used to deliver electrical energy over a long range. However, LPT highly relies on uninterrupted line-of-sight (LOS) path between the transmitter (i.e.: laser beam.) and the receiver [3, 62, 64]. Considering this requirement, the LPT applications are mainly limited to power delivery to UAV applications which can ensure an uninterrupted LOS [3, 36]. A typical laser power transmission to UAVs is demonstrated in Fig. 2.4 [14]. Here two Tx laser beams have been located in two different geographical positions. Depending on the UAV's location and battery availability, the aerial vehicle will be guided to any of the two Tx laser beams which are in a closer location, and an uninterrupted LOS connection will be made for battery recharge purposes.

17
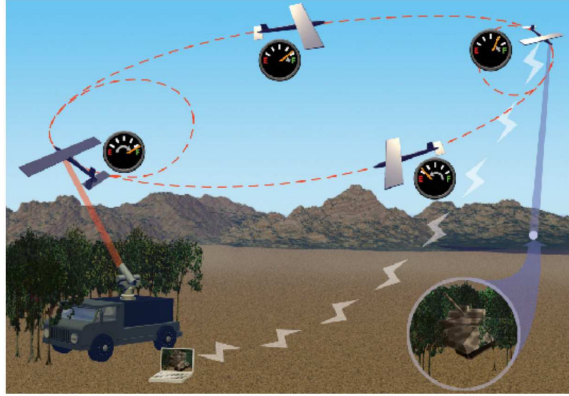
Figure 2.4: Laser power transmission to energise an UAV, adopted from [14].

2.2.3 Discussion

The radiative power transfer is suitable for energy delivery over a long distance. However, far-field WPT has very limited applications, which is due to the difficulties associated with adapting this technique. These problems can be briefed as:

- Demanding uninterrupted LOS path.

- Having low PTE due to multi-path fading.

- Potential damaging effect on biologically live tissues (including human) near the Tx/Rx system.

- Requiring sophisticated wave tracking techniques at the receiver.

- Having a significantly large physical size (especially at the transmitter).

- High associated expenses.

In addition to these, the employed frequency spectrum in far-field WPT (i.e.: $> 300\,\mathrm{MHz}$.), based on (1.1), has a very short wavelength; hence, is not suitable for propagation through highly conductive media (e.g.: seawater, steel, aluminium, etc.) [3, 35]. Considering these, radiative WPT is not adequate for most cordless power delivery applications [14,

35], including energising commercial applications (i.e.: everyday consumer electronics.), IMDs, WPT through metallic housing and concrete structures, EVs, etc.

2.3 Near-field Power Transmission

Near-field WPT relies on non-radiative coupling between a power transmitter and an electric-driven load, both of which are located within a wavelength from each other (i.e.: the distance between the Tx and Rx is smaller than one wavelength at the operating frequency [7, 35, 46].). Hence, NF-WPT is also known as non-radiative power transmission. The non-radiative nature of near-field wireless power transfer enables this technique to provide high power transmission levels without requiring uninterrupted LOS or suffering from multi-path fading. Non-radiative WPT systems typically operate at low- and mid-frequency ranges, between few kHz to several MHz [7, 8, 12, 21, 35]. Operating in such frequency bands, reduces the power absorption inside the transmission medium [7, 9, 32]; hence, making NF-WPT an ideal solution for cordless energy delivery through a variety of obstacles such as building walls, metallic chambers, seawater, etc.

Near-field wireless power transmission can be further classified as four techniques [3]: *I) acoustic power transfer*, *II) capacitive power transfer*, *III) inductive power transfer*, and *IV) resonant inductive power transfer*.

2.3.1   Acoustic Power Transfer

Acoustic power transmission (APT) systems employ sound vibrations, typically in the frequency range 0.5–2.25 MHz, as the energy carrier for near-field cordless power delivery [65]. In an APT system, as demonstrated in Fig. 2.5, a piezoelectric transducer (PZT) transforms the electric energy of the power supply into the sound's vibrational energy to propagate inside the medium between the Tx and Rx (e.g.: air, human tissue and metal.). At the receiver side the Rx piezoelectric transducer will be positioned along the path of the sound wave to convert the received energy back to electricity [36, 65].
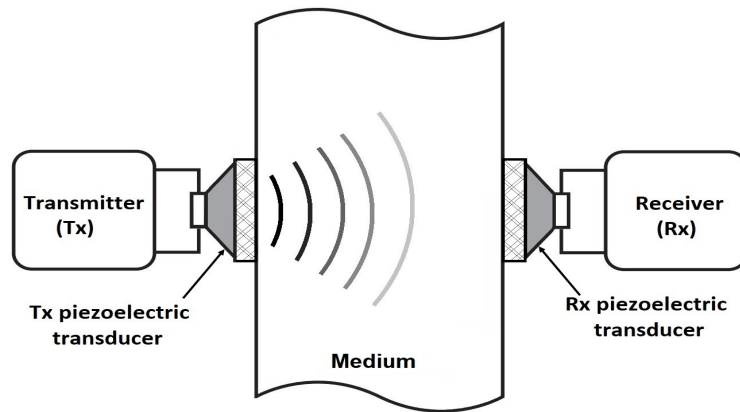
Figure 2.5: A typical acoustic power transfer system.

The power transfer efficiency in APT systems highly depends on the quality of PZT coupling [7]. Acoustic power transfer demands the pair of piezoelectric transducers to be coaxially coupled together at either sides of the medium, which is mostly difficult to be achieved. Considering this requirement, PTE in APT systems is relatively lower than other NF-WPT techniques [36, 65]. The acoustic power transmission technique has a limited application. It has been primarily used in low-power (i.e.: $< 100\,$mW.) biomedical applications with PTE up to 40% [36]. APT can also benefit stationary (i.e.: Tx/Rx fixed at a location.) WPT through-metal applications [66]. Achieving high PTE levels in APT through-metal systems necessitates applying a couplant material (e.g.: resin, epoxy, etc.) to the metal's contact surface in order to ensure both the PZTs are tightly and coaxially bond to the medium. Although this wireless power delivery technique can provide high PTE for WPT through-metal applications, it demands physical contact between the Tx/Rx and the metallic surface, which is not ideal for a wide range of WPT applications.

In addition to these, the functionality of the PZTs is also limited to a maximum operating temperature (i.e.: Curie point [66].) determined by the utilised piezoelectric material. This limitation makes the APT unsuitable for applications with operating temperature higher than the PZT's Curie point, such as WPT through high-temperature chemical chambers.

20
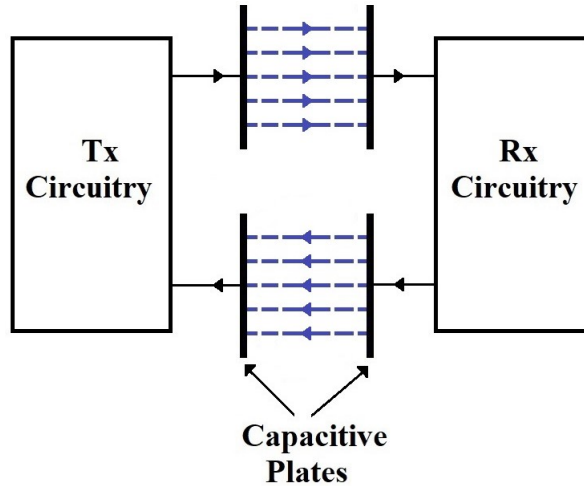
Figure 2.6: A typical capacitive power transfer system.

2.3.2 Capacitive Power Transfer

Capacitive power transfer (CPT) employs electric field coupling between one or two pairs of transmitting and receiving capacitive (metallic) plates for cordless energy delivery purposes. In this technique, the electric field at the primary capacitive plate/plates leads to the charge displacement in the secondary plate/plates, which results in electric flow (i.e.: electrical current.) inside the Rx circuitry and power transfer. The CPT systems usually require two sets of capacitive plates to form a closed current loop, as shown in Fig. 2.6 [67, 68]. However, it is also possible to achieve CPT using only one set of capacitive plates [67]. This WPT technique has only been recently considered for cordless power delivery applications. This is mainly because the power transfer efficiency in CPT systems is constrained by the specific physical requirements for the coupled capacitive pair [1, 69–71].

In CPT systems receiving a measurable power level at the Rx side demands increasing capacitance of the Tx/Rx plates. Improving the capacity of the coupled pair necessitates reducing the separation distance between the Tx and Rx plates [67]. This requirement limits the CPT to short-range wireless power transfer systems [1], typically $< 300\,\text{mm}$ [3, 36]. The efficiency in capacitive power transfer systems can be also improved by significantly increasing the surface area (i.e.: coupling area.) of the Tx and Rx capacitive plates

21
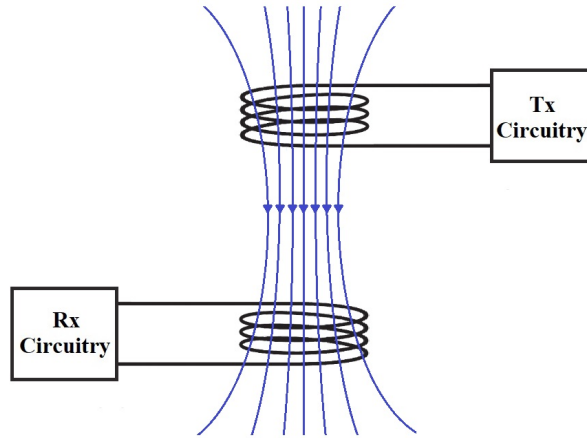
Figure 2.7: Inductive power transmission.

[67]. This requirement cannot be achieved in many WPT applications (e.g.: power delivery to IMDs, energy transmission through metallic pipelines [9], etc.) due to their spatial restrictions.

The capacitive power transfer technique has a lower average efficiency than inductive WPT [1, 3, 36, 68]. In general, CPT is more suitable for short-range applications that can adapt the capacitive plate's spatial requirements and such wireless power transfer applications typically include energising EVs, UAVs and mobile phones [3, 23, 72].

2.3.3   Inductive Power Transfer

Inductive power transfer (IPT) employs magnetic coupling between a transmitter and a receiver coil to deliver wireless energy, as schematically depicted in Fig. 2.7. IPT is based on the principle that a varying magnetic field produced by a primary winding will induce a magnetic field inside a secondary winding. The primary field, when interacting with secondary winding, will set up a current flow in a load connected to the secondary and power is transferred. This induction mechanism can also be used for wireless data transmission between the transmitting and receiving coils [73].

The inductive power transmission, pioneered in Tesla's era, resumed its technological evolution in 1960s after development of a magnetic coupling system for cordless energy

delivery through chest wall of an animal [8, 74]. Since then, IPT has become a well-established method of near-field wireless power transfer and has been employed in many diverse applications. Inductive power transfer is a cost-effective method of energising electric-driven devices with any level of power demand [38]. It can benefit WPT applications with any spatial requirements both in size and geometrical shape. For example, solenoid coils under a 1–mm size have been designed in [31] to support chronic neural recording implants. Magnetic coupling, due to its non-radiative nature, makes possible wireless energy delivery through a wide range of transmission media without the requirement for physical contact with the medium.

In comparison with APT and CPT, inductive power transfer can provide high PTE levels when delivering electrical energy over a short-range transmission distance (i.e.: less than Tx/Rx dimension.) [6, 8, 14, 21]. However, with a distance increase between Tx and Rx the induced power in the receiver side will quickly degrade due to magnetic flux leakage (i.e.: leakage inductance.) in the energy transfer link. This results in a significant PTE reduction in IPT applications with a longer transmission distance. Resonant inductive power transfer is an alternative magnetic coupling approach which provides higher PTE levels.

2.3.4   Resonant Inductive Power Transfer

Resonant inductive power transfer employs magnetic resonant coupling between a transmitter and a receiver coil for wireless energy delivery purposes. The efficiency in inductive power transfer is affected by the large leakage inductance in the energy transfer link [6]. Adding resonators (i.e.: compensation capacitors.) to the inductively coupled windings can effectively cancel out the leakage reactance of the system. The operating principle of resonant IPT systems is based on the fact (i.e.: resonant coupling concept in physics.) that two objects resonating at the same frequency will strongly interact with each other [75]. The resonant IPT approach technologically blossomed in 2007 when a group of physicists from Massachusetts Institute of Technology (MIT) demonstrated a highly efficient WPT

system based on magnetic coupling between a set of transmitting and receiving resonators (i.e.: LC resonators.) two meters apart [6, 14, 62].

Enhancing PTE in resonant IPT systems requires both the Tx and Rx resonators to be tuned to the same operating frequency. The resonant frequency (f_o) in these systems is usually in the range of few kHz to several MHz (i.e.: low- and mid-frequency bands.) [8, 12, 21, 35]. This is because at these bands the safety concerns related to SAR and human exposure under electromagnetic fields can be largely avoided [8, 32]. It should be noted that the power processing circuitry (i.e.: transmitter's terminating circuitry.) used to drive the WPT systems are mostly switched mode power converter arrangements. Operating the system at low- and mid-frequency range reduces the switching losses in the driving circuitry; hence, leading to higher source-to-load PTE levels [8]. Also, for WPT systems transmitting high power levels, operating at this frequency range is highly cost-effective since the power processing circuitry at low- and mid-frequency bands are readily available and more economic [8]. Additionally, many WPT applications require energy delivery through media with conductivity (σ) and/or relative permeability (μ_r) higher than air [76]. Typical examples of such media include: skull [31, 42], buffer solutions [76], metallic chambers [9, 66, 77–79], concrete [16], seawater [24], etc. Operating the resonant IPT system at low- and mid-frequency ranges, by reducing power absorption inside the medium [9, 24, 66, 77, 78], offers higher PTE levels [80].

By employing a resonant IPT approach typically maximum PTEs of 80%–95% can be readily achieved [37]. Resonant inductive coupling, by providing a strong inductive interaction between the Tx and Rx coil pair, provides the highest level of power transfer efficiency between all near-field WPT techniques. However, maximising PTE in resonant inductive power transfer links has always been a challenge [21, 30, 37, 72, 81].

2.4 Maximising PTE in the RIPT Systems

Power transfer efficiency is a key performance parameter in the development work on any wireless power transfer system. In resonant inductive power transfer systems, maximising PTE requires strong magnetic resonant coupling between the transmitter and receiver coils [62]. In this section, the parameters affecting PTE in the resonant IPT systems are discussed and the available methods to maximise the efficiency are reviewed.

A generic schematic of the resonant IPT systems is shown in Fig. 2.8, where v_s and R_L represent the ac voltage source (i.e.: power source.) and the target load, respectively. For this system, the power transfer efficiency is defined as the power received at the load divided by the power injected into the IPT link by the ac voltage source. In a resonant IPT link PTE is influenced by three factors –

I) *Magnetic linkage*: The energy transfer path between the Tx and Rx influences the power loss inside the link which, in turn, determines the magnetic flux induced in the receiver and the system's overall PTE.

II) *Terminating circuitry of both the Tx and Rx sides*: The terminating impedances of the Tx–Rx pair set the circuitry power losses in the primary and secondary which, in turn, establishes the system loaded quality factor (Q_L-factor). Here, the quality factor is defined as the ratio of energy loss to the energy stored in the electrical component [48].
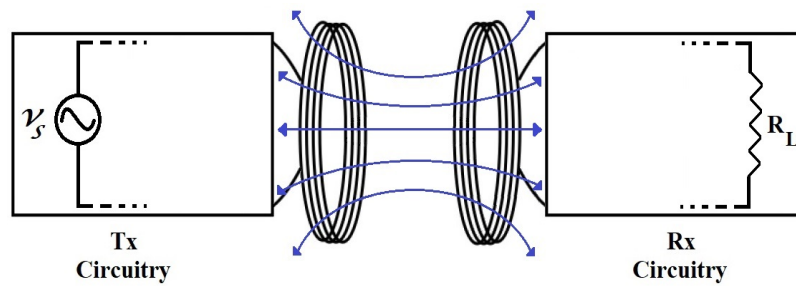
Figure 2.8: A generic schematic of the resonant IPT Systems.

III) *Coil geometry*: The coil's physical geometry (i.e.: diameter, length and number of turns.) determines the intrinsic quality factor (Q_i-factor) of the Tx–Rx coil pair which, in turn, affects their power transmission/receiving ability.

Maximising PTE in resonant inductive power transfer systems requires a resonant inductive link (or an inductive link in general) that possesses high magnetic flux coupling while both Q_i-factor and Q_L-factor are maximised (i.e.: strong coupling between Tx and Rx.) [62]. From a practical viewpoint fulfilling these requirements is not always possible. The bulk of WPT applications have a significantly long transmission medium with high attenuation levels between the transmitter and receiver which limits the link's magnetic flux coupling. The application's required power level also affects both the loaded and intrinsic quality factor values. The resonantly coupled coils can be used to wirelessly deliver any volume of power; from few μW in RFID tags [46] and implantable microelectronic devices [30, 39, 42, 43, 82–84] to kW range in electric vehicle (EV) battery chargers [18, 20, 21]. Managing such a range of power levels requires an IPT system with specific source and load resistance values, which imposes some constrains on the system's Q_L-factor.

The application requirements such as specific power level and space limitations also influence the topology and structural geometry of the inductive resonators (i.e.: Q_i-factor.). Two coil topologies commonly used in WPT applications are spiral and helical inductors [37, 85]. Different geometrical shapes can be adapted for both these topologies including square [20, 30], circle [31, 41] and hexagonal [42]. The planar structure of the spiral coils makes them more suitable for space-confined applications such as IMDs [30, 42, 83, 84] and portable electronic devices (e.g.: smart phones, cameras and laptops.) [13, 78]. On the other hand helical coils, due to their uniform magnetic field [31], can provide a large inductive coupling in comparison with spiral coils [20, 31, 43, 44, 56, 86]. Examples of such systems include high-voltage battery charging [21, 87, 88] and WPT through-metal-walls [9, 48, 49, 66, 79, 89–94]. It should be noted that selecting the coil topology is mainly influenced by the application's spatial restriction. For example Wang et al. [18] and Sallán

et al. [20], have utilised spiral (planar) coils in EV battery charging with high power level requirements under limited space restrictions.

These limitations and requirements necessitate optimising the physical circuit parameters of a resonant IPT system accordingly, which can be highly challenging. Different methodologies have been utilised to maximise power transfer efficiency with regards to the mentioned three impacting factors, that are: magnetic linkage, terminating circuitry of both the Tx and Rx sides and coil geometry.

2.4.1 Maximising Magnetic Resonant Linkage

In a resonant IPT system the magnetic flux linkage between the Tx and Rx strongly impacts the system's overall power transfer efficiency. The magnetic resonant linkage is influenced by transmission medium's attenuation level, distance between the Tx and Rx coil pair (d_t) and their orientational position with respect to each other (i.e.: axial misalignment.). To reduce magnetic flux leakage with respect to these impacting factors, different approaches have been adapted.

To enlarge the power transmission distance, multiple LC–resonators in domino arrangement can be placed between the transmitter and receiver coil pair [37, 95]. Domino intermediate resonators can also benefit the WPT systems with axial misalignment in the Tx/Rx coil path [37]. However, employing these intermediate resonators yields frequency splitting, in which the system operating frequency will be shifted away from f_o, by adding each set of resonators [8]. Ensuring the system operation at the magnetic resonant state necessitates adding adaptive impedance matching networks (e.g.: a matrix of capacitors [96].) to track the resonance frequency [1, 97]. Domino LC–resonators increase the system complexity, weight and size; hence, cannot be employed in the WPT applications with extreme spatial limitations.

To reduce power attenuation inside the air-gap between the Tx and Rx (i.e.: transmission medium.) different types of magnetic shields have been adapted which can suppress

energy flow in undesired directions. A method to achieve this is by placing metallic planes in the close proximity of the Tx or both the Tx and Rx coils [98, 99]. These shielding plates are mostly heavy and physically large, which makes the applications of this technique limited to the WPT systems that can accommodate placing magnetic shields in the air-gap between the transmitter and receiver.

In a resonant IPT system, the magnetic flux coupling can be increased by adopting ferrite materials (i.e.: high permeability materials.) as the core for the Tx/Rx coils [44]. Adding ferrite cores to the primary/secondary inductors improves the coil self-inductance which, in turn, boosts the inductive linkage between the transmitter and receiver [18, 21, 44, 47–49]. However, employing ferrite-cored coils in the resonant IPT link will significantly increase the system's overall weight and cost. In these WPT systems, reducing the coil physical weight concurrent with maintaining maximised inductive linkage, necessitates designing a geometrically optimised coil pair. An iterative algorithm to find the optimum geometry for the Tx/Rx ferrite-cored coil pair in a resonant IPT system has been developed in chapter 5.

2.4.2   Optimising the Terminating Circuitry

The other factor affecting power transfer efficiency in a resonant IPT system is the terminating circuitry at the transmitter and receiver sides (i.e.: source and load impedances.). The power level dissipated in the source resistance (R_s) determines what remaining power is left for the inductive link [40]. This means with an increase in R_s value, the system's source-to-load power transfer efficiency will decrease. Hence, maximising PTE necessitates reducing the R_s value to zero [81, 100]. Considering the fact that the source resistance practically cannot be reduced to zero, it should be selected as low as possible (i.e.: typically $\leq 50\,\Omega$.) to ensure maximum PTE level [101]. In a resonant IPT system, the power level received at the secondary is also influenced by the load resistance (R_L) value. Considering these constraints, the system's maximum PTE occurs at single optimum load resistance

value (R_{L_O}) which is influenced by the RIPT application and the power level requirements [101, 102].

In most empirical RIPT applications the actual load resistance varies and cannot be kept fixed at its nominal optimum value (i.e.: R_{L_O}.). This, for example, can be due to the variations in the distance between the Tx and Rx coils. Different methods have been adopted to adjust and hold the receiver's rated impedance (i.e.: the actual R_L value.) at its nominal optimum value to support maximum energy transmission [24, 72, 81, 102–104]. These techniques typically consist of voltage regulators and/or load modulators.

Voltage regulators, such as switched mode dc-dc converters [72] and buck-boost converters [104], by regulating the receiver's voltage ensure the load impedance is equivalent or nearly-equivalent to its nominal optimum value (i.e.: R_{L_O}.). Adding these units to the system, by increasing the switching losses, yields a significant drop in the energy efficiency of the IPT application [81, 102]. Also, considering the time constants associated with the added converters, the system's overall dynamic response will be slower.

To alleviate the difficulties using voltage regulators, different load modulation techniques have been adopted as the alternative impedance adjustment approach [24, 72, 81, 102, 103]. Some examples of load modulators are Q-modulation [103], on-off keying (OOK) [81] and pulse density modulation (PDM) [102]. Table 2.1 shows the maximum achievable PTEs for the exemplified load modulation methods. From the table it can be seen that the average overall efficiency in these techniques is low. This necessitates employing a second PTE maximisation approach (e.g.: enhancing the Q_i-factors.) to accompany the load modulators [102]. Also, the adopted tuning techniques utilise closed-loop controllers to track the load variations, and an RF wireless signal path is employed as part of the control loop between the transmitter and receiver to feed the information on R_L changes back to the Tx side. The closed-loop controller for an OOK modulation technique has been demonstrated in Fig. 2.9, where to maintain the load impedance equivalent to its optimum value, the information of load voltage (v_L), in the form of RF signal (i.e.: RF

Table 2.1: Maximum Achievable PTE using different load modulation techniques.

Modulation technique	f_o (MHz)	d_t (mm)	K	Optimal R_L (Ω)	PTE (%)	Reference
Q	2	80	0.05	15	27	[103]
OOK	0.9756	200	0.0689	10	72.6	[81]
PDM	0.917	500	0.01	25	70	[102]

radiation.) is used to control switching actions of the power inverter at the primary side [81]. Such systems with RF control/feedback have limited uses. This is because RF signal will be significantly attenuated in transmission media with electric conductivity (σ) and/or relative magnetic permeability (μ_r) higher than air.

Considering the difficulties and inefficiencies that exist in using the voltage regulators and modulators, it can be concluded that optimising the Tx/Rx circuitry cannot maximise PTE in all RIPT applications.
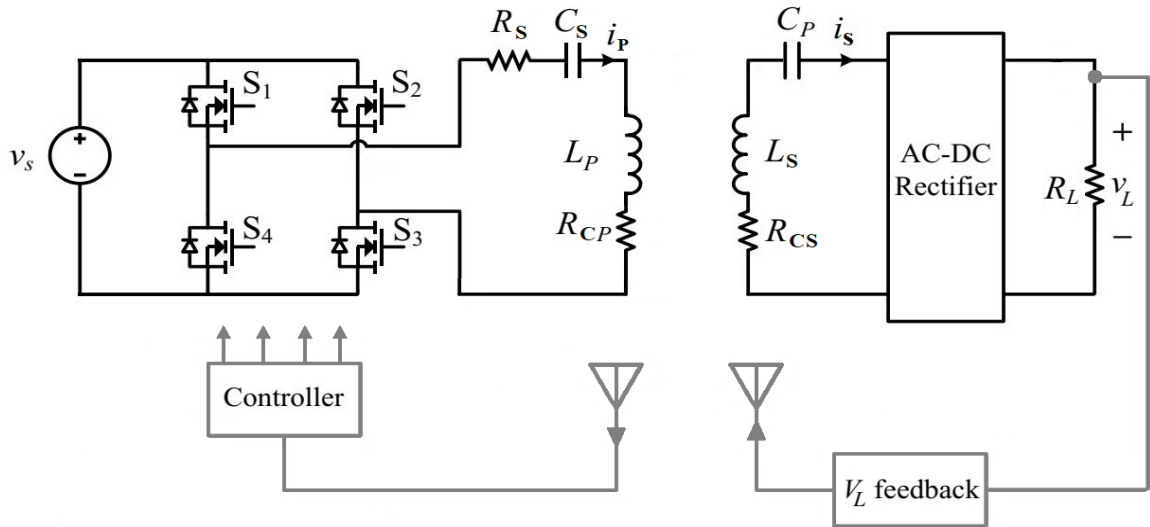
Figure 2.9: The schematic of an OOK modulator employed to maximise the power transfer efficiency in the RIPT systems [81]. The closed-loop controller, shown in gray, has been used to maintain the load resistance equivalent to its optimum value.

2.4.3   Optimising the Physical Size of Coils

Geometric optimisation of the Tx/Rx coil pairs is the third method of improving the magnetic resonant linkage. This approach can additionally reduce the RIPT system's physical size. Much work has been devoted to maximising PTE through coil geometry optimisation over the last few decades [20, 21, 30, 31, 39–43, 56, 85, 101, 105–112].

One of the methods for geometric optimisation of inductive coils is through increasing Q_i-factor of the Tx/Rx coil pairs as considered by many researchers including [105–108]. In the proposed technique, to improve Q_i-factor, the coil's winding layout has been modified in different ways such as varying the winding's track width [105] and increasing the coil's inner radius [107]. Employing a Tx/Rx coil pair with higher Q_i-factor can improve the energy transmission of the pair, however maximising source-to-load power transfer efficiency requires configuring the coil's geometry while compensating the loading effect of inductive link's coupling (i.e.: coupling coefficient K.) and Q_L-factor as well [113].

To maximise the IPT system's overall PTE different iterative design algorithms have been proposed over the last decades [20, 30, 31, 39–43, 56, 85, 101, 109–112]. As a common approach to cancel out the loading effect of Tx/Rx terminating circuitry, Jow et al. [30], Ibrahim et al. [39], Sallan et al. [20], Hwang et al. [56], Ko et al. [110], and Donaldson et al. [111] have found equations for power transfer efficiency based on system parameters (e.g.: K, R_s, R_L, etc.). Then, for the derived PTE equation, various figure-of-merit (FoM) parameters have also been defined to help improve the energy transmission efficiency for the purpose application. For example, to optimise the geometry of printed spiral coils in a cortical visual prothesis, as listed in Table 2.2, the coil's diameter (D), conductor width (W), winding's distribution over the spiral disk (φ) and number of turns (N) for both the Tx and Rx coils have been considered as FoM parameters by Jow et al. [30]. In these proposed techniques, in order to determine the proper numerical combination of FoMs which maximises PTE, the design parameters are swept one by one over a wide range around their pre-selected initial values. This process is repeated until the considered

Table 2.2: Figure-of-merit parameters & design values for a resonant IPT application [30].

FoM parameters	Symbols	Initial values	Optimised values
Diameter - Tx coil	D_{Tx} (mm)	20	70
Diameter - Rx coil	D_{Rx} (mm)	8	20
Conductor width - Tx coil	W_{Tx} (μm)	38	3250
Conductor width - Rx coil	W_{Rx} (μm)	38	250
Fill factor - Tx coil	φ_{Tx}	0.43	0.85
Fill factor - Rx coil	φ_{Rx}	0.43	0.43
Number of turns - Tx coil	N_{Tx}	71	9
Number of turns - Rx coil	N_{Rx}	31	15

combination produces a desired PTE level. The selected initial FoMs and their respective designed optimum values, for the previous example, are shown in Table 2.2. As can be seen, the optimised FoM values have significant differences from their preliminary values which indicates the high number of taken iterations. Using this method respective measured PTEs of 41.2% at $f_o = 1\,\text{MHz}$ and 85.8% at $f_o = 5\,\text{MHz}$ are found for a transmission distance of $10\,\text{mm}$ and a $500\,\Omega$ resistive load.

Depending on the number of geometrical variables (i.e.: FoMs.) that need to be swept, the proposed coil optimisation techniques clearly are very time consuming [20, 31]. To accelerate finding the optimal FoM parameters and make the design process more intuitive, Ahn and Ghovanloo [43] and Cheng et al. [31] have defined a combination of the design parameters as the FoM parameter required for maximising PTE. To optimise the Rx coil geometry, Cheng et al. [31] considered multiplication of three design parameters as the only required FoM. These design parameters are the receiver's Q_L-factor, a part of the inductive link's coupling coefficient and a ratio of power delivery to the load as the only required

FoM. Utilising the defined FoM parameter, a 4-turn solenoid using a 0.1270-mm (diameter) copper wire was prototyped for millimetre-sized IMDs. The proposed method only focuses on optimising Rx coil geometry to improve PTE. Also, there is no indication of the system's required power level and achieved PTE. To consider the effect of both Tx and Rx in maximising the system's source-to-load PTE, Ahn and Ghovanloo [43] have defined two independent FoMs (i.e.: Rx-FoM and Tx-FoM.) representing the roles of primary and secondary sides. The Rx-FoM has been considered such that its value indicates how efficiently the application's load can receive the power. This is achieved through multiplying the receiver's Q_L-factor and the ratio of power delivery to the load. The Tx-FoM is defined as the link's coupling coefficient squared multiplied by the transmitter Q_i-factor (i.e.: $K^2 Q_{i_p}$.). The multiplication of Rx- and Tx-FoMs provides the IPT system's overall PTE. Utilising this technique the first step to improve PTE is to maximise the Rx-FoM, then the Tx coil geometry is optimised with considering the designed receiver. Using the developed Tx and Rx coils, the overall PTE of 1.02% was measured while the power delivered to the load was 224 μW with 12 mm distance between the primary and secondary (i.e.: estimated $K = 0.002$.). In the proposed approach the inductive link's coupling coefficient is considered as a property of Tx-FoM. Coupling coefficient (i.e.: K.), based on its definition, is affected by both the Tx and Rx however [31].

The incompetence of the available geometry design techniques necessitates developing a new FoM parameter to accelerate the design of optimum coil geometries which maximises PTE. The present research work covered in this thesis modifies the approach introduced in [43] by considering a single FoM parameter such that its value indicates how strongly both the transmitter and receiver sides are linked together. The proposed FoM parameter, named as 'Strong Coupling Factor' (P_{scf}), has been defined as: $P_{scf} = K^2 Q_{L_p} Q_{L_s}$. This thesis also introduces a method to assist selecting the most favourable numerical value for the strong coupling factor which can maximise PTE for the designed optimum coil geometry.

Also, it should be noted that the available coil design algorithms in the literature mainly focus on spiral coils or low power (i.e.: $\ll 1\,\text{W}$.) mm-size solenoids. However geometrical optimisation of high-power helical coils can be equally important. This is because for the coils to be suitable for high power RIPT applications, the coil winding conductor must be large enough to tolerate the transmitting current level. This requirement yields a bulky coil geometry which in a physical implementation can encounter spatial difficulties. For example, in a typical WPT application transmitting $0.5 - 5\,\text{W}$ power through-metal, a solenoid with diameter of $84\,\text{mm}$, length of $152\,\text{mm}$ and 260 turns is required to operate at $300\,\text{kHz}$ [79], geometrical optimisation of the Tx/Rx coil, besides improving PTE, can significantly reduce the system's overall size. Considering this requirement, the proposed method in this thesis will be developed through geometrical optimisation of a helical coil (i.e.: solenoid.). It is worth mentioning that the presented geometry optimisation technique can also advantage low power RIPT applications with sizable Tx/Rx helical coils. One example of such applications is the capsule endoscopy system presented in [114], where a 120 turns Tx solenoid operating at $f_o = 750\,\text{kHz}$, delivers $39\,\text{mW}$ power to the receiver.

2.5 Summary

This chapter presented a detailed overview of wireless power transfer techniques which are classified as far-field and near-field WPT. NF-WPT approach is shown to be biologically safer and more suitable for cordless energy delivery to electric-driven devices which are located in close proximity of living tissues. Among different methods of near-field WPT, RIPT can provide the highest level of power transfer efficiency. The RIPT system's PTE is influenced by inductive linkage between the primary and secondary, terminating circuitry at the Tx and Rx sides and the Tx–Rx coil geometry. The available methods to maximise PTE, with respect to these impacting factors, are comprehensively reviewed. It is shown that geometrical optimisation of the Tx and Rx coil pair is the key parameter to maximise PTE in a wide range of applications. This technique can be used either separately or in combination

with other techniques which are devoted to improving PTE. An overview of the geometry optimisation methods available in the literature is provided. These approaches mainly require proper selection of a range of design parameters and are clearly very time-consuming. To improve the available techniques, a new figure-of-merit parameter is developed in the next chapter to accelerate finding an optimum coil geometry which maximises PTE.

CHAPTER 3

POWER TRANSFER EFFICIENCY ANALYSIS

In this chapter, the physical parameters affecting PTE of a resonant inductive WPT system are theoretically analysed and the figure-of-merit (i.e.: FoM.) parameter required to maximise PTE is discussed.

3.1 Analytical Model of Air-cored Coils

The physical coil model for an air-cored, single-layered solenoid (i.e.: circular helical coil.), is shown in Fig. 3.1. In the figure, the wire diameter is d_w, the coil radius is r_c and the coil length is l_c ($l_c \gg r_c$). A circular geometry is adopted since it can provide better coupling between the transmitter and receiver in the majority of WPT applications [20, 115]. The wire-wound air-cored coil (ACC), according to [28], can be modelled as an inductance (L) series with a parasitic resistance (R_c) (i.e.: ac ohmic resistance.) and a parasitic capacitance (C_c) which is parallel with both the L and R_c, as shown in Fig. 3.2a. For a single-layered ACC operating at low- and mid-frequency bands the parasitic capacitance value is negligible [28]. Hence, the ACC equivalent circuit model in RIPT systems has been widely considered as an inductance in series with a R_c, as shown in Fig. 3.2b [1–4, 6, 13, 14, 18, 20, 37, 38, 62, 72, 73, 79–81, 116]. Models for calculation of self-inductance
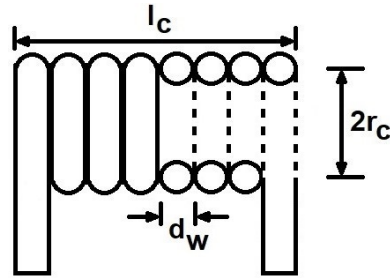
Figure 3.1: The structure of an air-cored solenoid, where l_c is coil length, r_c is the coil radius and d_w is wire diameter.
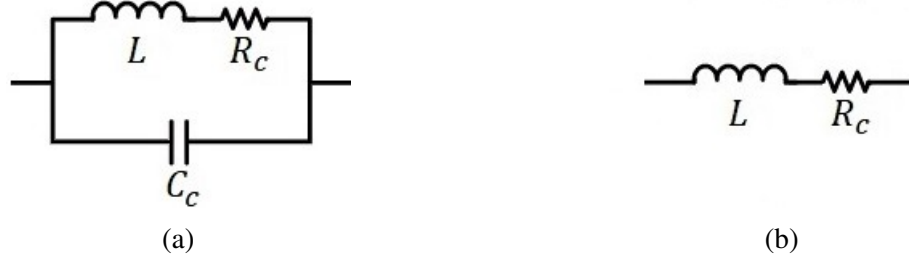
Figure 3.2: The equivalent circuit models for a typical wire-wound air-cored coil: (a) RLC equivalent model, (b) series equivalent model.

and ac ohmic resistance in typical single-layered air-cored solenoids are well established [41, 62, 73, 117–121]. In this section the models of L and R_c have been adopted from various references and will be utilised to calculate the ACC's self-inductance and parasitic resistance in the rest of thesis.

For a tightly-wound air-cored solenoid the self-inductance, according to [73, 117], can be expressed as:

$$L = \frac{\mu_o \pi N^2 r_c^2}{\sqrt{4r_c^2 + l_c^2}} \tag{3.1}$$

in which N is number of turns and μ_o is free-space permeability (i.e.: $\mu_o = 4\pi \times 10^{-7}$ Henrys per meter.).

Calculating the ACC's parasitic resistance requires having the knowledge of RIPT system's operating frequency [122]. Due to skin effect, as the operating frequency increases, the electric current passing through the wire will be more concentrated near outer surface (i.e.: skin layer.) of the conductor. This results in having larger R_c values as frequency increases. Hence, the coil's parasitic resistance is frequency dependent. The coil ac ohmic resistance, according to [62, 118–121], can be expressed as:

$$R_c = Nr_c \eth . \tag{3.2}$$

In (3.2) the skin effect losses inside the winding wire is noted as $\eth$. The parameter $\eth$, based on [118–121], can be calculated from the following piecewise function:

$$
\eth = \begin{cases} \dfrac{2\,\rho}{\delta\,d_w} & \text{if} \quad \delta < \dfrac{d_w}{2} & (3.3) \\[4ex] \dfrac{\rho\,(192\,\delta^2 + d_w^2)}{24\,\delta^2\,d_w^2} & \text{if} \quad \delta \geq \dfrac{d_w}{2} & (3.4) \end{cases}
$$

where the parameter δ (i.e.: skin depth.) is the thickness that the amplitude of current density reaches e^{-1} of its initial value (i.e.: $\approx 36.8\%$ of initial value.) at the outer surface of wire and can be stated as:

$$
\delta = \sqrt{\dfrac{\rho}{\pi\mu f_o}} \, . \tag{3.5}
$$

In (3.5) μ and ρ are the permeability and resistivity of winding wire material, respectively. For a copper wire these values are $\mu = \mu_o$ and $\rho = 1.72 \times 10^{-8}$ Ω.m [120]. Replacing (3.5) in (3.3)– (3.4), the parameter $\eth$ can be simplified to:

$$
\eth = \begin{cases} \dfrac{\sqrt{2\omega_o\mu\rho}}{d_w} & \text{if} \quad f_o > \dfrac{4\rho}{\pi\mu d_w^2} & (3.6) \\[4ex] \dfrac{384\rho + \omega_o\mu d_w^2}{48 d_w^2} & \text{if} \quad f_o \leq \dfrac{4\rho}{\pi\mu d_w^2} \, . & (3.7) \end{cases}
$$

Based on this, in a typical RIPT system where a copper wire with a diameter equal to 0.8 mm is used for winding the coils, the case changing frequency is 27.29 kHz (i.e.: $\dfrac{4\rho}{\pi\mu d_w^2} = 27.29$ kHz.). Hence, in this system if the operating resonance frequency is higher than 27.29 kHz then equation (3.6) should be used to estimate the ACC's parasitic resistance, and if equal or below this frequency (3.7) is used.

3.2 Resonant Inductive Power Transfer Circuit Model

To investigate the basic requirements for resonant coupling of Tx and Rx coils, a generic lumped circuit diagram of a RIPT system, based upon [1], is shown in Fig. 3.3. In this circuit model v_s and R_s represent the ac voltage source (in time domain) and its internal resistance. The primary and secondary coils' excitation currents (in time domain) are noted

38
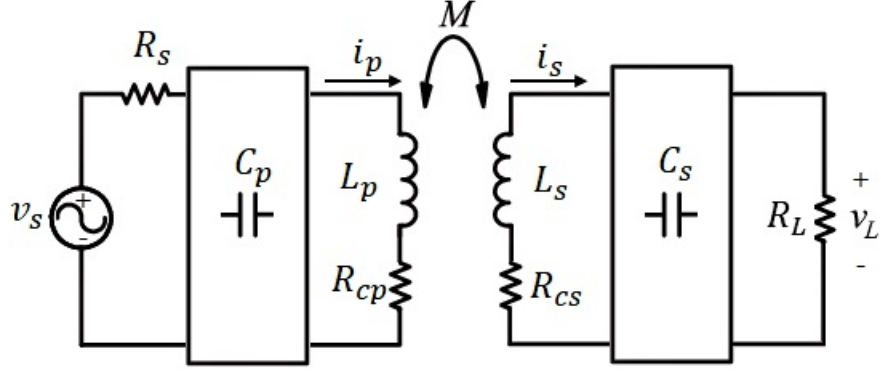
Figure 3.3: General configuration of a resonant inductive power transfer system.

as i_p and i_s respectively. The self-inductance values of the Tx and Rx windings are represented by L_p and L_s, while M is the mutual inductance between them. The ac ohmic resistances of the Tx and Rx windings are noted as R_{cp} and R_{cs} respectively. The C_p and C_s are representations of the compensation capacitors added to the Tx/Rx circuitry for effective cancelation of the leakage reactance in the link [62]. Also, the equivalent ac/dc load resistance, which power is being delivered to, is indicated by R_L.

Following the common approach utilised in [30, 39, 42, 43], the equivalent source and load resistances (i.e.: R_s and R_L.) have been considered to represent the rest of the system's electronics. This is because in a RIPT system, the application's requirements and limitations demand different types of power amplifier (e.g.: class-E power amplifier [123], full-bridge type inverter [21], etc.) and power management units (e.g.: buck-boost converter [72], rectifier [124], dc-dc converter [116, 125], etc.) to be utilised at the primary and secondary sides, respectively. Maximising PTE of these units have been extensively studied in the literature [116, 123–125] and is outwith the scope of this thesis [30].

3.2.1 Selection of Compensation Scheme for Resonant Coupling

In a resonant inductive power transfer system, the primary and secondary compensation capacitors can be either connected in series or parallel with their respective coils [122]. Depending on the connecting configuration of LC resonators to the Tx and Rx sides there
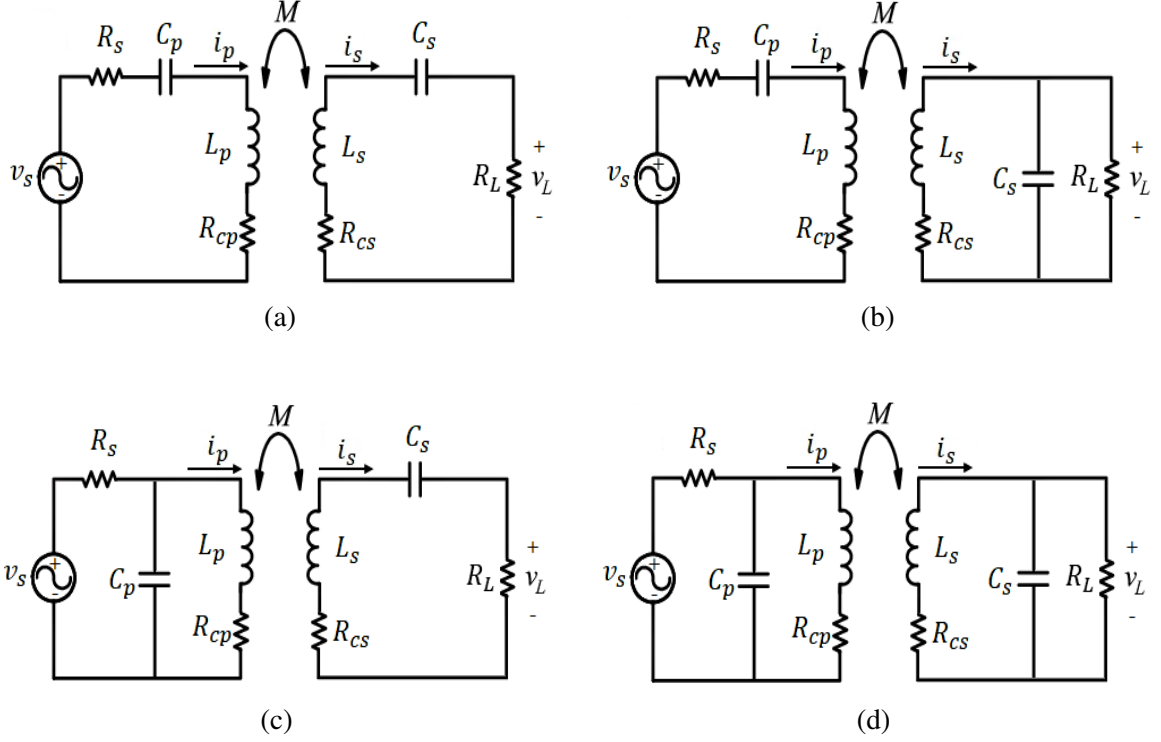
Figure 3.4: The possible topologies of resonant inductive power transfer systems: (a) series-series, (b) series-parallel, (c) parallel-series, (d) parallel-parallel.

can be four compensation topologies for resonant inductive links. As shown in Fig. 3.4 these are: series-series (SS), series-parallel (SP), parallel-series (PS), and parallel-parallel (PP).

Maximising PTE in a magnetically coupled link demands zero phase angle between the primary's voltage (i.e.: phasor V_s.) and current (i.e.: phasor I_p.) at f_o [15, 126]. This is to ensure zero reactive power (i.e.: unit power-factor.) in the resonant inductive link. Maintaining this requirement necessitates compensation of the total system impedance to make it purely resistive. In a RIPT system, the total impedance is defined as:

$$Z_t = \frac{V_s}{I_p}$$

where Z_t is the phasor of total impedance. For the inductive links shown in Fig. 3.4, the

Z_t can be found from equations (3.8) – (3.11):

$$Z_{t_{SS}} = R_s + R_{cp} + \frac{\omega^2 M^2}{R_{cs} + R_L + j\left(L_s\omega - \dfrac{1}{C_s\omega}\right)} + j\left(L_p\omega - \frac{1}{C_p\omega}\right) \tag{3.8}$$

$$Z_{t_{SP}} = R_s + R_{cp} + \frac{\omega^2 M^2 \left(1 - C_s L_s\omega^2 + jR_{cs}C_s\omega\right)}{R_{cs} + R_L - R_L C_s L_s\omega^2 + j\left(R_{cs}C_s R_L\omega + L_s\omega\right)}$$

$$+ j\left(L_p\omega - \frac{1}{C_p\omega}\right) \tag{3.9}$$

$$Z_{t_{PS}} = R_s + \frac{\omega^2 M^2}{R_{cs} + R_L + j\left(L_p\omega - \dfrac{1}{C_p\omega}\right)} + \frac{R_{cp} + jL_p\omega}{1 - C_p L_p\omega^2 + jR_{cp}C_p\omega} \tag{3.10}$$

$$Z_{t_{PP}} = R_s + \frac{\omega^2 M^2 \left(1 - C_s L_s\omega^2 + jR_{cs}C_s\omega\right)}{R_{cs} + R_L - R_L C_s L_s\omega^2 + j\left(R_{cs}C_s R_L\omega + L_s\omega\right)}$$

$$+ \frac{R_{cp} + jL_p\omega}{1 - C_p L_p\omega^2 + jR_{cp}C_p\omega} \cdot \tag{3.11}$$

If the IPT system is operated at resonance, the angular frequency can be replaced with:

$$\omega = \omega_o = 2\pi f_o = \frac{1}{\sqrt{L_p C_p}} = \frac{1}{\sqrt{L_s C_s}} \ (rad/s)\,.$$

Considering ω_o, the total system impedance can be restated as:

$$Z_{t_{SS}} = R_s + R_{cp} + \frac{M^2}{L_s C_s(R_{cs} + R_L)} \tag{3.12}$$

$$Z_{t_{SP}} = R_s + R_{cp} + \frac{jR_{cs}M^2}{L_s + R_{cs}\sqrt{L_s C_s} + jR_{cs}R_L C_s} \tag{3.13}$$

$$Z_{t_{PS}} = R_s + \frac{L_p - jR_{cp}\sqrt{L_p C_p}}{R_{cp}C_p} + \frac{M^2}{L_s C_s(R_{cs} + R_L)} \tag{3.14}$$

41

$$Z_{t_{PP}} = R_s + \frac{L_p - jR_{cp}\sqrt{L_pC_p}}{R_{cp}C_p} + \frac{jR_{cs}M^2}{L_s + R_{cs}\sqrt{L_sC_s} + jR_{cs}R_LC_s} \, . \tag{3.15}$$

From equations (3.12) – (3.15) it can be deduced that only the SS compensation topology can provide an inductive link with unit input-power-factor at f_o (i.e.: a reactance-free link.) [18, 20, 52, 122]. Utilising the other compensation topologies requires tuning the overall system reactance out of the IPT link to ensure zero phase angle between V_s and I_p. Compared to other topologies the SS compensation, with its reactance-free link, does receive more coverage in the literature [18, 20, 52, 81, 122]. For this reason a series-series compensated inductive link (i.e.: Fig. 3.4a.) has been utilised in this work to model the RIPT system.

3.3 Maximum Power Transfer Efficiency Formulation

For the considered series-series compensated resonant inductive link shown in Fig. 3.4a, the application of Kirchhoff's voltage law (KVL) at resonance, ω_o, can be expressed as:

$$\begin{bmatrix} V_s \\ V_L \end{bmatrix} = \begin{bmatrix} R_s + R_{cp} & -jM\omega_o \\ jM\omega_o & -R_{cs} \end{bmatrix} \begin{bmatrix} I_p \\ I_s \end{bmatrix} \tag{3.16}$$

where V_s is the RMS value of sinusoidal ac voltage and V_L is the RMS value of voltage appearing at the system load. Also, I_p and I_s are the phasors of current in the Tx and Rx sides, respectively. In many RIPT applications, both the Tx and Rx are located in confined spaces. To facilitate duplex (i.e.: two-way.) WPT in such systems, the primary and secondary coils are considered identical. This implies:

$$L_p = L_s = L$$

$$C_p = C_s = C$$

$$R_{cp} = R_{cs} = R \, .$$

Considering this, the power transfer efficiency (η) with respect to (3.16) can be expressed as:

$$\eta = \frac{V_L |\boldsymbol{I_s}|}{V_s |\boldsymbol{I_p}|}$$

$$= \frac{R_L \omega_o^2 M^2}{(R_L + R)\left[(R_s + R)(R_L + R) + \omega_o^2 M^2\right]} \; . \tag{3.17}$$

Equation (3.17), based on the system quality factors, can be restated as:

$$\eta = \frac{K^2 Q_{L_p} Q_{L_s}}{1 + K^2 Q_{L_p} Q_{L_s}} \left(1 - \frac{Q_{L_s}}{Q_i}\right) \; . \tag{3.18}$$

In (3.18), K is the coupling coefficient between the coils which can be stated as:

$$K = \frac{M}{\sqrt{L_p L_s}} = \frac{M}{L} \; . \tag{3.19}$$

In the present research work the Tx/Rx coil windings are coaxially aligned. Therefore, based on [73, 117], the inductive link's coupling coefficient can be restated as:

$$K = \frac{\sqrt{4r_c^2 + l_c^2}}{2l_c} \left(1 - \frac{d_t}{\sqrt{d_t^2 + r_c^2}}\right) \tag{3.20}$$

where d_t is the transmission distance between Tx and Rx.

In (3.18), the ACC's Q_i-factor and the Tx and Rx side's Q_L-factor are respectively included as:

$$Q_i = \frac{\omega_o L}{R} \tag{3.21}$$

$$Q_{L_p} = \frac{\omega_o L}{(R + R_s)} \tag{3.22}$$

$$Q_{L_s} = \frac{\omega_o L}{(R + R_L)} \; . \tag{3.23}$$

From (3.18) a condition which guarantees maximum PTE (i.e.: $\eta = 1$.) can be expressed

as:

$$\begin{cases} Q_i - Q_{L_s} \equiv Q_i & (3.24) \\ \\ K^2 Q_{L_p} Q_{L_s} \equiv 1 + K^2 Q_{L_p} Q_{L_s} \,. & (3.25) \end{cases}$$

These require both the following inequalities to be satisfied:

$$\begin{cases} Q_i \gg Q_{L_s} & (3.26) \\ \\ K^2 Q_{L_p} Q_{L_s} \gg 1 \,. & (3.27) \end{cases}$$

The inequality (3.27) is an electrical representation for physical concept of strong coupling [62, 127], which expresses that a highly efficient RIPT link requires strongly coupled Tx and Rx. Meeting conditions (3.26) and (3.27) requires:

a) an inductive link with high level of inductive linkage.

b) Tx/Rx circuitry with high loaded quality factors.

c) high quality coils.

However, satisfying these requirements is highly challenging. In the following, each of these requirements are discussed in depth.

3.3.1 Inductive Link with High Coupling Coefficient

Depending on the RIPT system's application, the power transmission distance between the coil pair and their mutual orientation set K between 0 and 1 (i.e.: $0 \leq K \leq 1$.). In practical applications K is typically ≤ 0.3 [1, 8, 18, 62].

3.3.2 Transceiver System with High Primary and Secondary Q_L-Factors

A high Q_{L_p} value, based on (3.22), can be achieved if the Tx coil has high self-inductance and small parasitic resistance. Also, the R_s value should be as small as possible. This is

compatible with the fact that the level of power dissipated in the source internal resistance sets what power remains for the inductive link.

Based on (3.23), achieving a high Q_{L_s} value also requires a coil with high self-inductance and small parasitic resistance. In addition to these, it is required to have a small R_L value. However, the load resistance value is highly influenced by the RIPT application and its power level requirements. Hence, it is not necessarily possible to select a small R_L value for the RIPT systems. For a given RIPT application, there needs to be found an optimum R_L value to satisfy the operational requirement and maximise PTE [72, 81, 102, 116]. By differentiating η (i.e.: equation (3.17).) with respect to R_L the optimum load value which maximises PTE can be expressed as:

$$R_{L_O} = R\sqrt{1 + \frac{\omega_o^2 K^2 L^2}{R(R + R_s)}} \ . \tag{3.28}$$

It should be noted that in empirical applications the actual R_L value varies and cannot be fixed at its nominal R_{L_O} value.

3.3.3 Tx and Rx Coils with High Q_i-Factor

Increasing a coil's Q_i-factor basically improves its power transmitting/receiving ability, which from (3.21) requires a coil with high self-inductance and small parasitic resistance. In addition to this, based on section (3.3.2), having a high Q_i-factor coil improves the Tx/Rx side's Q_L-factor.

From equation (3.1), increasing N and r_c clearly improves ACC's self-inductance. However increasing these values also has the detrimental effect of raising the coil ac ohmic resistance, based on (3.2). The challenge in maximising PTE is thus to design a geometrically optimised ACC with maximised L and low R.

3.4 Optimum ACC Geometry for Maximised Power Transfer Efficiency

Finding an optimal ACC geometry to maximise PTE in a RIPT system requires exploiting the ACC self-inductance to yield an ohmic resistance that provides maximised inductive coupling between Tx and Rx ACC pair.

The ACC self-inductance, based on (3.1), is essentially a factor of three variables; N, r_c and l_c. In a tightly wound coil $l_c = N d_w$. Hence, equation (3.1) can be restated as:

$$L = \frac{\mu_o \pi N^2 r_c^2}{\sqrt{4r_c^2 + N^2 d_w^2}} \, . \tag{3.29}$$

Also, the number of turns in the coil, based on equation (3.2), can expressed as:

$$N = \frac{R}{\mathfrak{d} r_c} \, . \tag{3.30}$$

Replacing N from (3.30) in (3.29) permits L to be restated, only based on r_c, as:

$$L = \frac{\mu_o \pi R^2 r_c}{\mathfrak{d} \sqrt{4\mathfrak{d}^2 r_c^4 + R^2 d_w^2}} \, . \tag{3.31}$$

Differentiating (3.31) with respect to r_c provides a coil radius which maximises L:

$$r_c = \sqrt[4]{\frac{R^2 d_w^2}{4\mathfrak{d}^2}} = \frac{l_c}{2} \qquad \Rightarrow \qquad L_{max} = \sqrt[4]{\frac{\mu_o^4 \pi^4 R^6}{16\mathfrak{d}^6 d_w^2}} \, . \tag{3.32}$$

Having obtained the maximum ACC self-inductance value, the next step is to find the optimum R value that can provide maximised magnetic resonant linkage between the Tx and Rx with respect to L_{max}. In selecting a suitable coil ac ohmic resistance, a figure-of-merit parameter (P_{scf}) with respect to condition (3.27) is introduced in (3.33). The value of P_{scf} indicates how strongly the Tx and Rx coils are linked together:

$$P_{scf} = K^2 Q_{L_p} Q_{L_s} \, . \tag{3.33}$$

The parameter P_{scf} is called as *strong coupling factor* and provides a guideline for designing the optimum coil geometry which can maximise PTE.

The FoM parameter P_{scf}, based on the circuit elements, can be expressed as:

$$K^2 Q_{L_p} Q_{L_s} = P_{scf} \qquad \Rightarrow \qquad \omega_o^2 K^2 L^2 = P_{scf}(R + R_s)(R + R_L). \tag{3.34}$$

As the ACC's self-inductance needs to be maximised, we substitute L with L_{max} in (3.34) which yields:

$$\left(\frac{(K\omega_o\mu_o\pi)^2}{4P_{scf}\eth^3 d_w} \right) R^3 - R^2 - (R_s + R_L)R - R_s R_L = 0. \tag{3.35}$$

Solving (3.35) for R determines the ac ohmic resistance which maximises η for a given RIPT system. The solution to (3.35) can be readily found using computational software such as MATLAB. With R established it is then possible to calculate r_c, N and l_c from (3.32) and (3.2).

3.4.1 Discussion

It is worth noting that equation (3.35) indicates the optimal R value is a function of K. The inductive link's coupling coefficient, as presented in (3.20), is dependent on the r_c and d_t [86, 111]. Hence, the smallest variations in the value of coupling coefficient can easily move the system's PTE out of the maximum η ridge.

To determine a unique optimum R value which is robust to K variations in all applications, (3.35) will be solved for $K = 1$. This is because, as can be deduced from (3.34), designing a coil for the highest possible coupling coefficient can ensure the P_{scf} value is large enough to maximise PTE over the range of $0 \leq K \leq 1$. Considering this, (3.35) can be restated as:

$$\left(\frac{(\omega_o\mu_o\pi)^2}{4P_{scf}\eth^3 d_w} \right) R^3 - R^2 - (R_s + R_L)R - R_s R_L = 0. \tag{3.36}$$
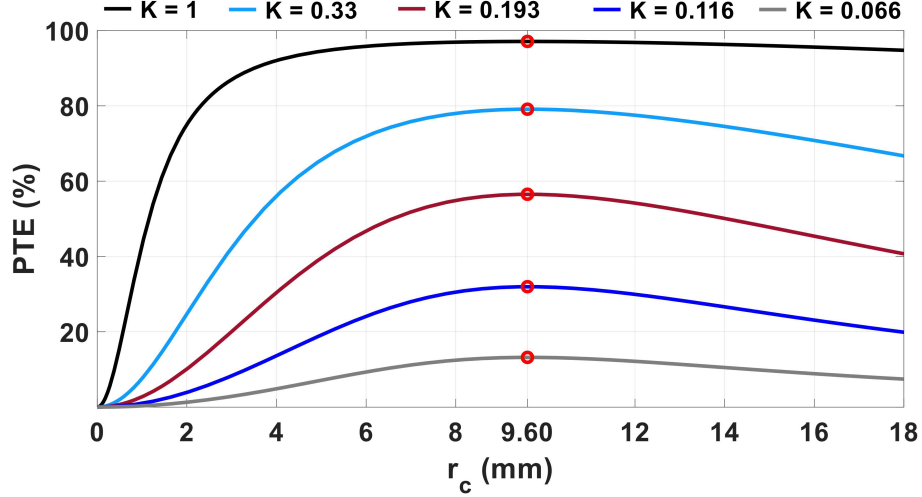
Figure 3.5: Maximum PTE for different coupling coefficients (K) when $P_{scf} = 35$. The red circles indicate the designed ACC geometry for a typical RIPT system ($f_o = 6.78$ MHz, $R_s = 10\,\Omega$ and $R_L = 300\,\Omega$).

To provide an example in this regard, a typical RIPT system similar to Fig. 3.4a, with $R_s = 10\,\Omega$ and $R_L = 300\,\Omega$ at $f_o = 6.78$ MHz has been considered. For the purpose of better graphical presentation, an investigative P_{scf} value of 35 ($P_{scf} = 35$) was selected to calculate ac ohmic resistance from (3.36). For this P_{scf} value $R = 392.69\,m\Omega$, $r_c = 9.60$ mm, $N = 24$ and $l_c = 19.20$ mm. For the given RIPT system, the PTE variations over a range of r_c values have been plotted in Fig. 3.5, with the designed geometry shown by use of red circles. It should be noted that, although the coil geometry was designed for $K = 1$, it provides the maximum PTE for the range of coupling coefficient values (i.e.: $0.066 \leq K \leq 1$.). The value of coupling coefficient $K = 0.066$ has been selected to avoid compression of the graph at low PTE values. In Fig. 3.5, the maximum achievable PTE is seen to drop with a reduction in K. This is expected as coupling reduces. However, the maximum PTE still stays centred around the designed coil geometry (i.e.: $r_c = 9.60$ mm.) thus validating the design approach using the equation (3.36).

Also, it should be noted that identifying the most favourable numerical value of P_{scf} (i.e.: FoM parameter.) is essential to achieve the optimal coil geometry design. A novel method to assist in selection of the P_{scf} value, which is the focus of this work, is provided

in the next chapter.

3.5 Summary

Analytical models to calculate ACC self-inductance and ac ohmic resistance have been presented. The circuit model representing a RIPT system is also shown, which employs the series-series compensation topology. This capacitive compensation scheme is selected to facilitate maximum power transfer efficiency in the magnetic resonant link. For the considered SS inductive link, the equation for PTE is derived and conditions to maximise the efficiency are discussed. Maximising PTE in RIPT systems necessitates having a strong magnetic linkage between the Tx and Rx. Achieving this requires a resonant inductive link with high level of magnetic linkage, Tx/Rx circuitry with high Q_L-factors and a Tx/Rx coil geometry with high Q_i-factor. Among these requirements, geometrical optimisation of the Tx and Rx coil pair is presented as the key parameter to improve PTE. Based on the RIPT system's physical parameters (e.g.: R_s, R_L, etc.) an equation is formulated for PTE. After analysing the derived PTE equation, a unique FoM parameter (i.e.: P_{scf}.) is defined to maximise PTE. The parameter P_{scf} is developed by combining the factors which impact the RIPT system's source-to-load PTE. Identifying the most favourable numerical value for P_{scf} is essential to maximise PTE, which will be discussed further in the next chapter.

CHAPTER 4

OPTIMUM COIL GEOMETRY DESIGN PROCEDURE

In this chapter the effect of FoM parameter (i.e.: strong coupling factor.) on the physical size of the air-cored coil (ACC) and system power transfer efficiency is investigated. A novel iterative design algorithm for proper selection of the FoM's numerical value and the subsequent optimisation of ACC geometry is also presented.

4.1 Strong Coupling Factor Effects

Achieving an optimum coil geometry, which maximises power transfer efficiency of a RIPT system, requires a proper selection method for identifying the numerical value of FoM (i.e.: P_{scf}.) with respect to the RIPT application and its physical size constraints. The design parameter strong coupling factor in addition to influencing the system power transfer, based on (3.36), also affects the ac ohmic resistance of the Tx/Rx ACC pair. The value of ac ohmic resistance directly impacts the coil's physical size and optimum load value (i.e.: R_{L_O}.) based on (3.28). Hence, the strong coupling factor's effect on the physical size of Tx/Rx ACC pair, optimum load value and PTE needs to be investigated further.

4.1.1 Effects of Strong Coupling Factor on ACC Geometry and PTE

To investigate the strong coupling factor's effects, a typical resonant inductive power transfer system, used in [41], with $R_s = 0.1\,\Omega$ and $R_L = 100\,\Omega$ at $f_o = 13.56\,\text{MHz}$ has been considered. As is common [30, 34, 40, 41], for the given RIPT system the ACC's geometrical parameters (i.e.: r_c, N and l_c.) are calculated for three investigative FoM values (i.e.: $P_{scf} = 1550$, 2550 and 3550.) and presented in Table 4.1. Considering the calculated ACC geometries in Table 4.1, the PTE variations of the designed inductive links over a range of r_c values are plotted, using MATLAB, in Fig. 4.1. The RIPT system's coupling coefficient

Table 4.1: Designed ACC geometries and power transfer efficiency for three investigative strong coupling factors.

P_{scf}	R	r_c	N	l_c	η (%) at	η (%) at	η (%) at
	(Ω)	(mm)		(mm)	$K = 0.025$	$K = 0.512$	$K = 1$
1550	0.29	6.90	17	13.80	49.07	99.47	99.65
2550	0.36	7.70	19	15.40	61.23	99.49	99.60
3550	0.42	8.30	21	16.60	68.65	99.48	99.56

values are selected as $K = 0.025$, 0.512 and 1 in Fig. 4.1a – 4.1c to evenly cover the range $0 \leq K \leq 1$. The maximum achievable PTEs are marked with black circles on the curves, while their numerical values are indicated in Table 4.1.

From the graphs and numerical values in the table, it can be deduced that *increasing the strong coupling factor* (i.e.: P_{scf}.) *raises the coil's physical size* while the maximum achievable PTE of the given RIPT system is centred around the designed geometries. It should be noted that there is always a trade-off between reducing the physical size of the coil and increasing PTE for a given K value.

Furthermore, when comparing the figures an observation is that for the inductive link with $K \ll 1$ (i.e.: $K = 0.025$ in Fig. 4.1a.) increasing the design parameter strong coupling factor increases PTE. However as K gets closer to 1, maximum achievable PTE does not necessarily increase with raising strong coupling factor value higher. For example, when $K = 0.512$ (i.e.: Fig. 4.1b.) the system's maximum PTE value for $P_{scf} = 2550$ is higher than the maximum PTE value for $P_{scf} = 3550$, despite the increase in strong coupling factor value. Similarly, in the inductive link with higher K value (i.e.: $K = 1$.), as shown in Fig. 4.1c, maximum PTE will slightly reduce with an increase of strong coupling factor. From Fig. 4.1 it can be concluded that in an inductive link as K gets closer to 1, increasing the strong coupling factor value (i.e.: using physically larger Tx/Rx ACCs.) does not ensure achieving higher PTE levels.
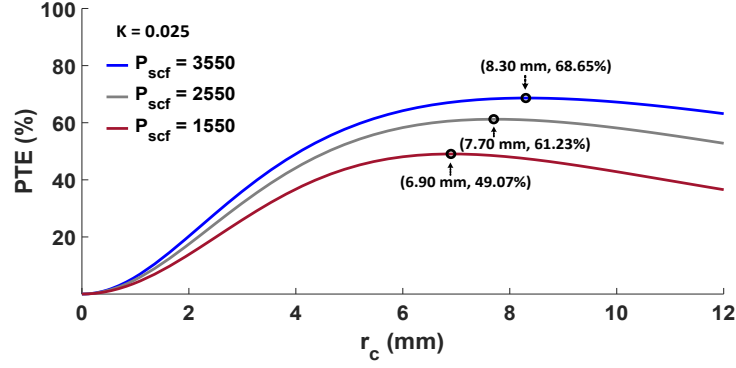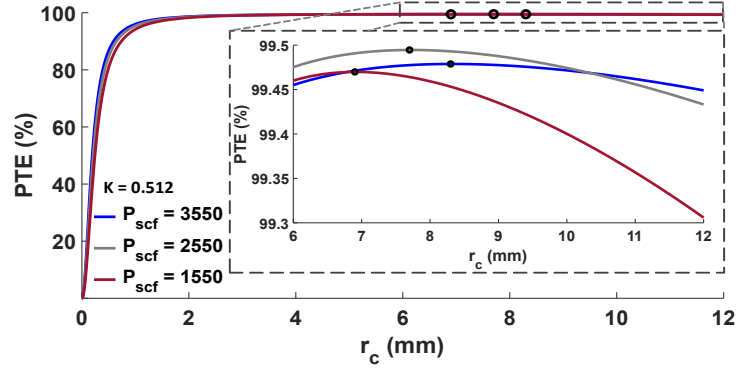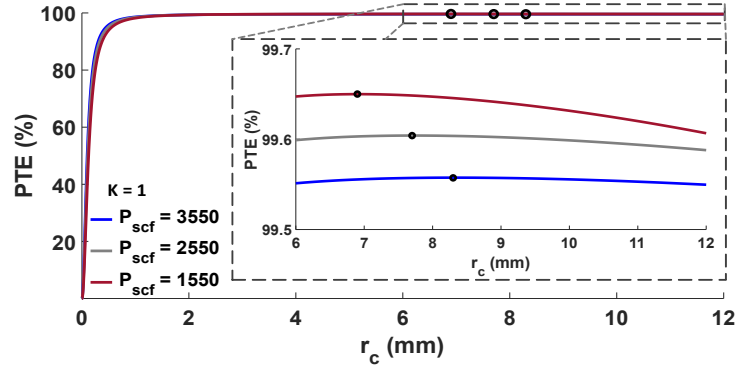
Figure 4.1: Effect of increasing P_{scf} on the physical size of ACC and the system's PTE. Three investigative FoM values ($P_{scf} = 1550$, 2550, and 3550) have been chosen for: (a) $K = 0.025$, (b) $K = 0.512$, and (c) $K = 1$. The curves in (b)–(c) are zoomed in around the points of investigation.

To theoretically analyse this process, equation (3.18) based on P_{scf} will be restated as:

$$P_{scf} = K^2 Q_{L_p} Q_{L_s} \quad \Rightarrow \quad \eta = \frac{P_{scf}}{1 + P_{scf}} \left(\frac{R_L}{R + R_L} \right). \tag{4.1}$$

In a highly coupled inductive link (i.e.: $K \simeq 1$.) the $P_{scf} \gg 1$ is readily achievable. Having $P_{scf} \gg 1$, equation (4.1) can be expressed as:

$$\frac{P_{scf}}{1 + P_{scf}} \simeq 1 \quad \Rightarrow \quad \eta \simeq \frac{R_L}{R + R_L}. \tag{4.2}$$

From (4.2) it can be seen that in an inductive link with a higher P_{scf} value, the coil's ac ohmic resistance, R, is also increased which leads to reduction of PTE.

4.1.2 Effects of Strong Coupling Factor on Optimum Load and PTE

To analyse the effect of strong coupling factor on the system's R_{L_O} value and PTE, the same RIPT system (i.e.: $R_s = 0.1\,\Omega$ and $R_L = 100\,\Omega$ at $f_o = 13.56\,\text{MHz}$ [41].), which is employed in section (4.1.1) with the same investigative FoM values and ACC geometries indicated in Table 4.1 has been considered. For the given system, the optimum load values are calculated from (3.28) and presented in Table 4.2. The coupling coefficient values, employed in the calculations, are $K = 0.025$, 0.5 and 1.

For the given system the PTE variations over a range of load values are plotted in Fig. 4.2. The inductive link's coupling coefficient values are considered as $K = 0.025$, 0.5 and 1 in Fig. 4.2a, 4.2b and 4.2c, respectively. The optimum load values and maximum PTEs achievable at R_{L_O} (i.e.: η_{max}.) are marked with black circles on the curves, while

Table 4.2: Optimum load values and power transfer efficiency for three investigative strong coupling factors.

P_{scf}	R_{L_O} (Ω) at $K = 0.025$	η_{max} (%) at $K = 0.025$	R_{L_O} (Ω) at $K = 0.5$	η_{max} (%) at $K = 0.5$	R_{L_O} (Ω) at $K = 1$	η_{max} (%) at $K = 1$
1550	5.28	89.71	105.54	99.46	211.08	99.73
2550	7.58	90.97	151.38	99.53	302.75	99.76
3550	9.64	91.72	192.60	99.57	385.20	99.78

their numerical values are indicated both on the graphs and in Table 4.2. From Fig. 4.2 it can be seen that increasing strong coupling factor, due to raising R (i.e.: ACC's parasitic resistance.), increases the RIPT system's optimal load value as expressed in (3.28). Also, when comparing the figures, a theme is that with increasing K value, the system's R_{L_O} increases in addition to a raise in power transfer efficiency.
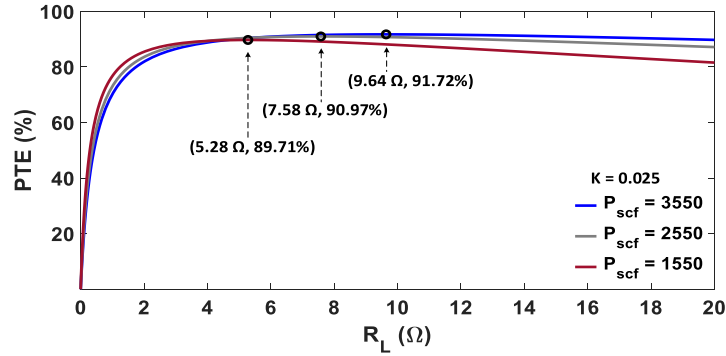
(a)
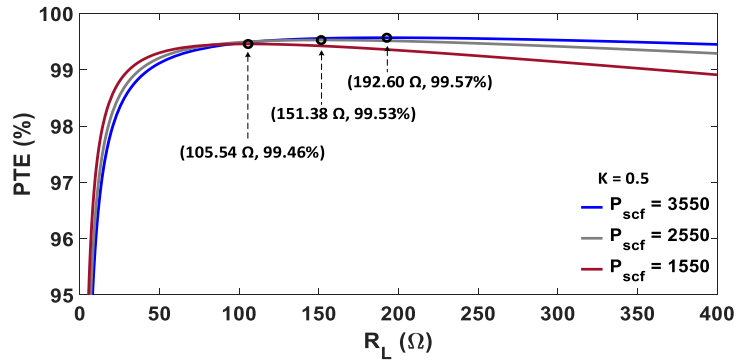
(b)
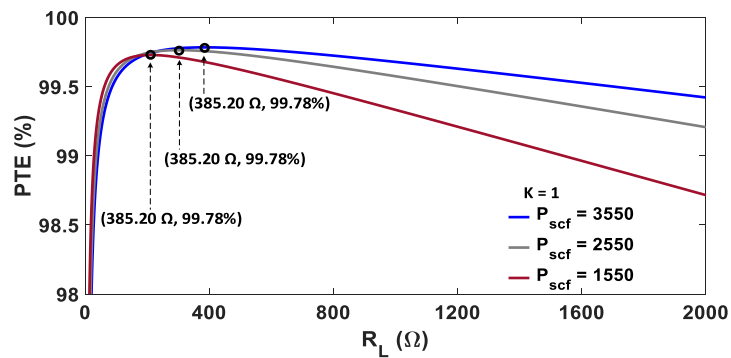
(c)

Figure 4.2: Effect of increasing P_{scf} on the system optimal R_L value. Three investigative strong coupling factor values (P_{scf} = 1550, 2550, and 3550) have been chosen for: (a) $K = 0.025$, (b) $K = 0.5$, and (c) $K = 1$.
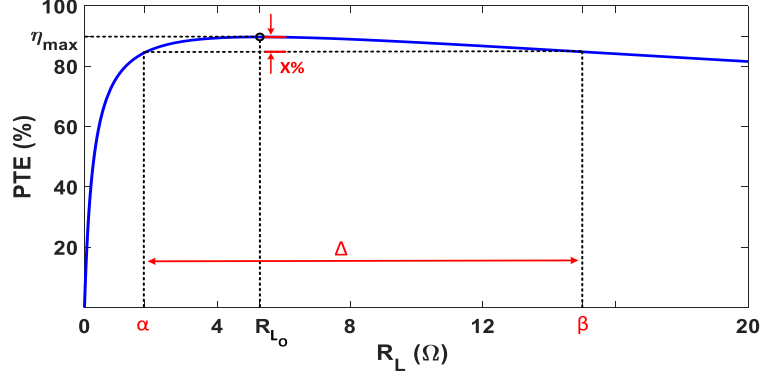
Figure 4.3: Demonstration of the Δ window on the plot of PTE against load variations for the given RIPT system (with $P_{scf} = 1550$ and $K = 0.025$).

In selecting a proper P_{scf} value it should be noted that achieving maximum PTE in a given resonant inductive link requires the system's load to be equal to its optimal value from (3.28). However, it is not always possible to keep R_L fixed at the optimal load value to receive maximum PTE. For example, in a stationary EV charging system charging/discharging of batteries leads to variations in the system's load value [81].

To make the strong coupling factor robust to load variations, a boundary (Δ) around R_{L_O} has been introduced, where the system PTE stays within close proximity of the maximum achievable η (i.e.: η_{max}.), as shown in Fig. 4.3. The proximity range can be any arbitrary value (e.g.: $X\%$.) dependent on the RIPT system's application and requirements. Also, the ranges for the boundary Δ are marked by parameters α and β. The parameter α and β can be respectively calculated from equations (A. 4) and (A. 5), in Appendix A. As far as the physical size limitations permit, the most adequate P_{scf} value for designing an optimum geometry is where the RIPT system's load value sits within the Δ range (i.e.: $\alpha \leq R_L \leq \beta$.). To assist depicting the parameters α, β and the boundary Δ, PTE of the given resonant IPT system for $P_{scf} = 1550$ and $K = 0.025$ over a range of R_L values is shown in Fig. 4.3.

Considering the factors impacting optimum ACC geometry design (i.e.: physical size, required PTE for the given RIPT application and the maximum η achievable at R_{L_O}.), choosing a proper P_{scf} value requires an iterative selection procedure.

55

4.2 Strong Coupling Factor Selection Procedure

In order to find the optimal value for the FoM parameter, a novel iterative algorithm is depicted in Fig. 4.4. The demonstrated design procedure, through selecting a proper P_{scf} value will provide an optimum ACC geometry which maximises PTE for the required RIPT application.

The design algorithm, in Fig. 4.4, starts with taking a set of design constraints and an initial value for the FoM parameter. The design constraints comprise R_s, R_L, f_o, d_w, K, the parameter X and the spatial limitations (i.e.: maximum/minimum r_c and/or maximum/minimum l_c.) which can be determined from the RIPT application and requirements. The FoM parameter can initially take any arbitrary value, because the optimisation algorithm provides the designer with a good sense of how to make necessary changes to the P_{scf} value to maximise PTE. With selecting the initial value for the P_{scf}, the Tx/Rx ACC geometry (i.e.: R, r_c, l_c and N.) can be calculated from equations (3.36), (3.32) and (3.2); ACC's ac ohmic resistance from (3.36), radius and length of the coil from (3.32) and number of turns from (3.2). It should be noted that the parameter $\eth$ in (3.2), depending on the RIPT system's operating frequency (i.e.: f_o.), can be determined either from (3.6) or (3.7). After initially calculating the ACC geometry, the P_{scf} value will be modified in an iterative manner such that the final designed ACC geometry maximises the RIPT system's PTE, besides meeting the application's spatial requirements.

To numerically describe the ACC design algorithm, a mid-frequency RIPT system similar to the system which is employed in [79] for WPT through metallic structures, has been considered where $R_s = 5.77\,\Omega$ and $R_L = 10\,\Omega$ at $f_o = 300\,\text{kHz}$. The coil winding conductor used is $0.511\,\text{mm}$ (diameter) copper wire, and the inductive link's coupling coefficient, K, is 0.2. It has been considered that the Tx/Rx coil diameter must be less than $32\,\text{mm}$ (i.e.: $r_c \leq 16\,\text{mm}$.). To ensure the designed ACC geometry exhibits a high PTE, the chosen proximity range of η_{max} is 10% (i.e.: $X = 10\%$.). The iterative design process is initiated with
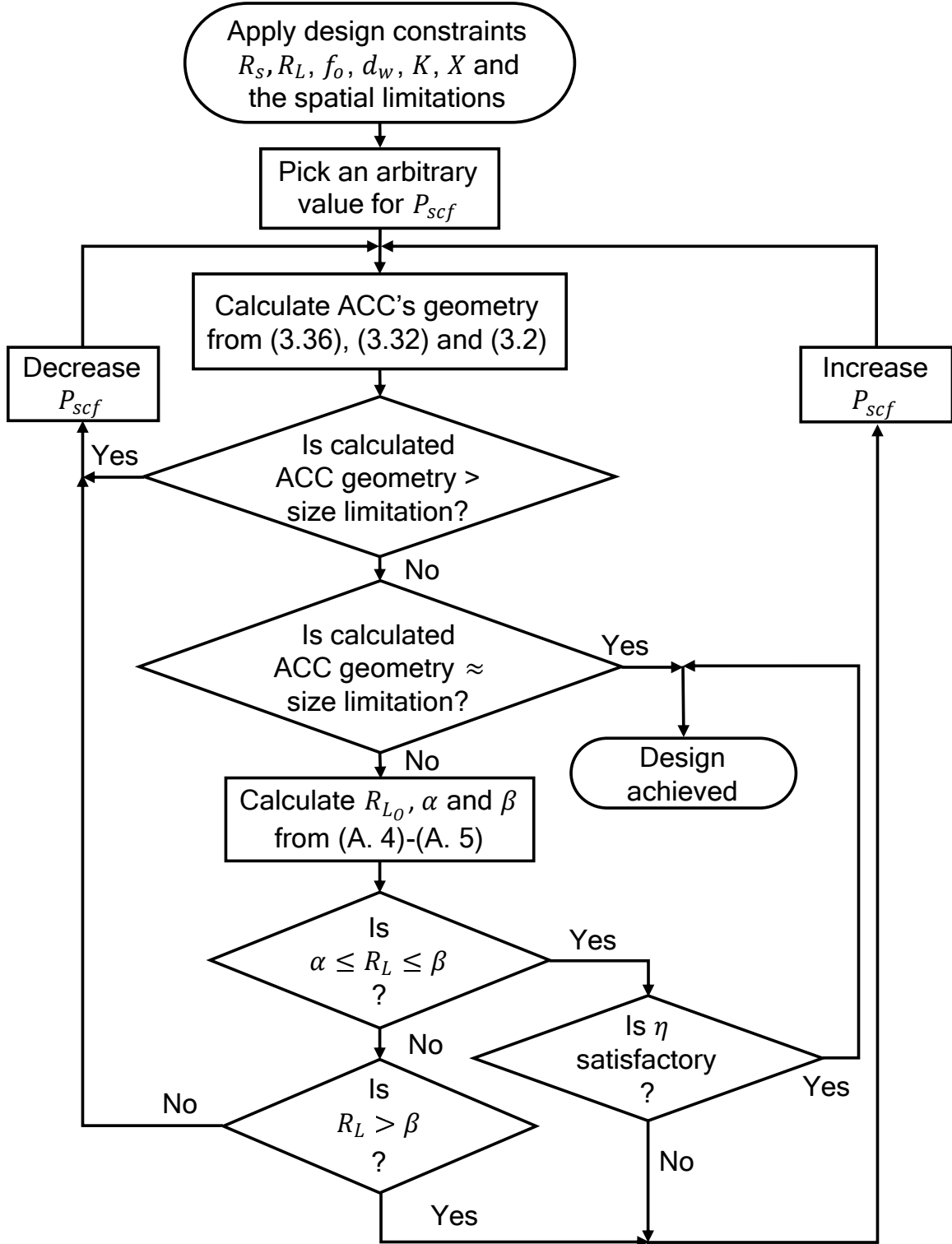
Figure 4.4: Flowchart of design algorithm for air-cored coils.

Table 4.3: Algorithm iterations for RIPT system under consideration ($f_o = 300\,\text{kHz}$, $R_s = 5.77\,\Omega$ and $R_L = 10\,\Omega$).

State #	P_{scf}	R (Ω)	r_c (mm)	N	l_c (mm)	R_{L_O} (Ω)	α (Ω)	β (Ω)	η for R_{L_O}(%)	η for R_L (%)
1	2000	0.98	21.20	83	42.40	-	-	-	-	-
2	1000	0.77	18.70	73	37.40	-	-	-	-	-
3	100	0.34	12.50	49	25.00	3.79	2.03	7.09	83.34	77.34
4	250	0.47	14.70	57	29.40	7.05	3.47	14.34	87.44	86.81
5	400	0.56	16.00	63	32.00	9.71	4.55	20.73	89.16	89.15

considering $P_{scf} = 2000$. Table 4.3 shows some iteration examples for finding the FoM's optimal value. It should be noted that to calculate R, equation (3.6) (i.e.: $\eth = \dfrac{\sqrt{2\omega_o\mu\rho}}{d_w}$.) is used. This is because the application's operating frequency is greater than $66.89\,\text{kHz}$ (i.e.: $f_o > \dfrac{4\rho}{\pi\mu d_w^2}$.).

As shown in Table 4.3, the calculated Tx/Rx coil radius at state 1 is larger than the application's spatial limitation (i.e.: $r_c \leq 16\,\text{mm}$.). Hence, based on the design algorithm, shown in Fig. 4.4, the selected P_{scf} value should be reduced. Considering that the first decision box in the design flowchart is not met in this state, the values for the parameters R_{L_O}, α, β, η for R_{L_O} and η for R_L do not need to be calculated (blank spaces in state 1, Table 4.3). In state 2, the FoM parameter is reduced to $P_{scf} = 1000$. Again, the values for the design parameters R_{L_O}, α, β, η for R_{L_O} and η for R_L do not need to be calculated (blank spaces in state 2, Table 4.3). The calculated r_c for this P_{scf} value is also larger than $16\,\text{mm}$. To fulfil the RIPT application's spatial requirement (i.e.: $r_c \leq 16\,\text{mm}$.), the selected FoM values after two iterations have been reduced to $P_{scf} = 100$. However the ACC geometry designed at state 3 does not provide a desired level of PTE. Hence to improve η, the FoM value has been slightly increased in states 4 and 5. The maximum strong coupling factor value that can meet the application's spatial limitations is $P_{scf} = 400$. For this FoM

Table 4.4: Algorithm iterations for RIPT system under consideration ($f_o = 10\,\text{kHz}$, $R_s = 0.01\,\Omega$ and $R_L = 1\,\text{k}\Omega$).

State #	P_{scf}	R (Ω)	r_c (mm)	N	l_c (mm)	R_{L_O} (Ω)	α (Ω)	β (Ω)	η for R_{L_O}(%)	η for R_L (%)
1	8	2.07	61.80	154	123.60	-	-	-	-	-
2	1	0.73	36.80	92	73.60	24.42	4.25	140.24	94.16	44.72
3	3	1.27	48.40	121	96.80	-	-	-	-	-
4	2	1.04	43.70	109	87.40	-	-	-	-	-
5	1.5	0.89	40.70	102	81.40	-	-	-	-	-
6	1.4	0.87	40.00	100	80.00	31.41	5.17	190.94	94.62	53.09

value, the designed ACC geometry is $r_c = 16\,\text{mm}$, $N = 62$ and $l_c = 32\,\text{mm}$ and the maximum PTE of 89.15% is theoretically achieved. For a similar RIPT system, a solenoid with $r_c = 42\,\text{mm}$, $N = 260$ and $l_c = 152\,\text{mm}$ has been employed, in [79], which can theoretically provide maximum PTE of 75%. A comparison between the coil geometry used in [79] and the coil designed by employing the novel recursive algorithm in Fig. 4.4 shows how the work undertaken in this thesis on development of an ACC design algorithm will benefit future workers, in optimising the physical size and achievable PTE.

As the second example to numerically explore the ACC geometry design procedure, a low-frequency resonant IPT system with $R_s = 0.01\,\Omega$, $R_L = 1\,\text{k}\Omega$ at $f_o = 10\,\text{kHz}$ has been considered, where the Tx/Rx coil length must be less than $80\,\text{mm}$ (i.e.: $l_c \leq 80\,\text{mm.}$). This low-frequency RIPT system has real-life application in relation to WPT to recreational people movers [128]. The coil winding conductor used is $0.8\,\text{mm}$ (diameter) copper wire, and the inductive link's coupling coefficient, K, is 0.9. To ensure the designed coil geometry exhibits a high PTE the chosen proximity range of η_{max} is 10% (i.e.: $X = 10\%.$). The iterative design process is initiated with considering $P_{scf} = 8$. Table 4.4 shows some iteration examples for finding the FoM's optimal value (rational for blank spaces are covered in Table 4.3 discussion). It should be noted that to calculate R, equation (3.7) (i.e.:

$\mathfrak{d} = \dfrac{384\rho + \omega_o\mu d_w^2}{48d_w^2}$.) is used. This is because the application's operating frequency is less than $27.29\,\text{kHz}$ (i.e.: $f_o \leq \dfrac{4\rho}{\pi\mu d_w^2}$.).

As can be seen in Table 4.4, to fulfil the resonant IPT application's spatial requirement (i.e.: $l_c \leq 80\,\text{mm}$.), the selected FoM value in the first iteration has been reduced to $P_{scf} = 1$. In search for an ACC geometry that can provide high level of PTE, the FoM value has been increased/decreased successively in states 3 to 6. The maximum strong coupling factor value that can meet the applications spatial requirement is achieved in state 6 (i.e.: $P_{scf} = 1.4$.). For this FoM value, the designed ACC geometry is $r_c = 40\,\text{mm}$, $N = 100$ and $l_c = 80\,\text{mm}$ and the maximum PTE of 53.09% is theoretically achieved.

4.3 Experimental Results & Validation of ACC Design Procedure

In this section, the novel ACC geometry design methodology, described in Fig. 4.4, is empirically validated over low- and mid-frequency bands. To facilitate practical, bench-top, investigations four typical RIPT systems have been considered with resonance frequencies at: *I)* $1.06\,\text{MHz}$ (i.e.: mid-frequency [119, 120].), *II)* $100\,\text{kHz}$ (i.e.: mid-frequency [119, 120].), *III)* $50\,\text{kHz}$ (i.e.: mid-frequency [119, 120].), and *IV)* $15\,\text{kHz}$ (i.e.: low-frequency [119, 120].).

4.3.1 Design Example of ACC Pair Operating at $1.06\,\text{MHz}$

To experimentally verify correct operation of the provided ACC design technique over the mid-frequency band a resonant inductive power transfer system with $R_s = 3\,\Omega$, $R_L = 3.5\,\Omega$ at $f_o = 1.06\,\text{MHz}$ has been considered, where the Tx/Rx coil length must be less than $19\,\text{mm}$ (i.e.: $l_c \leq 19\,\text{mm}$.). This RIPT system has real-world application in transcutaneous inductive power transmission [30]. The Tx/Rx coupling coefficient, K, is considered 0.215 and the chosen proximity range of η_{max} is 3% (i.e.: $X = 3\%$.). The coil winding conductor used is $0.8\,\text{mm}$ (diameter) copper wire. The $0.8\,\text{mm}$ wire is selected as a suitable diameter

Table 4.5: Algorithm iterations for RIPT system under consideration ($f_o = 1.06$ MHz, $R_s = 3\,\Omega$ and $R_L = 3.5\,\Omega$).

Iteration #	P_{scf}	R (mΩ)	r_c (mm)	N	l_c (mm)	R_{L_O} (Ω)	α (Ω)	β (Ω)	η for R_{L_O}(%)	η for R_L (%)
1	1000	257.93	12.4	31	24.8	-	-	-	-	-
2	500	202.55	11.0	27	22.0	-	-	-	-	-
3	300	169.75	10.1	25	20.2	-	-	-	-	-
4	200	147.64	9.4	23	18.8	2.24	1.09	4.57	87.61	86.59
5	220	152.32	9.5	24	19.0	2.38	1.15	4.90	87.98	87.24

value to give a reasonable ohmic resistance and allow ease of practical construction of the coils in the rest of this chapter. Also, it should be noted that to calculate R, equation (3.6) (i.e.: $\eth = \dfrac{\sqrt{2\omega_o\mu\rho}}{d_w}$.) is used. This is because the application's operating frequency is greater than 27.29 kHz (i.e.: $f_o > \dfrac{4\rho}{\pi\mu d_w^2}$.).

Some iteration examples to find the optimal FoM value for the considered RIPT system are listed in Table 4.5. Following the design procedure (i.e.: the novel ACC design algorithm shown in Fig. 4.4.), the optimal FoM value for the given resonant IPT system is $P_{scf} = 220$ (i.e.: state 5 in Table 4.5.). Selecting this value results in designing a Tx/Rx ACC pair with $r_c = 9.50$ mm, $N = 24$ and $l_c = 19.00$ mm which can provide maximum PTE of 87.24%. Further specifications of the designed geometry including Tx/Rx air-cored coil's self-inductance, parasitic resistance and Q_i-factors are mentioned in Table 4.6.

Table 4.6: Specifications of the prototyped ACC geometry ($r_c = 9.50$ mm, $N = 24$, $l_c = 19.00$ mm at $f_o = 1.06$ MHz).

	L_p (μH)	R_{cp} (mΩ)	Q_{i_p}	L_s (μH)	R_{cs} (mΩ)	Q_{i_s}
Calculated value	7.51	152.32	330.02	7.51	152.32	330.02
Measured value	7.26	153.67	312.18	7.14	155.85	300.27

(a)

(b)
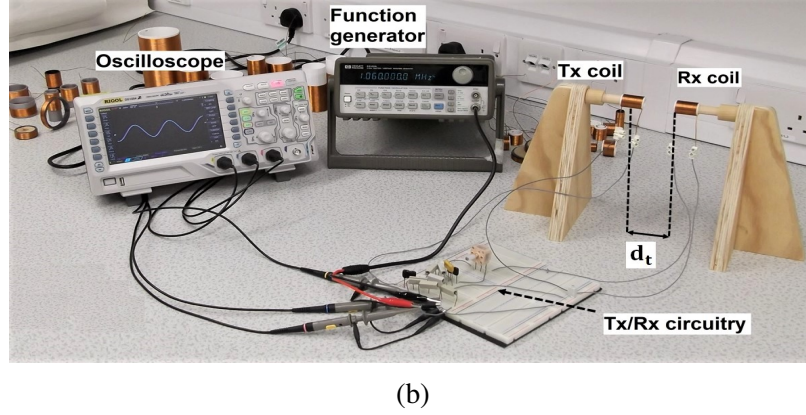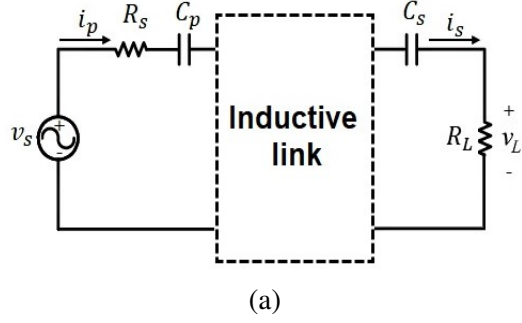
Figure 4.5: PTE measurement setup: (a) Electrical model of the setup, and (b) Experimental test setup (length of coil $= 19.00$ mm, radius of coil $= 9.50$ mm and width apart, d_t, is varied).

To practically investigate the achievable PTE of the designed ACC geometry, a Tx/Rx ACC pair for $P_{scf} = 220$ was physically constructed. The measured L, R and Q_i values of the prototyped air-cored solenoid pair are presented in Table 4.6. The measurements are taken using an electronic LCR meter (Rohde & Schwarz HM8118). The PTE measurements have been carried out on a series-series RIPT system, as shown in Fig. 4.5a (i.e.: the circuit model developed in section (3.2.1).), where compensation capacitors (i.e.: C_p and C_s.), R_s and R_L are directly added to the primary and secondary coils. This technique permits sole PTE evaluation of the designed geometry [30, 41]. For the RIPT system demonstrated in Fig. 4.5a, the utilised experimental set up is shown in Fig. 4.5b, where a function generator (Hewlett Packard 33120A) is used to drive the primary air-cored coil at the resonance frequency (i.e.: 1.06 MHz.). In order to probe the system's energy transmission efficiency, an oscilloscope (Rigol DS1054Z) is used to measure the voltage and
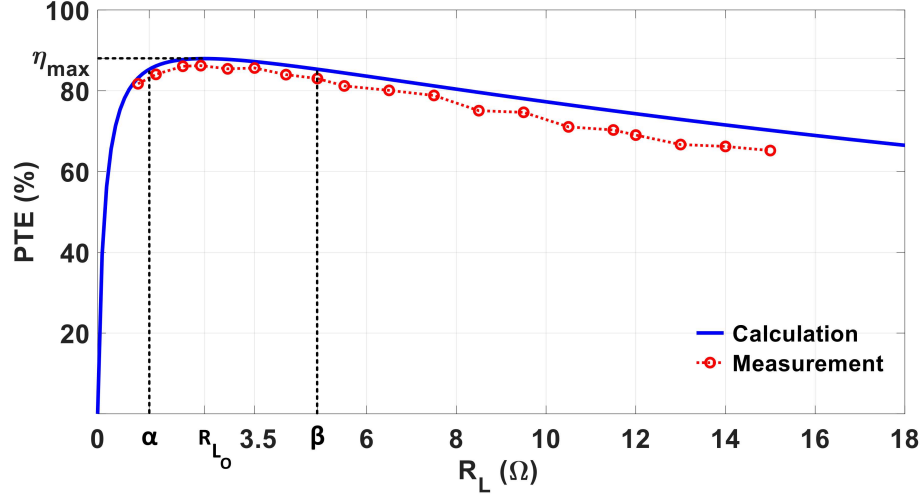
Figure 4.6: The calculated and measured PTE variations over a nominal range of load values. The η_{max}, α and β values are indicated in Table 4.5 (state 5).

current waveforms at the Tx/Rx side. As is common, the transmitted power is found by multiplying the RMS values of the measured voltage and current signals injected into the primary circuitry [30, 79]. The received power is also calculated by measuring the voltage across the load [30, 79].

For the designed ACC geometry, the maximum achievable PTE (i.e.: η_{max}.) is 87.98% at $R_{L_O} = 2.38\,\Omega$. Based on the physical circuit parameters developed in Table 4.5, for all load values between α and β (i.e.: $1.15\,\Omega \leq R_L \leq 4.90\,\Omega$.) the system's PTE will be within 3% of η_{max} (i.e.: $\geq 85.34\%$.). Fig. 4.6 shows the calculated PTE against increasing R_L for the ACC design; set beside this curve are the results taken from practical measurements as R_L is physically increased from $0.9\,\Omega$ to $15\,\Omega$. The measured values show that for all the load resistances within the α and β range, the system's PTE is higher than 81.72% (i.e.: within 7.11% of η_{max}.). The measured results from the physical system show a strong correlation with the calculated results. The calculated and measured PTE for the RIPT application (i.e.: $R_s = 3\,\Omega$ and $R_L = 3.5\,\Omega$.) are 87.24% and 85.63% respectively. The given RIPT system delivers $1.35\,\text{W}$ power to the load when $V_s = 5.66\,v_{rms}$.

Although the Tx/Rx ACC pair are designed for $K = 0.215$, the designed geometry maximises PTE over the range of $0 \leq K \leq 1$ as described in section (3.4.1). To practi-

63
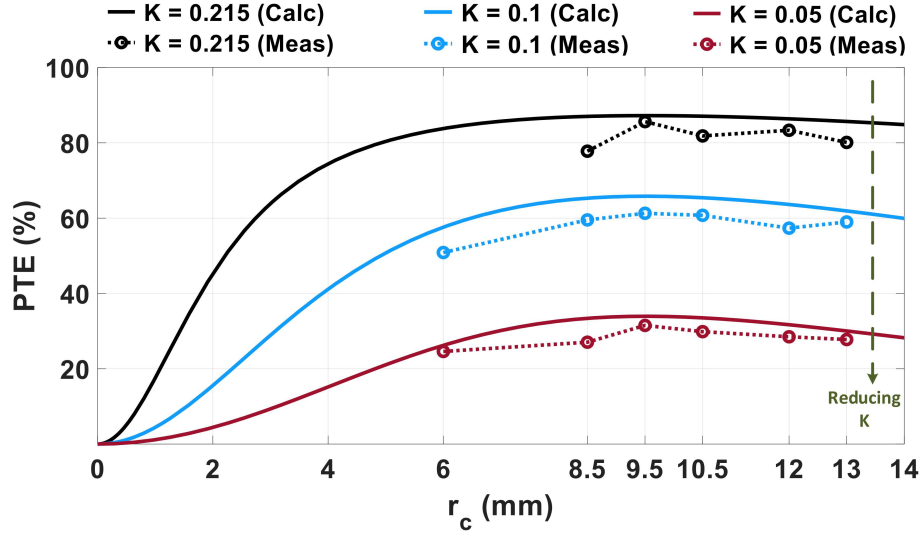
Figure 4.7: Calculated and measured PTE of six sets of coil over three K values from 0.215 to 0.05.

cally prove the concept, six sets of coil, each with different r_c values, have been constructed and their respective PTEs measured for the RIPT application. The three groups of different coloured solid and dashed curves plotted in Fig. 4.7 correspond to calculated and measured PTEs of the designed geometry for three K values between 0.05 to 0.215. The coupling coefficient range has been chosen again to facilitate practical, bench-top, investigation and ease of results gathering. As can be seen in Fig. 4.7, with a fall in coupling coefficient, K, the link becomes more loosely-coupled but the maximum PTE becomes apparent as being around the designed air-cored coil r_c value obtained from the novel design algorithm developed in this research work (i.e.: 9.50 mm.). The experimental PTE value shows closeness to the analytical calculations using MATLAB. Practical tests on physical geometries either side of $r_c = 9.50$ mm show falling PTE over different K values, thus validating the developed ACC design method.

Furthermore, it is worth mentioning that K is highly dependent on the relative distance between the Tx/Rx ACC pairs. To evaluate the functionality of the designed geometry with transmission distance, d_t, variations, calculated and measured PTE values over a d_t range from 10 mm to 32 mm (i.e.: $0.0291 \leq K \leq 0.1938$.) have been compared in Fig. 4.8. From

Figure 4.8: Comparison of PTE between practical measurements and theoretical results for the designed ACC pair over a d_t range from $10\,\text{mm}$ to $32\,\text{mm}$.

Fig. 4.8 it can be deduced that with an increase in transmission distance, the practically measured PTE values attenuate, as can be predicted from the theoretical equations.

4.3.2 Design Example of ACC Pair Operating at $100\,\text{kHz}$

As the second example to practically validate the ACC design technique over the mid-frequency band, a RIPT system with $R_s = 3\,\Omega$, $R_L = 20\,\Omega$ at $f_o = 100\,\text{kHz}$ has been considered, where the Tx/Rx coil diameter must be less than $92\,\text{mm}$ (i.e.: $r_c \leq 46\,\text{mm}$.). The considered system has application in underwater wireless power transfer industry [129]. The coil winding conductor used in this RIPT system is $0.8\,\text{mm}$ (diameter) copper wire. The Tx/Rx coupling coefficient, K, is 0.05 and the chosen proximity range of η_{max} is 3% (i.e.: $X = 3\%$.).

Some iteration examples to find the optimal FoM value for the given resonant IPT system are listed in Table 4.7. It should be noted that to calculate R, equation (3.6) (i.e.: $\eth = \dfrac{\sqrt{2\,\omega_o \mu \rho}}{d_w}$.) is used. This is because the application's operating frequency is greater than $27.29\,\text{kHz}$ (i.e.: $f_o > \dfrac{4\rho}{\pi \mu d_w^2}$.). Following the design procedure, the optimal FoM value for the considered RIPT system is $P_{scf} = 3200$ (i.e.: iteration 4 in Table 4.7.). Selecting this value results in designing an air-cored solenoid with $r_c = 45.70\,\text{mm}$, $N = 114$ and

Table 4.7: Algorithm iterations for RIPT system under consideration ($f_o = 100\,\text{kHz}$, $R_s = 3\,\Omega$ and $R_L = 20\,\Omega$).

State #	P_{scf}	R (Ω)	r_c (mm)	N	l_c (mm)	R_{LO} (Ω)	α (Ω)	β (Ω)	η for R_{LO}(%)	η for R_L (%)
1	500	0.55	32.70	81	65.40	3.80	2.25	6.41	74.7	54.07
2	2500	0.98	43.70	109	87.40	11.40	6.02	21.61	84.11	82.16
3	3500	1.11	46.50	116	93.00	-	-	-	-	-
4	3200	1.08	45.70	114	91.40	13.37	6.93	25.79	85.07	84.11

$l_c = 91.40\,\text{mm}$ which can provide maximum PTE of 84.11%. To practically investigate the achievable PTE of the designed ACC geometry, a Tx/Rx solenoid pair for $P_{scf} = 3200$ has been constructed. The calculated and measured values for the Tx/Rx ACC's self-inductance, parasitic resistance and Q_i-factors are presented in Table 4.8.

The PTE measurements have been carried out on the series-series RIPT system shown in Fig. 4.5a. For the RIPT system demonstrated in Fig. 4.5a, the utilised experimental set up is shown in Fig. 4.9, where a function generator (Hewlett Packard 33120A) is used to drive the primary coil at the resonance frequency (i.e.: $100\,\text{kHz}$.). In order to probe the system's energy transmission efficiency, an oscilloscope (Rigol DS1054Z) is used to measure the voltage and current waveforms at the Tx/Rx side [30, 79].

The prototyped Tx/Rx air-cored coil pair is designed to provide PTE of 84.11% when the coupling coefficient between the pair is $K = 0.05$. However, as described in section

Table 4.8: Specifications of the prototyped ACC geometry ($r_c = 45.70\,\text{mm}$, $N = 114$, $l_c = 91.40\,\text{mm}$ at $f_o = 100\,\text{kHz}$).

	L_p (m H)	R_{cp} (Ω)	Q_{i_p}	L_s (m H)	R_{cs} (Ω)	Q_{i_s}
Calculated value	0.835	1.08	486.22	0.835	1.08	486.22
Measured value	0.794	1.80	280.18	0.802	1.85	270.10
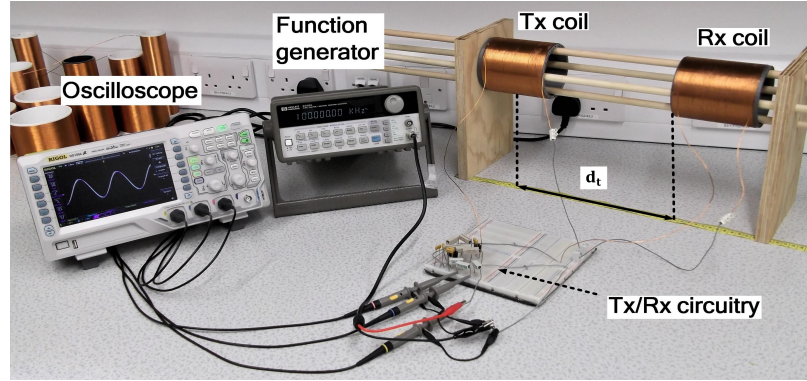
Figure 4.9: Experimental PTE test setup for the RIPT system with Tx/Rx air-cored coils (length of coil $= 91.40$ mm, radius of coil $= 45.70$ mm and width apart, d_t, is varied).

(3.4.1), the designed geometry maximises PTE over the range of $0 \leq K \leq 1$. To practically prove the concept, seven sets of coil, each with different r_c values, have been constructed and their respective PTEs measured for the given RIPT application. The four groups of different coloured solid and dashed curves plotted in Fig. 4.10 correspond to calculated and measured PTEs of the designed ACC geometry for four K values between 0.0125 to 0.1. The coupling coefficient range has been chosen again to facilitate practical, bench-top, investigation and ease of results gathering. As can be seen in Fig. 4.10, with a fall in coupling coefficient, K, the resonant inductive link becomes more loosely-coupled but the

Figure 4.10: Calculated and measured PTE of seven sets of coil over four K values from 0.1 to 0.0125.

Figure 4.11: Comparison of PTE between practical measurements and theoretical results for the designed ACC pair.

maximum PTE becomes apparent as being around the designed coil r_c value (i.e.: 45.70 mm.). The experimental PTE value shows closeness to the analytical calculations using MAT-LAB. Practical tests on physical geometries either side of $r_c = 45.70$ mm show falling PTE over different K values, thus again validating the novel design method proposed under this work.

It is worth mentioning that K is highly dependent on the relative distance between the Tx/Rx ACC pairs. To evaluate the functionality of the designed geometry with transmission distance, d_t, variations, calculated and measured PTE values over a d_t range from 50.1 mm to 200.7 mm (i.e.: $0.0176 \leq K 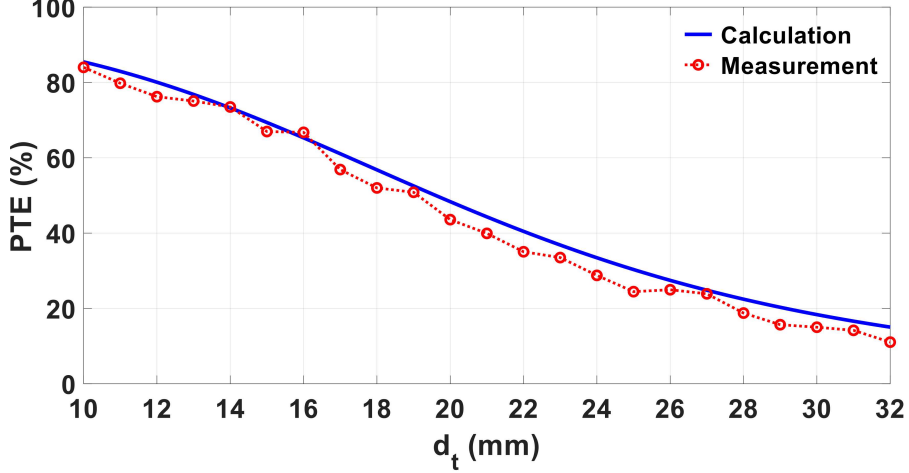\leq 0.1845$.) have been compared in Fig. 4.11. From Fig. 4.11 it can be deduced that with an increase in transmission distance, the practically measured PTE values attenuate, as can be predicted from the theoretical equations.

Furthermore, for the designed ACC geometry, the maximum achievable PTE (i.e.: η_{max}.) is 85.07% at $R_{L_O} = 13.37\,\Omega$. Based on the physical circuit parameters developed in Table 4.7, for all load values between α and β (i.e.: $6.93\,\Omega \leq R_L \leq 25.79\,\Omega$.) the system's PTE will be within 3% of η_{max} (i.e.: $\geq 82.52\%$.). Fig. 4.12 shows the calculated PTE against increasing R_L for the ACC design; set beside this curve are the results taken from practical measurements as R_L is physically increased from $3\,\Omega$ to $33.1\,\Omega$. The mea-
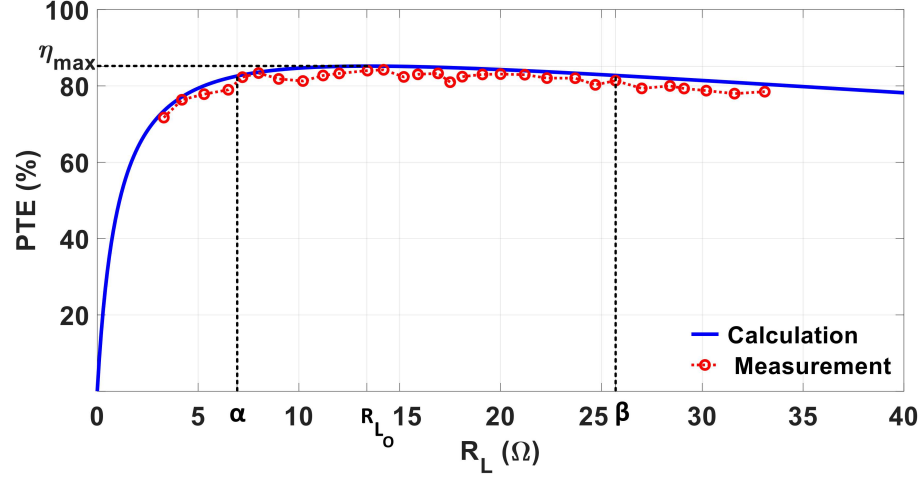
Figure 4.12: The calculated and measured PTE variations over a nominal range of load values. The η_{max}, α and β values are indicated in Table 4.7 (state 4).

sured values show that for all the load resistances within the α and β range, the system's PTE is higher than 80% (i.e.: within 6% of η_{max}.). The measured results from the physical system again show a very strong correlation with the calculated results. The calculated and measured PTE for the RIPT application (i.e.: $R_s = 3\,\Omega$ and $R_L = 20\,\Omega$.) are 84.11% and 83.10% respectively. The given RIPT system delivers $1.06\,\mathrm{W}$ power to the load when $V_s = 3.53\,v_{rms}$.

4.3.3 Design Example of ACC Pair Operating at $50\,\mathrm{kHz}$

The third mid-frequency example considered to practically verify the correct operation of the design technique developed in Fig. 4.4 is a RIPT system with $R_s = 0.15\,\Omega$, $R_L = 1.5\,\Omega$ at $f_o = 50\,\mathrm{kHz}$, where the Tx/Rx ACC length must be less than $25\,\mathrm{mm}$ (i.e.: $l_c \leq 25\,\mathrm{mm}$.). This mid-frequency RIPT system has industrial application in wireless charging of batteries in sensors which are employed to monitor variables associated with the transport of fruits [15]. The Tx/Rx coupling coefficient, K, is considered 0.2 and the chosen proximity range of η_{max} is 10% (i.e.: $X = 10\%$.). The coil winding conductor used is $0.8\,\mathrm{mm}$ (diameter) copper wire. It should be noted that to calculate R, equation (3.6) (i.e.: $\mathfrak{d} = \dfrac{\sqrt{2\omega_o\mu\rho}}{d_w}$.) is used. This is because the application's operating frequency is greater than $27.29\,\mathrm{kHz}$ (i.e.:

Table 4.9: Algorithm iterations for RIPT system under consideration ($f_o = 50\,\text{kHz}$, $R_s = 0.15\,\Omega$ and $R_L = 1.5\,\Omega$).

State #	P_{scf}	R (Ω)	r_c (mm)	N	l_c (mm)	R_{L_O} (Ω)	α (Ω)	β (Ω)	η for R_{L_O}(%)	η for R_L (%)
1	200	0.077	14.60	36	29.20	-	-	-	-	-
2	100	0.059	12.80	32	25.60	-	-	-	-	-
3	50	0.046	11.20	28	22.40	0.38	0.14	1.06	78.38	64.68
4	80	0.055	12.30	30	24.60	0.52	0.18	1.55	81.10	73.51
5	88.7	0.057	12.50	31	25.00	0.56	0.19	1.69	81.65	75.15

$$f_o > \frac{4\rho}{\pi\mu d_w^2}.).$$

Some iteration examples to find the optimal P_{scf} value for the given RIPT system are listed in Table 4.9. Following the ACC design procedure, the optimal FoM value for the considered resonant IPT system is $P_{scf} = 88.7$ (i.e.: state 5 in Table 4.9.). Selecting this value results in designing an ACC pair with $r_c = 12.50\,\text{mm}$, $N = 31$ and $l_c = 25.00\,\text{mm}$ which can provide maximum PTE of 81.65%. To practically investigate the achievable PTE of the coil geometry designed, a Tx/Rx ACC pair for $P_{scf} = 88.7$ has been physically constructed. The calculated and measured values for the Tx/Rx ACC's L, R and Q_i are listed in Table 4.10.

The physically constructed Tx/Rx air-cored solenoid pair is designed to provide PTE of 75.15% when the coupling coefficient between the Tx and Rx coils is $K = 0.2$. However,

Table 4.10: Specifications of the prototyped ACC geometry ($r_c = 12.50\,\text{mm}$, $N = 31$, $l_c = 25.00\,\text{mm}$ at $f_o = 50\,\text{kHz}$).

	L_p (μH)	R_{cp} (mΩ)	Q_{i_p}	L_s (μH)	R_{cs} (mΩ)	Q_{i_s}
Calculated value	17.01	56.91	93.90	17.01	56.91	93.90
Measured value	16.64	63.75	80.57	16.68	64.11	79.21
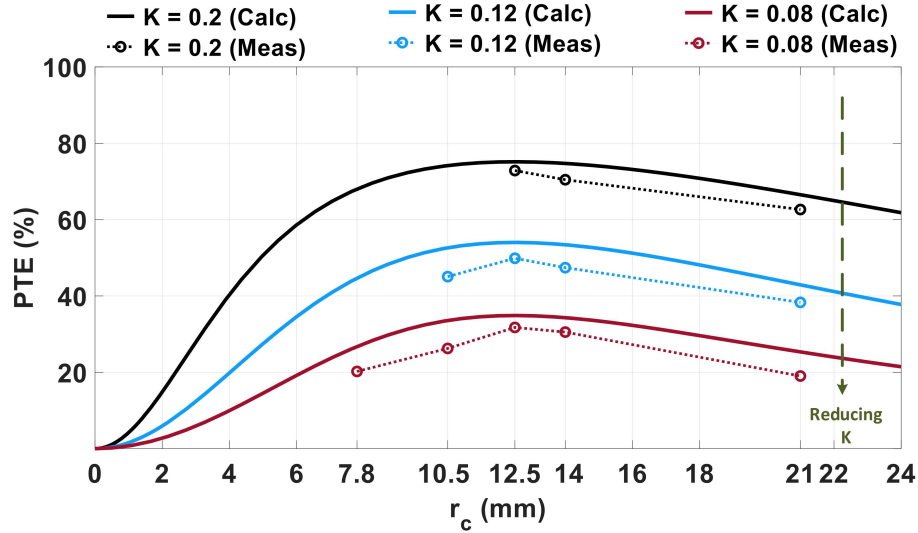
Figure 4.13: Calculated and measured PTE of five sets of coil over three K values from 0.2 to 0.08.

the designed geometry maximises PTE over the range of $0 \leq K \leq 1$. To experimentally prove the concept for the designed ACC geometry in this section, five sets of solenoid, each with different r_c values, have been constructed and their respective PTEs measured for the RIPT application. The calculated and measured PTEs of the constructed ACC geometries are plotted in Fig. 4.13. It should be noted that PTE measurements have been carried out using the similar technique employed in section (4.3.1). In Fig. 4.13 three groups of different coloured solid and dashed curves correspond to calculated and measured PTEs of the designed geometry for three K values between 0.08 to 0.2. The coupling coefficient range has been chosen again to facilitate practical, bench-top, investigation and ease of results gathering. As can be seen in Fig. 4.13, with a fall in coupling coefficient, K, the link becomes more loosely-coupled but the maximum PTE becom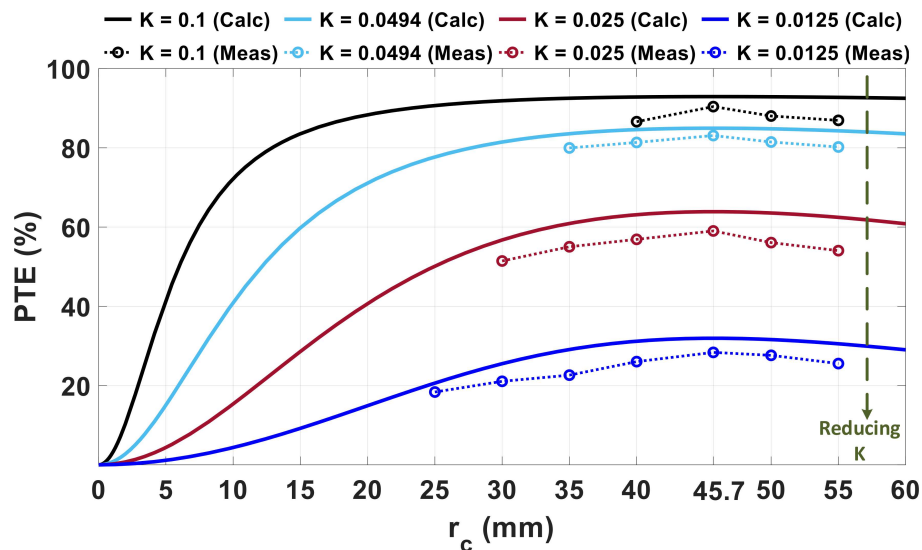es apparent as being around the designed air-cored coil r_c value (i.e.: 12.50 mm.). The experimental PTE value shows closeness to the analytical calculations using MATLAB. Practical tests on physical ACC geometries either side of $r_c = 12.50$ mm show falling PTE over different K values, thus validating the optimum ACC design method over mid-frequency band.

It is worth mentioning that K is highly dependent on the relative distance between the
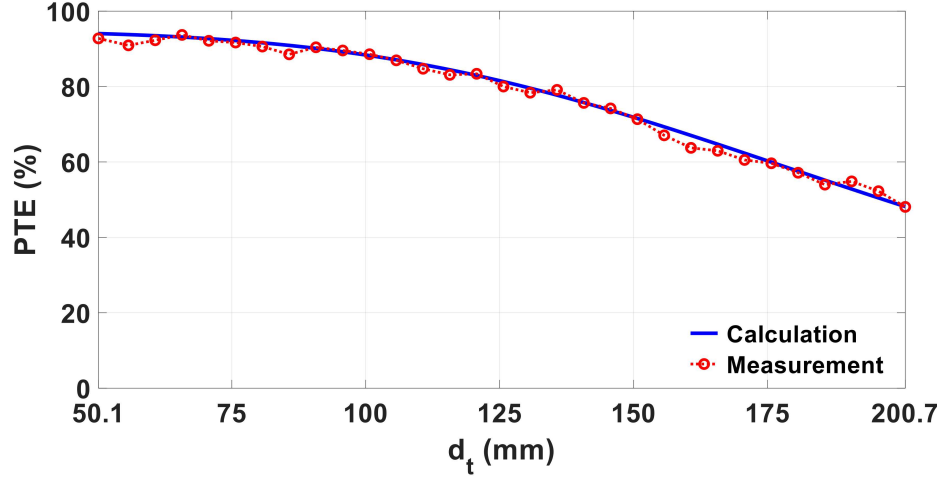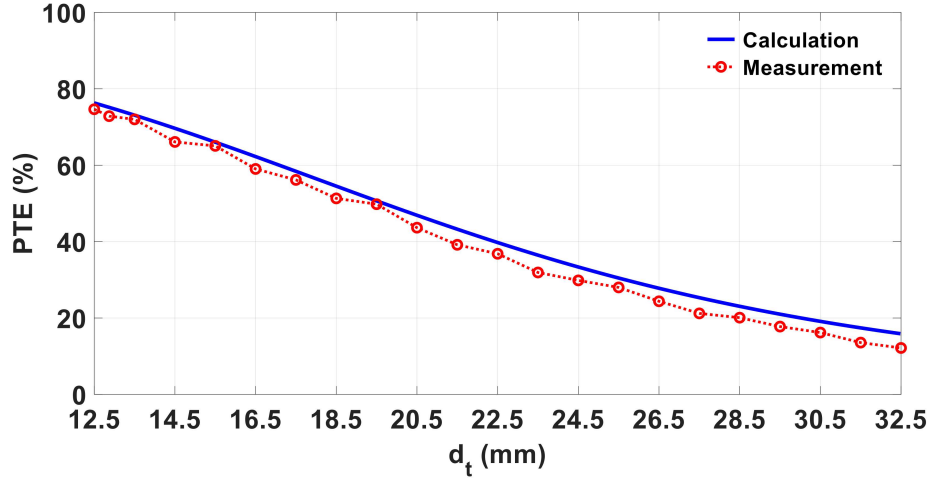
Figure 4.14: Comparison of PTE between practical measurements and theoretical results for the designed ACC pair over a d_t range from $12.5\,\text{mm}$ to $32.5\,\text{mm}$.

Tx/Rx ACC pair. To evaluate the functionality of the designed geometry with variations of transmission distance, calculated and measured PTE values over a d_t range from $12.5\,\text{mm}$ to $32.5\,\text{mm}$ (i.e.: $0.0472 \leq K \leq 0.2071$.) have been compared in Fig. 4.14. From Fig. 4.14 it can be deduced that with an increase in transmission distance, the practically measured PTE values attenuate, as can be predicted from the theoretical equations.

Furthermore, for the designed ACC geometry, the maximum achievable PTE (i.e.: η_{max}.) is 81.65% at $R_{L_O} = 0.56\,\text{m}\Omega$. Based on the physical circuit parameters developed in Table 4.9, for all load values between α and β (i.e.: $0.19\,\Omega \leq R_L \leq 1.69\,\Omega$.) the system's PTE will be within 10% of η_{max} (i.e.: $\geq 73.48\%$.). Fig. 4.15 shows the calculated PTE against increasing R_L for the coil design; set beside this curve are the results taken from practical measurements as R_L is physically increased from $0.11\,\Omega$ to $8.5\,\Omega$. The measured values show that for all the load resistances within the α and β range, η is higher than 70.01% (i.e.: within 14.26% of η_{max}.). The measured results from the physical system show good correlation with the calculated results. The calculated and measured PTE for the RIPT application (i.e.: $R_s = 0.15\,\Omega$ and $R_L = 1.5\,\Omega$.) are 75.15% and 72.85% respectively. The given RIPT system delivers $1.03\,\text{W}$ power to the load when $V_s = 1.41\,v_{rms}$.
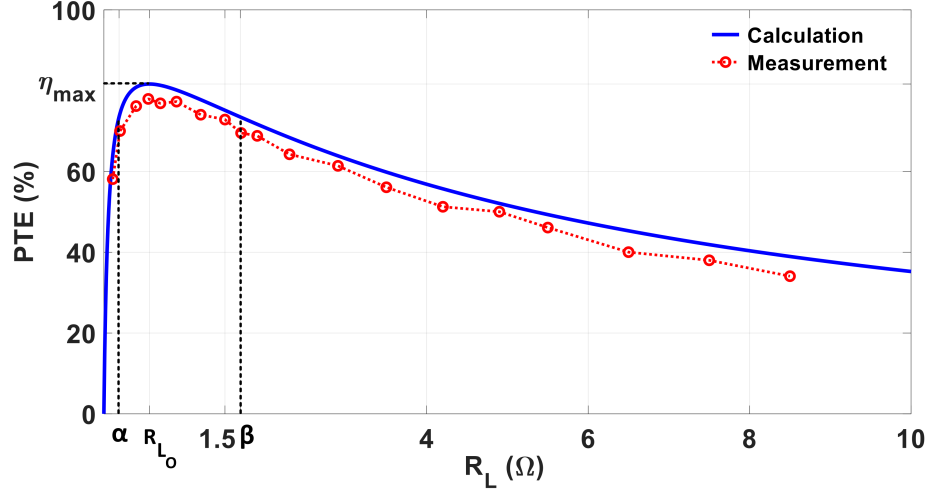
Figure 4.15: The calculated and measured PTE variations over a nominal range of load values. The η_{max}, α and β values are indicated in Table 4.9 (state 5).

4.3.4 Design Example of ACC Pair Operating at $15\,\mathrm{kHz}$

To experimentally verify functionality of the developed ACC design technique over the low-frequency band, a RIPT system with $R_s = 3\,\Omega$, $R_L = 0.4\,\Omega$ at $f_o = 15\,\mathrm{kHz}$ has been considered, where the Tx/Rx coil length must be less than 45 mm (i.e.: $l_c \leq 45\,\mathrm{mm}$.). This low-frequency RIPT system has real-world application in electric vehicle battery chargers [18, 20]. The coil winding conductor used in the considered RIPT system is $0.8\,\mathrm{mm}$ (diameter) copper wire. The Tx/Rx coupling coefficient, K, is 0.2 and the chosen proximity range of η_{max} is 6% (i.e.: $X = 6\%$.).

Some iteration examples to find the optimal FoM value for the given RIPT system are listed in Table 4.11. It should be noted that to calculate R, equation (3.7) (i.e.: $\eth = \dfrac{384\rho + \omega_o\mu d_w^2}{48 d_w^2}$.) is used. This is because the application's operating frequency is less than $27.29\,\mathrm{kHz}$ (i.e.: $f_o \leq \dfrac{4\rho}{\pi\mu d_w^2}$.). Following the developed ACC design procedure in Fig. 4.4, the optimal FoM value for the considered resonant IPT system is $P_{scf} = 39.73$ (i.e.: state 5 in Table 4.11.). Selecting this value results in designing an air-cored coil pair with $r_c = 22.50\,\mathrm{mm}$, $N = 56$ and $l_c = 45.00\,\mathrm{mm}$ which can provide maximum PTE of 37.72%. To practically investigate the achievable PTE of the ACC geometry designed, a Tx/Rx ACC

73

Table 4.11: Algorithm iterations for RIPT system under consideration ($f_o = 15\,\text{kHz}$, $R_s = 3\,\Omega$ and $R_L = 0.4\,\Omega$).

State #	P_{scf}	R (Ω)	r_c (mm)	N	l_c (mm)	R_{L_O} (Ω)	α (Ω)	β (Ω)	η for R_{L_O}(%)	η for R_L (%)
1	100	0.40	27.20	68	54.40	-	-	-	-	-
2	50	0.30	23.60	59	47.20	-	-	-	-	-
3	25	0.23	20.50	51	41.00	0.44	0.26	0.75	31.82	31.74
4	35	0.26	22.00	55	44.00	0.56	0.33	0.95	36.08	35.21
5	39.73	0.28	22.50	56	45.00	0.61	0.36	1.05	37.72	36.31

pair for $P_{scf} = 39.73$ has been physically constructed. The calculated and measured L, R and Q_i values of the prototyped air-cored solenoid pair are listed in Table 4.12.

The PTE measurements have been carried out using the similar technique employed in section (4.3.1). For the designed ACC geometry, the maximum achievable PTE (i.e.: η_{max}.) is 37.72% at $R_{L_O} = 0.61\,\Omega$. Based on the physical circuit parameters developed in Table 4.11, for all load values between α and β (i.e.: $0.36\,\Omega \leq R_L \leq 1.05\,\Omega$.) the system's PTE will be within 6% of η_{max} (i.e.: $\geq 35.46\%$.). Fig. 4.16 shows the calculated PTE against increasing R_L for the air-cored coil design; set beside this curve are the results taken from practical measurements as R_L is physically increased from $0.15\,\Omega$ to $4.90\,\Omega$. The measured values show that for all the load resistances within the α and β range, the system's PTE is higher than 32.89% (i.e.: within 12.80% of η_{max}.). The measured results from the physical

Table 4.12: Specifications of the prototyped ACC geometry ($r_c = 22.50\,\text{mm}$, $N = 56$, $l_c = 45.00\,\text{mm}$ at $f_o = 15\,\text{kHz}$).

	L_p (μH)	R_{cp} (mΩ)	Q_{i_p}	L_s (μH)	R_{cs} (mΩ)	Q_{i_s}
Calculated value	99.54	276.20	33.97	99.54	276.20	33.97
Measured value	89.61	286.15	28.23	90.83	289.52	29.07
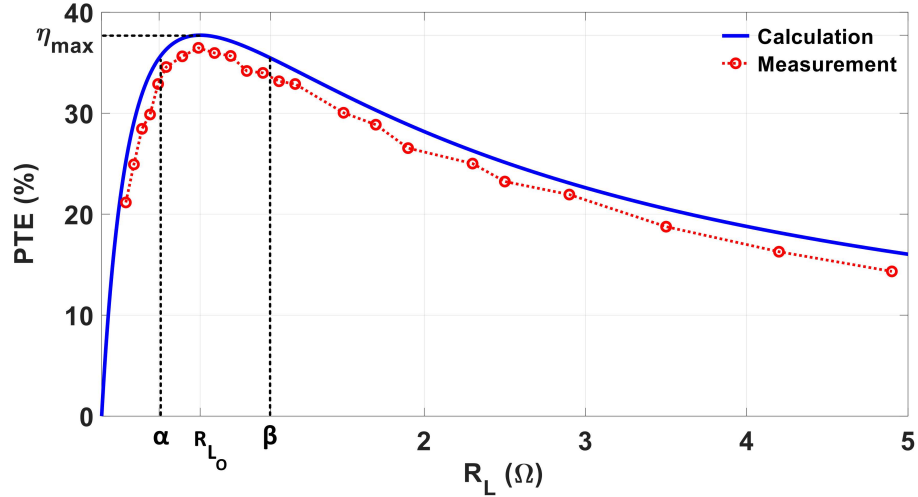
Figure 4.16: The calculated and measured PTE variations over a nominal range of load values. The η_{max}, α and β values are indicated in Table 4.11 (state 5).

system again show very strong correlation with the calculated results. The calculated and measured PTE for the RIPT application (i.e.: $R_s = 3\,\Omega$ and $R_L = 0.4\,\Omega$.) are 36.31% and 34.57% respectively. The given RIPT system delivers $1.15\,\text{W}$ power to the load when $V_s = 4.24\,v_{rms}$.

Although the Tx/Rx ACC pair are designed for $K = 0.2$, the designed geometry max-imises PTE over the range of $0 \leq K \leq 1$ as described in section (3.4.1). To practically prove the concept at low-frequency band, six sets of coil, each with different r_c values, have been constructed and their respective PTEs measured for the RIPT application. The three groups of different coloured solid and dashed curves plotted in Fig. 4.17 correspond to calculated and measured PTEs of the designed geometry for three K values between 0.1 to 0.2. The coupling coefficient range has been chosen again to facilitate practical, bench-top, investigation and ease of results gathering. As can be seen in Fig. 4.17, with a fall in coupling coefficient, K, the link becomes more loosely-coupled but the maximum PTE becomes apparent as being around the designed air-cored coil r_c value obtained from the novel design algorithm developed in this research work (i.e.: $22.50\,\text{mm}$.). The experimen-tal PTE value shows remarkable closeness to the analytical calculations using MATLAB. Practical tests on physical geometries either side of $r_c = 22.50\,\text{mm}$ show falling PTE over

75
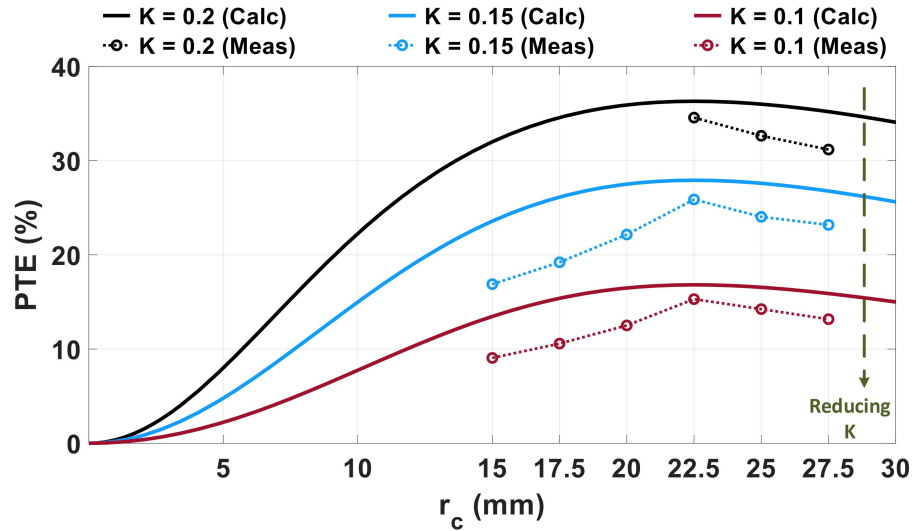
Figure 4.17: Calculated and measured PTE of six sets of coil over three K values from 0.2 to 0.1.

different K values, thus validating correct operation of the ACC design method presented in Fig. 4.4.

Furthermore, it is worth mentioning that K is highly dependent on the relative distance between the Tx/Rx coil pairs. To evaluate the functionality of the designed geometry with transmission distance, d_t, variations, calculated and measured PTE values over a d_t range from 22.5 mm to 44.5 mm (i.e.: $0.076 \leq K \leq 0.207$.) have been compared in Fig. 4.18. From Fig. 4.18 it can be deduced that with an increase in transmission distance, the practically measured PTE values attenuate, as can be predicted from the theoretical equations.

It is worth noting that the maximum achievable PTE for the given RIPT system is less than 38%. This complies with the fundamentals of antenna design theory, based on which achieving higher PTE levels at such low operating frequency ranges necessitates employing physically large Tx/Rx coil pair.

4.3.5   Discussion

Comparing the experimental results in sections $(4.3.1) - (4.3.4)$ shows that for the given RIPT systems, maximum PTE is achieved at the designed ACC geometries. Hence, it can
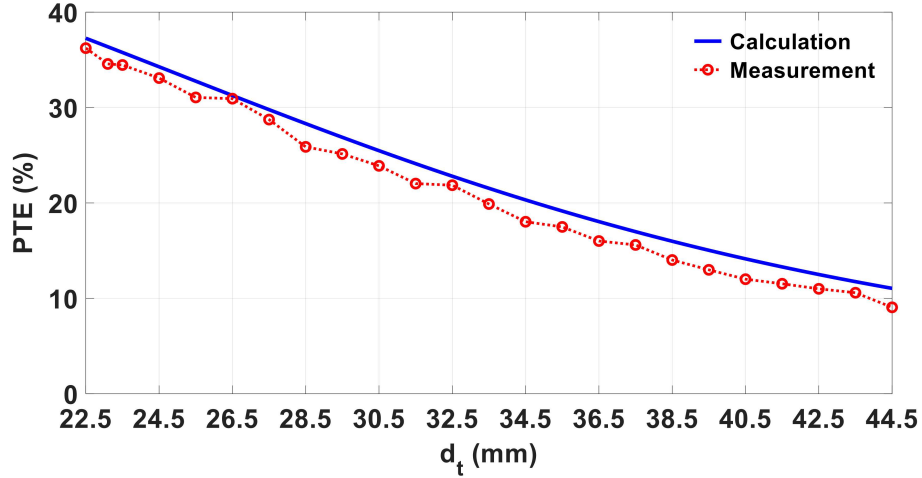
Figure 4.18: Comparison of PTE between practical measurements and theoretical results for the designed ACC pair over a d_t range from 22.5 mm to 44.5 mm.

be concluded that the optimum ACC geometries, which are designed using the novel iterative algorithm presented in this chapter (i.e.: Fig. 4.4.), demonstrate a consistent WPT performance over the low- and mid-frequency bands. From the experimental design examples, it is also observed that as the RIPT application's operating frequency is decreased, achieving high PTE levels necessitates employing physically larger Tx/Rx coils. Meeting this requirement is not feasible in many RIPT applications due to the spatial limitations often encountered. An alternative method to increase PTE to the desired level is to add ferrite cores to the Tx/Rx coil pair, which will be further discussed in the next chapter.

4.4 Summary

The effect of strong coupling factor on the RIPT system's PTE and the ac ohmic resistance has been analysed. It has been identified that the parameter P_{scf}, by influencing the R value, impacts the ACC's physical size and R_{L_O}. A typical RIPT system has been considered to analyse the effects of three investigative FoM values on the ACC's geometrical parameters, R_{L_O} and PTE. It is demonstrated that increasing the P_{scf} raises the ACC's geometrical size; however, having physically larger Tx/Rx coils does not ensure higher PTE levels. Increasing strong coupling factor also raises the RIPT system's R_{L_O} value and the

maximum achievable PTE at R_{L_O} (i.e.: η_{max}.). With respect to the strong coupling factor's impact on the coil size, η and η_{max}, a recursive algorithm is introduced to assist in the selection of the most favourable value for the parameter P_{scf} and the subsequent coil geometry optimisation. Also, design examples of two nominal RIPT systems at resonant frequencies of $300\,\text{kHz}$ and $10\,\text{kHz}$ are used to theoretically investigate the design algorithm over the mid- and low-frequency bands, for which successful results were achieved.

The geometry design method was validated by developing four prototype Tx/Rx ACC pairs, operating over low- and mid-frequency bands (i.e.: $1.06\,\text{MHz}$, $100\,\text{kHz}$, $50\,\text{kHz}$ and $15\,\text{kHz}$.). Measurements presented from the Tx/Rx ACC pair in the RIPT link operating at $1.06\,\text{MHz}$ show a difference of around 7% between practical and calculated PTE values. For the ACC geometry which is designed to be employed in the RIPT link operating at $100\,\text{kHz}$, the calculated and practically measured PTE values show a difference of 6%. In the prototyped Tx/Rx ACC geometry which is designed for the RIPT link operating at $50\,\text{kHz}$, the calculated and measured PTE values are within 14% of each other. Also, the Tx/Rx ACC pair designed for the RIPT link operating at $15\,\text{kHz}$ show a difference close to 12% between practical PTE measurements and the calculated values. The correlation between the measured and calculated PTE values of all four prototyped RIPT systems validate the presented design process over the low- and mid-frequency bands.

CHAPTER 5

OPTIMISING FERRITE-CORED COIL GEOMETRY

To design an optimum Tx/Rx coil geometry (i.e.: air-cored coil.) which provides maximum PTE in the RIPT systems, a novel recursive algorithm is presented in chapter 4. Adding a ferrite core to the designed air-cored coil, in addition to enabling further enhancement of PTE, can also result in a miniaturised Tx/Rx coil geometry. This chapter presents an advanced iterative algorithm based on the earlier air-cored algorithm to design an optimum ferrite-cored coil geometry that can maximise the PTE of the RIPT system.

5.1 Introduction

Ferrite materials have been widely employed in RIPT systems to boost the system's PTE [18, 21, 27, 44, 47–54]. Ferrites are a sub-group of ferrimagnetic materials which feature high relative magnetic permeability [21, 117, 130]. Considering this, inserting ferrite cores into the Tx/Rx coil increases coil self-inductance which, in turn, improves the inductive linkage between the Tx and Rx [52]. A ferrite-cored coil (FCC), in comparison with a similar size air-cored coil (ACC), provides a higher self-inductance. Hence, ferrite cores are utilised to reduce the physical size of Tx/Rx coils in RIPT systems, as well [44]. This feature is highly beneficial for RIPT applications operating at low- and mid-frequency bands, where physically large Tx/Rx coils are frequently required to provide high PTE levels [50].

When a ferrite core is inserted into a wire-wound coil (i.e.: air-cored coil.), ferrite will be strongly magnetised in the presence of the winding's magnetic field. The ferrite magnetisation, which is caused by the magnetic field's induction inside the core, intensifies the coil inductance [27, 55–58]. However, the induced field, based on the Lenz's law of induction, will oppose the incident magnetic field thus reduces the magnetisation level inside the ferrite core [27, 50, 55, 58, 59]. This effect is called demagnetisation or negative

magnetisation [130]. The effectiveness of magnetisation in a material, with respect to the air, is measured by the parameter relative magnetic permeability (μ_r). In ferrite materials, the relative magnetic permeability is a complex quantity which, based on [44, 58], can be expressed as:

$$\mu_r = \mu_r' - j\mu_r''.$$

(5.1)

In (5.1), μ_r' and μ_r'' are the real and imaginary components of the complex relative permeability, respectively. The real component μ_r' accounts for the ferrite's magnetisation ability which can enhance the magnetic flux. The imaginary component μ_r'' represents demagnetisation in the ferrite (i.e.: magnetic field loss.).

In a resonant IPT system, introducing ferrite cores to the Tx/Rx coil pair, by amplifying the coil inductance, can enhance the inductive link's PTE. Concurrent with this, the ferrite's demagnetisation will yield magnetic field loss inside the core, which reduces the RIPT system's overall PTE. Thus, in a RIPT system the challenge in adopting ferrite-cored Tx/Rx coils is to design an optimum geometry that can provide maximised PTE. A better understating of the effect of adding ferrite core on the power transfer link demands the analytical model of Tx/Rx ferrite-cored coils, which is presented in the next section.

5.2   Analytical Model of Ferrite-cored Coils

The physical model for a ferrite-cored solenoid is shown in Fig. 5.1a, where a cylindrical ferrite rod with radius of r_f and length of l_f, is placed inside a wire-wound solenoid. The coil winding is identical to the air-cored solenoid modeled in section (3.1). Also, the core and winding are considered to have the same dimensions (i.e.: $r_f \approx r_c$ and $l_f = l_c$.). The equivalent circuit model for ferrite-cored coils has been widely considered as an inductor (L_{wf}) series with a parasitic resistance (R_{wf}), as shown in Fig. 5.1b [44, 53, 58]. It should be noted that, similar to the model of air-cored solenoid (i.e.: shown in Fig. 3.2b), the parasitic capacitance of the ferrite-cored coil has been neglected in Fig. 5.1b. Models for
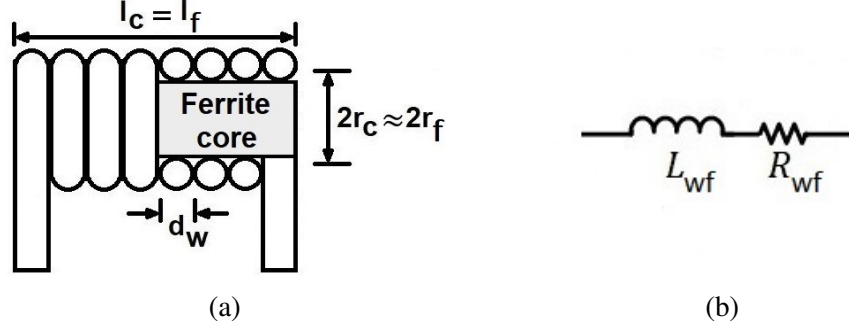
Figure 5.1: Model of a ferrite-cored solenoid: (a) physical structure, (b) equivalent circuit.

calculation of self-inductance and parasitic resistance in ferrite-cored solenoids, as shown in Fig. 5.1, are well established in the literature [44, 53, 58, 59]. In this section the models of L_{wf} and R_{wf} have been adopted from various references and will be utilised to calculate the FCC's inductance and parasitic resistance in the rest of this chapter.

For a ferrite-cored solenoid the self-inductance, according to [44, 53, 58, 59], can be expressed as:

$$L_{\mathrm{wf}} = \mu'_r L \qquad (5.2)$$

in which L is the self-inductance of air-cored solenoid (i.e.: equation (3.1).). With substituting L from (3.1), L_{wf} can be restated as:

$$L_{\mathrm{wf}} = \frac{\mu'_r \mu_o \pi N^2 r_c^2}{\sqrt{4r_c^2 + l_c^2}} . \qquad (5.3)$$

The parasitic resistance of a ferrite-core coil consists of losses in the core (R_{f}) and winding (i.e.: R_c in equation (3.2).):

$$R_{\mathrm{wf}} = R_{\mathrm{f}} + R_c . \qquad (5.4)$$

Considering the demagnetisation effect in ferrite the core's magnetic loss, according to [44, 58, 59], can be expressed as:

$$R_{\mathrm{f}} = \omega_o \mu''_r L \qquad (5.5)$$

81

where with replacing L from (3.2), R_f can be restated as:

$$R_\mathrm{f} = \frac{\omega_o \mu_r'' \mu_o \pi N^2 r_c^2}{\sqrt{4r_c^2 + l_c^2}}\,.\tag{5.6}$$

The parasitic resistance of FCCs, with substituting R_f and R_c from (5.6) and (3.2) respectively, can be expressed as:

$$R_\mathrm{wf} = \frac{\omega_o \mu_r'' \mu_o \pi N^2 r_c^2}{\sqrt{4r_c^2 + l_c^2}} + N r_c \eth\,.\tag{5.7}$$

From (5.2) and (5.5) it is deduced that in a ferrite-cored coil the inductance and parasitic resistance are highly influenced by the winding's L and R_c.

5.3 Optimum Geometry of Ferrite-cored Coils for Maximised PTE

Considering the dependency of L_wf and R_wf on the winding's geometry (i.e.: ACC's L and R.), finding an optimal geometry for the ferrite-cored coil which can maximise PTE necessitates designing the optimum geometry for the winding (i.e.: air-cored coil.). The FoM parameter and iterative algorithm to design the winding's optimum geometry has been expressed in chapter 4. However, the method presented to find the optimum ACC geometry does not determine if the designed winding maximises PTE at the presence of ferrite cores as well. To investigate this requirement further, the air-cored solenoid designed in section (4.3.1) is considered, where $r_c = 9.50\,\mathrm{mm}$, $N = 24$ and $l_c = 19.00\,\mathrm{mm}$. The coil inductance and parasitic resistance of the designed winding, based on Table 4.6, is $L = 7.51\,\mu\mathrm{H}$ and $R = 0.15\,\Omega$ respectively. Also, the designed air-cored solenoid provides a maximum PTE of 87.24%. Adding a core, made from a typical ferrite material (i.e.: material 67 from Fair-Rite Products Crop [131].) with $\mu_r' = 2$ and $\mu_r'' = 0.15$, to the winding leads the coil inductance and parasitic resistance increasing to $L_\mathrm{wf} = 15.07\,\mu\mathrm{H}$ and $R_\mathrm{wf} = 7.68\,\Omega$ respectively. However, for the developed RIPT system with employed ferrite cores, PTE reduces to 24.92%. The RIPT system's additional design specifications for the air-cored

Table 5.1: Specifications of the air-cored and ferrite-cored coils ($r_c = 9.50\,\text{mm}$, $N = 24$, $l_c = 19.00\,\text{mm}$ at $f_o = 1.06\,\text{MHz}$).

	L	R	R_{L_O}	α	β	η for	η for
	(μH)	(Ω)	(Ω)	(Ω)	(Ω)	R_{L_O}(%)	R_L (%)
Air-cored coil	7.51	0.152	2.38	1.15	4.90	87.98	87.24
	L_{wf}	R_{wf}	$R_{L_{O_{\text{wf}}}}$	α_{wf}	β_{wf}	η_{wf} for	η_{wf} for
	(μH)	(Ω)	(Ω)	(Ω)	(Ω)	$R_{L_{O_{\text{wf}}}}$(%)	R_L (%)
Ferrite-cored coil	15.07	7.68	19.85	13.44	29.30	44.20	24.92

coil (i.e.: R_{L_O}, α, β and η for R_{L_O}.) and the ferrite-cored coil (i.e.: $R_{L_{O_{\text{wf}}}}$, α_{wf}, β_{wf} and η_{wf} for $R_{L_{O_{\text{wf}}}}$.) have been provided in Table 5.1. In the table, the parameter η_{wf} represents the RIPT system's power transfer efficiency when ferrite-cored Tx/Rx coil pair are employed. The optimum load value for the system with ferrite-cored coils is noted by $R_{L_{O_{\text{wf}}}}$. Also, the parameters α_{wf} and β_{wf} are higher and lower boundary ranges around maximum PTE for the RIPT system with ferrite-cored Tx/Rx coils, respectively. The parameters η_{wf}, $R_{L_{O_{\text{wf}}}}$, α_{wf} and β_{wf} can be calculated from equations (B. 1), (B. 2), (B. 6) and (B. 7) in Appendix B, respectively.

From Table 5.1 it can be deduced that although the designed ACC geometry maximises the system's PTE, adding a ferrite core does not necessarily yield a higher PTE level. Hence, to design an optimum FCC geometry it is required to firstly verify if adding the ferrite core to the Tx/Rx coil pair will increase PTE. This is especially important because employing bulky (i.e.: physically large.) ferrite-cored coils will significantly increase the RIPT application's overall cost, in addition to making the system unnecessarily heavy [47]. Considering this requirement much work has been devoted to design an optimum geometry for the Tx/Rx ferrite-cored coils in the RIPT systems [21, 27, 44, 47, 50–54]. A commonly employed technique, for finding the optimum FCC geometry [21, 27, 47, 50–53], is to initially design the optimum ACC geometry which fulfils the RIPT application require-

ments. Having designed the optimum winding geometry the ferrite core will be added to the Tx/Rx coil pair. The next step is then to adjust the FCC geometry to achieve the desired PTE level. Following this approach to provide an optimum geometry which maximises PTE in the RIPT systems with Tx/Rx ferrite-cored solenoid pair, an advanced iterative algorithm will be presented in the next section. The advanced FCC design algorithm is developed by adding additional constraints (i.e.: μ_r' and μ_r''.) and conditions to the novel iterative algorithm, presented in Fig. 4.4, with respect to the ferrite's magnetisation and demagnetisation effects.

5.4 Geometry Design Procedure for the Ferrite-cored Coil

To design an optimum geometry for the ferrite-cored coil which maximises PTE for the required RIPT application an advanced iterative algorithm, based on the method developed in chapter 4, is depicted in Fig. 5.2. The demonstrated design procedure, through selecting a proper P_{scf} value will provide an optimum coil geometry which maximises PTE for the required RIPT application.

The FCC's design algorithm, as shown in Fig. 5.2, starts with taking a set of design constraints and an initial value for the FoM parameter. The design constraints comprise R_s, R_L, f_o, d_w, K, μ_r', μ_r'', the parameter X and the spatial limitations (i.e.: maximum/minimum r_c and/or maximum/minimum l_c.) which can be determined from the RIPT application and requirements. Also, the information on the ferrite material's μ_r' and μ_r'' is generally supplied by the manufacturer of the material. Similar to ACC's design algorithm, the parameter P_{scf} can initially take any arbitrary value, because the optimisation algorithm provides the designer with a good sense of how to make necessary changes to the P_{scf} value to maximise PTE.

With selecting the initial value for the P_{scf}, geometrical parameters of the Tx/Rx ACC pair (i.e.: L, R, r_c, l_c and N.) can be calculated from equations (3.1), (3.36), (3.32) and (3.2). It should be noted that the parameter $\eth$ in (3.2), depending on the RIPT system's
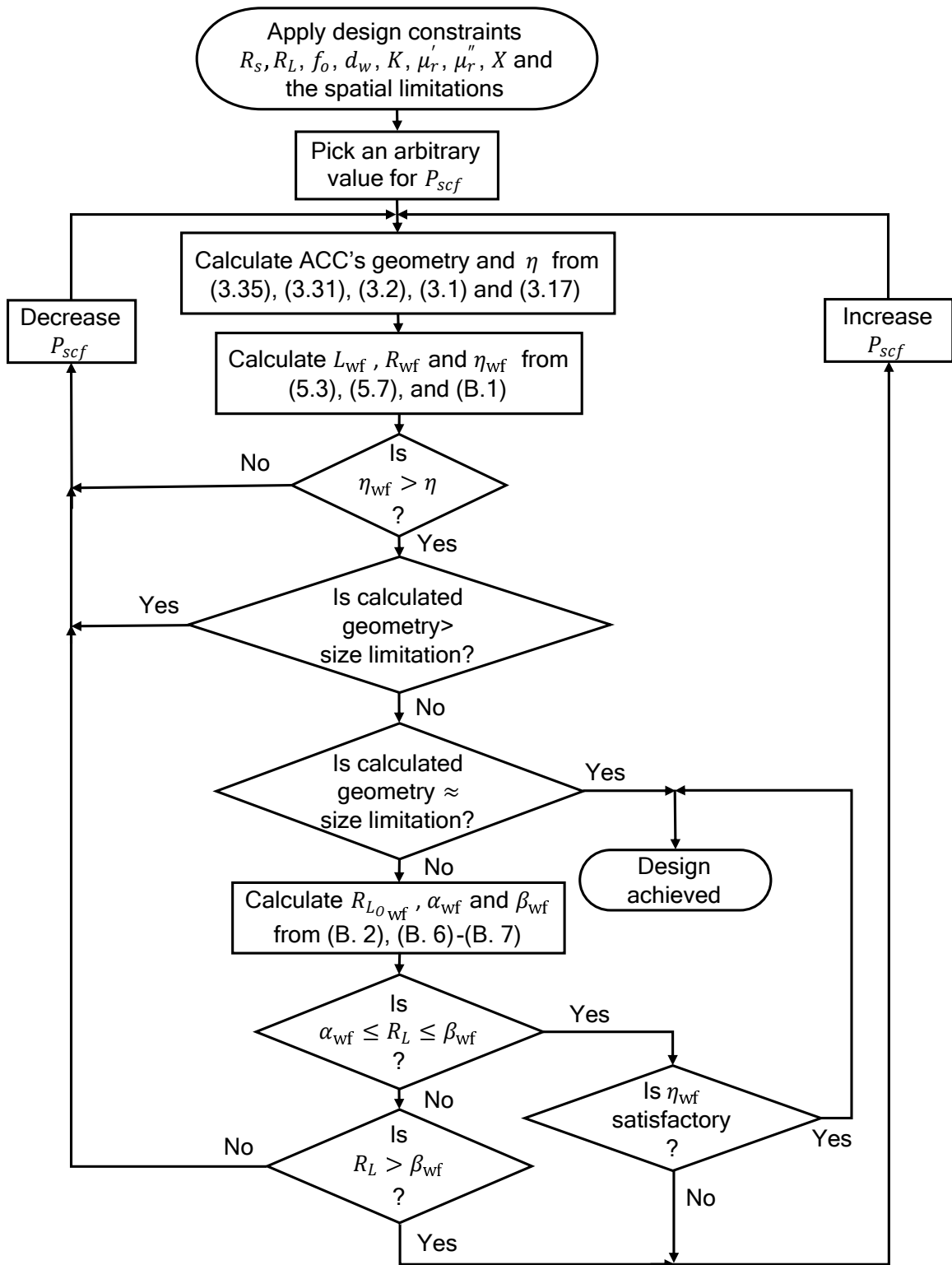
Figure 5.2: Flowchart of design algorithm for ferrite-cored coils.

operating frequency (i.e.: f_o.), can be determined either from (3.6) or (3.7). After calculating the ACC's geometrical parameters for the initial P_{scf} value, PTE of the RIPT system can be calculated for the developed air-cored winding, from (3.17). In the next step, the developed geometrical parameters will be employed to calculate L_{wf}, R_{wf} and η_{wf} from (5.3), (5.7) and (B.1) respectively. After calculating PTEs for the RIPT application with ACC and FCC pair, the values of η and η_{wf} will be compared together to ensure adding the ferrite core can benefit the RIPT system. In case adding ferrite core can enhance the system's PTE, the P_{scf} value will be modified in an iterative manner such that the final designed geometry maximises the RIPT system's PTE, besides meeting the application's spatial requirements.

To numerically describe the design algorithm, a mid-frequency RIPT system similar to the exemplified application discussed in section (4.2) (i.e.: Table 4.3.) has been considered where $R_s = 5.77\,\Omega$ and $R_L = 10\,\Omega$ at $f_o = 300\,\mathrm{kHz}$ [79]. The coil winding conductor used is $0.511\,\mathrm{mm}$ (diameter) copper wire, and the inductive link's coupling coefficient, K, is 0.2. It has been considered that the Tx/Rx coil diameter must be less than $32\,\mathrm{mm}$ (i.e.: $r_c \leq 16\,\mathrm{mm}$.). To ensure the designed coil geometry exhibits a high PTE the chosen proximity range of $\eta_{max_{\mathrm{wf}}}$ is 10% (i.e.: $X = 10\%$.). It should be noted that $\eta_{max_{\mathrm{wf}}}$ is the RIPT system's PTE when the load is equal to $R_{L_{O_{\mathrm{wf}}}}$. For the given RIPT application, the core is considered to be made with the material 78 from Fair-Rite Products Crop (i.e.: the supplier of the ferrite rods used in this thesis.), where $\mu_r' = 3$ and $\mu_r'' = 0.1$ [131]. Table 5.2 shows some iteration examples for finding the FoM's optimal value which can maximise PTE for the RIPT application with a Tx/Rx FCC pair. The iterative design process is initiated with considering $P_{scf} = 1000$. It should be noted that to calculate R, equation (3.6) (i.e.: $\eth = \dfrac{\sqrt{2\omega_o \mu \rho}}{d_w}$.) is used. This is because the application's operating frequency is greater than $66.89\,\mathrm{kHz}$ (i.e.: $f_o > \dfrac{4\rho}{\pi \mu d_w^2}$.).

As can be seen in Table 5.2, adding a ferrite core to the calculated ACC geometry in the first iteration cannot fulfil the design algorithm's PTE requirement (i.e.: having $\eta_{\mathrm{wf}} > \eta$.).

Table 5.2: Algorithm iterations to design an optimum FCC pair for the RIPT system under consideration ($f_o = 300\,\text{kHz}$, $R_s = 5.77\,\Omega$ and $R_L = 10\,\Omega$).

State #	P_{scf}	R (Ω)	r_c (mm)	N	l_c (mm)	η for R_L(%)	η_{wf} for R_L(%)	$R_{L_{O_{\text{wf}}}}$ (Ω)	α_{wf} (Ω)	β_{wf} (Ω)	η_{wf} for $R_{L_{O_{\text{wf}}}}$(%)
1	1000	0.77	18.70	73	37.40	90.59	25.56	-	-	-	-
2	400	0.56	16.00	63	32.00	89.15	34.96	-	-	-	-
3	100	0.34	12.50	49	25.00	77.34	49.10	-	-	-	-
4	10	0.16	8.50	33	17.00	28.13	53.30	8.62	0.412	14.01	53.51
5	34	0.24	10.50	41	21.00	56.29	55.88	-	-	-	-
6	33	0.23	10.40	40	20.80	55.59	55.97	18.77	0.814	35.29	59.66

Also, the calculated coil geometry does not meet the RIPT system's spatial requirement (i.e.: having $r_c \leq 16\,\text{mm}$.). Considering that the first and second decision boxes in the design flowchart are not met in this state, the values for the parameters $R_{L_{O_{\text{wf}}}}$, α_{wf}, β_{wf} and η_{wf} for $R_{L_{O_{\text{wf}}}}$ do not need to be calculated (blank spaces in state 1, Table 5.2). Following the design algorithm, in state 2 the FoM parameter has been reduced to 400. The calculated FCC geometry for $P_{scf} = 400$ also does not fulfil the condition $\eta_{\text{wf}} > \eta$, although the coil dimensions meet the application's spatial requirement. Again, the values for the parameters $R_{L_{O_{\text{wf}}}}$, α_{wf}, β_{wf} and η_{wf} for $R_{L_{O_{\text{wf}}}}$ do not need to be calculated (blank spaces in state 2, Table 5.2). In order to search for a coil geometry which meets the PTE condition, the FoM parameter has been further reduced in iterations 3 and 4. The selected FoM value in state 4 (i.e.: $P_{scf} = 10$.) enables designing a coil geometry that meets the condition $\eta_{\text{wf}} > \eta$ and the application's spatial requirement. To further improve η_{wf} level in state 4, the P_{scf} value has been slightly modified in iterations 5 and 6. The maximum strong coupling factor value that can meet both the algorithm (i.e.: $\eta_{\text{wf}} > \eta$.) and application (i.e.: $r_c \leq 16\,\text{mm}$.) requirements is $P_{scf} = 33$. For this FoM value, the designed coil geometry is $r_c = 10.40\,\text{mm}$, $N = 40$ and $l_c = 20.80\,\text{mm}$ and the maximum PTE of 55.97% is theoretically achieved. It should be noted that again in states 3 and 5, the values for the parameters $R_{L_{O_{\text{wf}}}}$, α_{wf}, β_{wf} and η_{wf} for $R_{L_{O_{\text{wf}}}}$ do not need to be calculated (blank spaces

Table 5.3: Algorithm iterations to design an optimum FCC pair for the RIPT system under consideration ($f_o = 10\,\text{kHz}$, $R_s = 0.01\,\Omega$ and $R_L = 1\,\text{k}\Omega$).

State #	P_{scf}	R (Ω)	r_c (mm)	N	l_c (mm)	η for R_L(%)	η_{wf} for R_L(%)	$R_{L_{O_{\text{wf}}}}$ (Ω)	α_{wf} (Ω)	β_{wf} (Ω)	η_{wf} for $R_{L_{O_{\text{wf}}}}$(%)
1	15	2.83	72.30	180	144.60	92.13	90.70	-	-	-	-
2	1	0.73	36.80	92	73.60	44.72	60.70	73.70	5.54	967.96	91.02
3	3	1.27	48.40	121	96.80	70.76	78.22	-	-	-	-
4	2	1.04	43.70	109	87.40	61.77	72.58	-	-	-	-
5	2.49	1.16	46.20	115	92.40	66.78	75.76	-	-	-	-
6	1.4	0.87	40.00	100	80.00	53.09	66.78	94.74	6.63	1337.91	91.17

in states 3 and 5, Table 5.2).

As the second example to numerically explore the FCC geometry design procedure, a low-frequency RIPT system with $R_s = 0.01\,\Omega$, $R_L = 1\,\text{k}\Omega$ at $f_o = 10\,\text{kHz}$ has been considered, where the length of Tx/Rx FCC must be less than $80\,\text{mm}$ (i.e.: $l_c \leq 80\,\text{mm}$.). This RIPT system has application in inductive power transfer to industrial monorail pickup tracks and factory automation [38]. The coil winding conductor used is $0.8\,\text{mm}$ (diameter) copper wire, and the inductive link's coupling coefficient, K, is 0.9. To ensure the designed coil geometry exhibits a high PTE the chosen proximity range of $\eta_{max_{\text{wf}}}$ is 10% (i.e.: $X = 10\%$.). For the given RIPT application, the core is considered to be made with the material 78 from Fair-Rite Products Crop, where $\mu'_r = 3$ and $\mu''_r = 0.1$ [131]. Table 5.3 shows some iteration examples for finding the FoM's optimal value which can maximise PTE for the RIPT application with a FCC Tx/Rx coil pair (rational for blank spaces are covered in Table 5.2). The iterative design process is initiated with considering $P_{scf} = 15$. It should be noted that to calculate R, equation (3.7) (i.e.: $\eth = \dfrac{384\rho + \omega_o\mu d_w^2}{48d_w^2}$.) is used. This is because the application's operating frequency is less than $27.29\,\text{kHz}$ (i.e.: $f_o \leq \dfrac{4\rho}{\pi\mu d_w^2}$.).

Based on the iteration examples listed in Table 5.3, adding a ferrite core to the calculated coil geometry in the first iteration cannot fulfill the condition $\eta_{\text{wf}} > \eta$. Also, the calculated

geometry does not meet the resonant IPT system's spatial requirement (i.e.: having $l_c \leq$ 80 mm.). Hence, the P_{scf} has been reduced to 1 in the second iteration. The selected FoM value in state 2 (i.e.: $P_{scf} = 1$.) enables designing a coil geometry that meets the condition $\eta_{wf} > \eta$ and the RIPT application's spatial requirement. To further improve the PTE level in state 2, the P_{scf} value has been slightly increased/decreased in iterations 3 to 6. The strong coupling factor value that can meet both the algorithm (i.e.: $\eta_{wf} > \eta$.) and application (i.e.: $l_c \leq 80$ mm.) requirements is $P_{scf} = 1.4$. For this FoM value, the designed coil geometry is $r_c = 40.00$ mm, $N = 100$ and $l_c = 80.00$ mm and the maximum PTE of $\eta_{wf} = 66.78\%$ is theoretically achieved.

It should be noted that winding geometry of the designed FCC pair (i.e.: state 6 in Table 5.3.) is in fact the optimum ACC pair which was designed, for the same RIPT application, in Table 4.4. Also, it is worth mentioning that the value of η in the state 5 is equal to the value of η_{wf} in the state 6 (i.e.: 66.78%.). Comparing the coil geometries in these two states it can be deduced that the optimum FCC pair can provide the same PTE level that a much larger ACC pair can provide. The coil geometry in the state 6 is $r_c = 40.00$ mm, $N = 100$ and $l_c = 80.00$ mm. The coil geometry in the state 5 is $r_c = 46.20$ mm, $N = 115$ and $l_c = 92.40$ mm. This comparison highlights that employing an optimum FCC pair in a RIPT system can miniaturise the Tx/Rx coil geometry, in addition to enhancing the system's PTE.

5.5 Experimental Results & Validation of FCC Design Process

In this section, the advanced FCC geometry design methodology, described in Fig. 5.2, is empirically validated over low- and mid-frequency bands. To facilitate practical, bench-top, investigations two typical RIPT systems have been considered with resonance frequencies at: *I)* 50 kHz (i.e.: mid-frequency [119, 120].) and *II)* 15 kHz (i.e.: low-frequency [119, 120].).

5.5.1 Design Example of FCC Pair Operating at $50\,\text{kHz}$

As an example to practically validate the FCC design technique over the mid-frequency band, an arbitrary chosen resonant inductive power transfer system with $R_s = 3\,\Omega$, $R_L = 1.5\,\Omega$ at $f_o = 50$ kHz has been considered, where the length of Tx/Rx FCC pair must be less than 25 mm (i.e.: $l_c \leq 25$ mm.). The Tx/Rx coupling coefficient, K, is 0.207 and the chosen proximity range of $\eta_{max_{\text{wf}}}$ is 3% (i.e.: $X = 3\%$.). The considered RIPT system has energy transfer applications in electric vehicles [52]. For the given RIPT application, the core is considered to be made with the material 78 from Fair-Rite Products Crop, where $\mu'_r = 3$ and $\mu''_r = 0.1$ [131]. The ferrite material 78 is selected with considering the ferrite bar's availability, the cost associated with it and its operating frequency range. Based on the manufacturer's technical information, the material 78 is the most feasible material developed to facilitate the RIPT applications operating at the required frequency range [131]. The coil winding conductor used is $0.8\,\text{mm}$ (diameter) copper wire. The $0.8\,\text{mm}$ wire is selected as a suitable diameter value to give a reasonable ohmic resistance and allow ease of practical construction of the coils in the rest of this chapter. Also, it should be noted that to calculate R, equation (3.6) (i.e.: $\eth = \dfrac{\sqrt{2\omega_o\mu\rho}}{d_w}$.) is used. This is because the application's operating frequency is greater than $27.29\,\text{kHz}$ (i.e.: $f_o > \dfrac{4\rho}{\pi\mu d_w^2}$.).

Some iteration examples to find the optimal P_{scf} value for the considered RIPT system are listed in Table 5.4. Following the design procedure (i.e.: the iterative algorithm shown in Fig. 5.2.), the optimal FoM value for the given resonant IPT system is $P_{scf} = 6$ (i.e.: state 5 in Table 5.4.). Selecting this FoM value results in designing a Tx/Rx ferrite-cored coil pair with $r_c = 12.50$ mm, $N = 31$ and $l_c = 25.00$ mm which can provide maximum PTE of 42.66%. Further specifications of the designed geometry including Tx and Rx FCC's self-inductances (i.e.: $L_{p_{\text{wf}}}$ and $L_{s_{\text{wf}}}$ respectively.), parasitic resistances (i.e.: $R_{p_{\text{wf}}}$ and $R_{s_{\text{wf}}}$ respectively.) and intrinsic quality factors (i.e.: $Q_{i_{p_{\text{wf}}}}$ and $Q_{i_{s_{\text{wf}}}}$ respectively.) are mentioned in Table 5.5. It should be noted that for a ferrite-cored coil the $Q_{i_{\text{wf}}}$ can be

Table 5.4: Algorithm iterations to design an optimum FCC pair for the RIPT system under consideration ($f_o = 50\,\text{kHz}$, $R_s = 3\,\Omega$ and $R_L = 1.5\,\Omega$).

State #	P_{scf}	R (Ω)	r_c (mm)	N	l_c (mm)	η for R_L(%)	η_{wf} for R_L(%)	$R_{L_{O_{\text{wf}}}}$ (Ω)	α_{wf} (Ω)	β_{wf} (Ω)	η_{wf} for $R_{L_{O_{\text{wf}}}}$(%)
1	100	0.15	20.30	51	40.60	73.72	34.50	-	-	-	-
2	25	0.09	15.90	40	31.80	48.73	44.80	-	-	-	-
3	2.5	0.04	10.80	27	21.60	9.41	33.02	0.81	0.56	1.18	35.79
4	4	0.05	11.70	29	23.40	14.17	38.81	1.12	0.77	1.63	35.53
5	6	0.06	12.50	31	25.00	19.72	42.66	1.47	1	2.16	42.66

calculated by substituting L and R with L_{wf} and R_{wf} respectively in (3.21), as:

$$Q_{i_{\text{wf}}} = \frac{\omega_o L_{\text{wf}}}{R_{\text{wf}}} .$$

To practically investigate the achievable PTE of the designed geometry, a Tx/Rx FCC pair for $P_{scf} = 6$ was physically constructed. It is worth mentioning that a solid ferrite rod that can occupy the entire space inside the designed windings was not already fabricated by the available ferrite manufacturers. Hence, following a common technique, the windings are filled with numbers of cylindrical ferrites with the identical length of l_c, as shown in Fig. 5.3 [44, 50, 132]. This approach results in a laminated core, which leads to a reduction in the Tx/Rx FCC's parasitic resistances (i.e.: $R_{p_{\text{wf}}}$ and $R_{s_{\text{wf}}}$.) [50, 51]. The measured L_{wf}, R_{wf} and $Q_{i_{\text{wf}}}$ values of the prototyped ferrite-cored solenoid pair are listed in Table 5.5. The measurements are taken using an electronic LCR meter (Rohde & Schwarz HM8118). The differences between the calculated and measured values of the Tx/Rx FCC's parasitic resistances in Table 5.5 are attributed to employing the laminated ferrite cores, which result in a reduced R_{wf} value [50, 51].

Similar to the technique employed in chapter 4, the PTE measurements have been carried out on a series-series RIPT system, as shown in Fig. 4.5a, where compensation capacitors (i.e.: C_p and C_s.), source and load resistors (i.e.: R_s and R_L respectively.) are directly

Figure 5.3: Physical structure of the employed ferrite-cored coils.

added to the primary and secondary ferrite-cored coils. For the RIPT system demonstrated in Fig. 4.5a, the utilised experimental set up is shown in Fig. 5.4, where a function generator (Hewlett Packard 33120A) is used to drive the primary coil at the resonance frequency (i.e.: $50\,\text{kHz}$.). In order to probe the system's energy transmission efficiency, an oscilloscope (Rigol DS1054Z) is used to measure the voltage and current waveforms at the Tx/Rx side. The transmitted power is found by multiplying the RMS values of the measured voltage and current signals injected into the primary circuitry [30, 79]. The received power is also calculated by measuring the voltage across the load [30, 79].

For the designed FCC geometry, the maximum achievable PTE (i.e.: $\eta_{max_{\text{wf}}}$.) is 42.66% at $R_{L_{O_{\text{wf}}}} = 1.47\,\Omega$. Based on the physical circuit parameters developed in Table 5.4, for all load values between α_{wf} and β_{wf} (i.e.: $1\,\Omega \leq R_L \leq 2.16\,\Omega$.) the system's PTE will be within 3% of $\eta_{max_{\text{wf}}}$ (i.e.: $\geq 41.38\%$.). Fig. 5.5 shows the calculated PTE against

Table 5.5: Specifications of the prototyped FCC geometry ($r_c = 12.50\,\text{mm}$, $N = 31$, $l_c = 25.00\,\text{mm}$ at $f_o = 50\,\text{kHz}$).

	$L_{p_{\text{wf}}}$ (μH)	$R_{p_{\text{wf}}}$ (mΩ)	$Q_{i_{p_{\text{wf}}}}$	$L_{s_{\text{wf}}}$ (μH)	$R_{s_{\text{wf}}}$ (mΩ)	$Q_{i_{s_{\text{wf}}}}$
Calculated value	51.03	598.28	27.11	51.03	598.28	27.11
Measured value	48.81	427.04	35.36	49.72	461.27	33.87
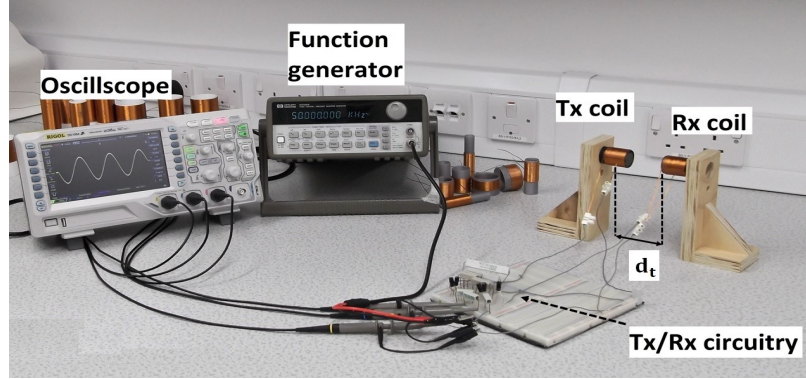
Figure 5.4: Experimental PTE test setup for the RIPT system with Tx/Rx ferrite-cored coils (length of coil $= 25.00\,\text{mm}$, radius of coil $= 12.50\,\text{mm}$ and width apart, d_t, is varied).

increasing R_L for the FCC design; set beside this curve are the results taken from practical measurements as R_L is physically increased from $0.3\,\Omega$ to $15\,\Omega$. The measured values show that for all the load resistances within the α_{wf} and β_{wf} range, the system's PTE is higher than 42.98% (i.e.: within 0.75% of $\eta_{max_{\text{wf}}}$.). The measured results from the physical system show remarkable correlation with the calculated results. The calculated and measured PTE for the RIPT application (i.e.: $R_s = 3\,\Omega$ and $R_L = 1.5\,\Omega$.) are 42.66% and 45.16% respectively. The given RIPT system delivers $1.1\,\text{W}$ power to the load when $V_s = 2.12\,v_{rms}$.

Although the Tx/Rx FCC pair are designed for $K = 0.207$, the designed geometry maximises PTE over the range of $0 \leq K \leq 1$ as described in section (3.4.1). To practically
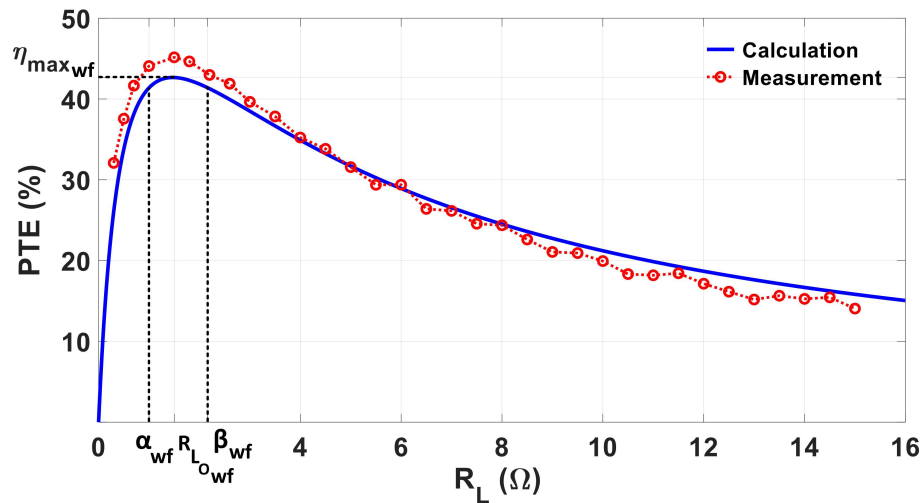
Figure 5.5: The calculated and measured PTE variations over a nominal range of load values. The $\eta_{max_{\text{wf}}}$, α_{wf} and β_{wf} values are indicated in Table 5.4 (state 5).
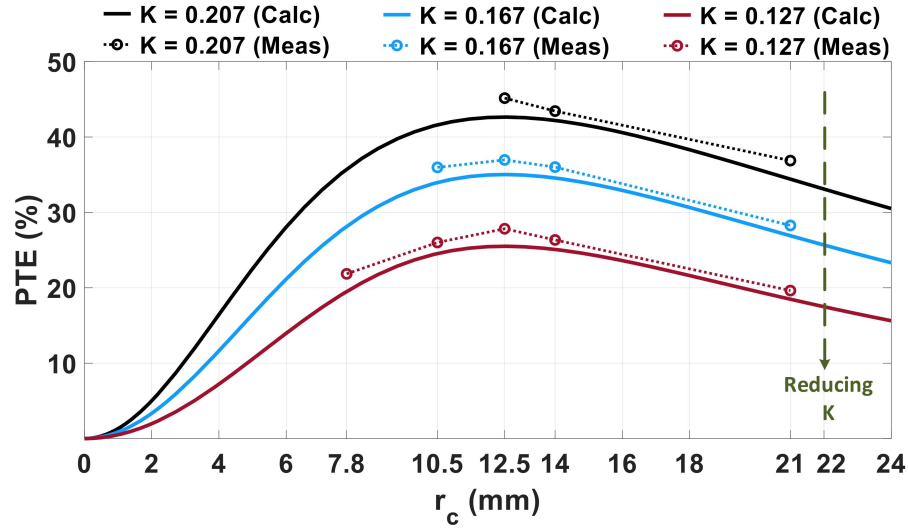
Figure 5.6: Calculated and measured PTE of five sets of coil over three K values from 0.207 to 0.127.

prove the concept, five sets of coil with laminated ferrite cores, each with different r_c values, have been constructed and their respective PTEs measured for the RIPT application. The three groups of different coloured solid and dashed curves plotted in Fig. 5.6 correspond to calculated and measured PTEs of the constructed FCC geometries for three K values between 0.127 to 0.207. The coupling coefficient range has been chosen to facilitate practical, bench-top, investigation and ease of results gathering. As can be seen in Fig. 5.6, with a fall in coupling coefficient, K, the link becomes more loosely-coupled but the maximum PTE becomes apparent as being around the designed ferrite-cored coil r_c value obtained from the advanced algorithm developed in this research work (i.e.: 12.50 mm.). The experimental PTE values show closeness to the analytical calculations using MATLAB. Practical tests on physical FCC geometries either side of $r_c = 12.50$ mm show falling PTE over different K values, thus validating the design method proposed.

Similar to the RIPT systems with air-cored coils, in a RIPT system with a Tx/Rx FCC pair the coupling coefficient, K, is also highly dependent on the relative distance between the Tx/Rx ferrite-cored solenoids. To verify the correct operation of the designed geometry with transmission distance, d_t, variations, calculated and measured PTE values over a d_t
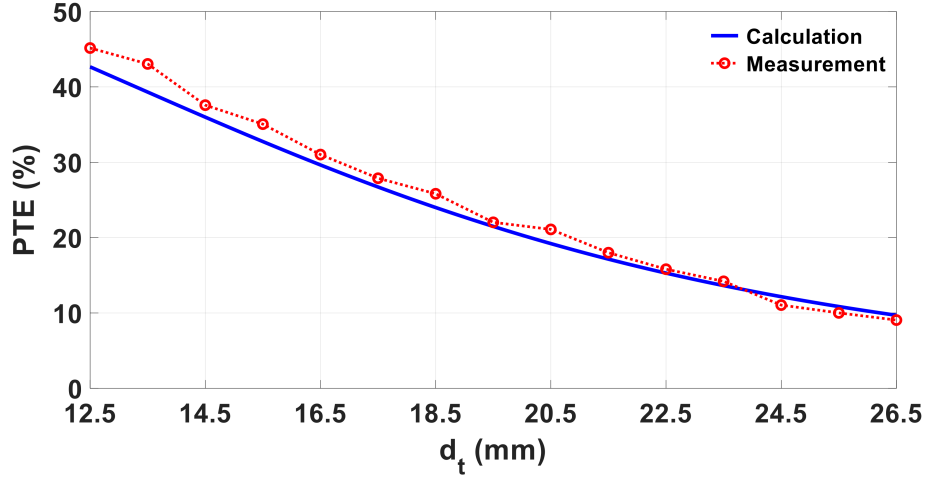
Figure 5.7: Comparison of PTE between practical measurements and theoretical results for the designed FCC pair over a d_t range from 12.5 mm to 26.5 mm.

range from 12.5 mm to 26.5 mm (i.e.: $0.0676 \leq K \leq 0.2072$.) have been compared in Fig. 5.7. From Fig. 5.7 it can be deduced that with an increase in transmission distance, the practically measured PTE values attenuate, as can be predicted from the theoretical equations.

With comparing the PTE measurements in Fig. 5.5, Fig. 5.6 and Fig. 5.7 a close correlation between the calculated values and measured results from the practical setup can be seen. It should be noted that, as listed in Table 5.5, the measured values of $R_{p_{\mathrm{wf}}}$ and $R_{s_{\mathrm{wf}}}$ are respectively $0.17 \, \Omega$ and $0.14 \, \Omega$ smaller than the calculated resistance values. This mismatch between the calculated and measured resistance values, which is due to employing the laminated ferrites cores, results in less power loss in the Tx/Rx FCC pair; hence, the PTE measurements on the constructed RIPT system can result in values higher than the calculations.

5.5.2 Design Example of FCC Pair Operating at 15 kHz

To practically validate the design technique over the low-frequency band, an arbitrary chosen resonant inductive power transfer system with $R_s = 3 \, \Omega$, $R_L = 3 \, \Omega$ at $f_o = 15$ kHz has been considered, where the length of Tx/Rx FCC pair must be less than 45 mm (i.e.:

95

Table 5.6: Algorithm iterations to design an optimum FCC pair for the RIPT system under consideration ($f_o = 15\,\text{kHz}$, $R_s = 3\,\Omega$ and $R_L = 3\,\Omega$).

State #	P_{scf}	R (Ω)	r_c (mm)	N	l_c (mm)	η for R_L(%)	η_{wf} for R_L(%)	$R_{L_{O_{\text{wf}}}}$ (Ω)	α_{wf} (Ω)	β_{wf} (Ω)	η_{wf} for $R_{L_{O_{\text{wf}}}}$(%)
1	100	0.69	35.50	89	71.10	65.08	36.61	-	-	-	-
2	50	0.53	31.20	78	62.40	56.65	42.84	-	-	-	-
3	10	0.30	23.30	58	46.70	26.00	46.68	-	-	-	-
4	5	0.23	20.60	52	41.40	15.47	41.41	2.33	1.59	3.43	41.95
5	8.2	0.28	22.50	56	45.00	22.62	45.62	3.26	2.20	4.82	45.68

$l_c \leq 45\,\text{mm}$.). The Tx/Rx coupling coefficient, K, is 0.2 and the chosen proximity range of $\eta_{max_{\text{wf}}}$ is 3% (i.e.: $X = 3\%$.). The considered RIPT system has applications in WPT to non-stationary electric buses [21]. For the given RIPT application, the core is considered to be made with the material 78 from Fair-Rite Products Crop, where $\mu'_r = 3$ and $\mu''_r = 0.1$ [131]. The coil winding conductor used is $0.8\,\text{mm}$ (diameter) copper wire. Also, it should be noted that to calculate R, equation (3.7) (i.e.: $\eth = \dfrac{384\rho + \omega_o \mu d_w^2}{48d_w^2}$.) is used. This is because the application's operating frequency is less than $27.29\,\text{kHz}$ (i.e.: $f_o \leq \dfrac{4\rho}{\pi \mu d_w^2}$.).

Some iteration examples to find the optimal FoM value for the given RIPT system are listed in Table 5.6. Following the design procedure, the optimal FoM value for the considered RIPT system is $P_{scf} = 8.2$ (i.e.: state 5 in Table 5.6.). Selecting this value results in designing a FCC pair with $r_c = 22.50\,\text{mm}$, $N = 56$ and $l_c = 45.00\,\text{mm}$ which

Table 5.7: Specifications of the prototyped FCC geometry ($r_c = 22.50\,\text{mm}$, $N = 56$, $l_c = 45.00\,\text{mm}$ at $f_o = 15\,\text{kHz}$).

	$L_{p_{\text{wf}}}$ (μH)	$R_{p_{\text{wf}}}$ (Ω)	$Q_{i_{p_{\text{wf}}}}$	$L_{s_{\text{wf}}}$ (μH)	$R_{s_{\text{wf}}}$ (Ω)	$Q_{i_{s_{\text{wf}}}}$
Calculated value	298.63	1.21	23.18	298.63	1.21	23.18
Measured value	283.34	0.845	31.41	289.86	0.891	30.63
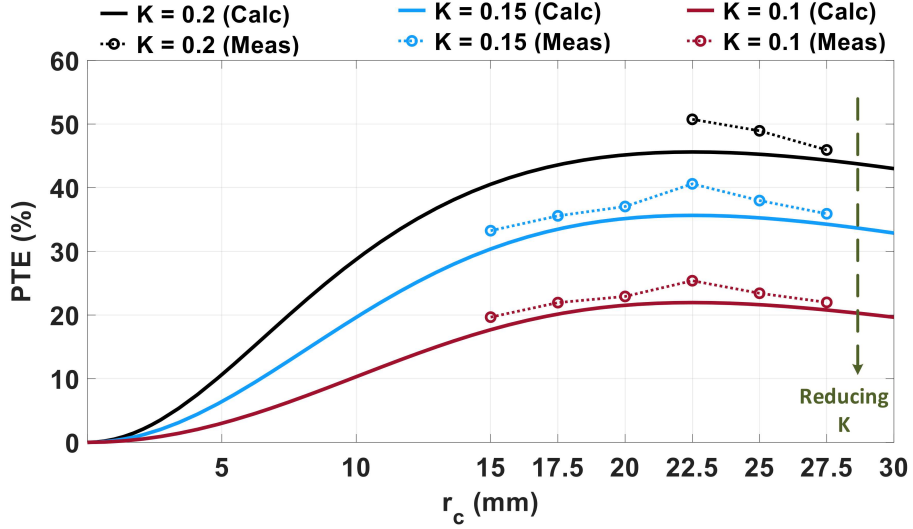
Figure 5.8: Calculated and measured PTE of six sets of coil over three K values from 0.2 to 0.1.

can provide maximum PTE of 45.62%. To practically investigate the achievable PTE of the designed geometry, a Tx/Rx solenoid pair with ferrite cores has been constructed for $P_{scf} = 8.2$. Following a common approach the Tx/Rx windings are filled with numbers of semi-length ferrite bars [44, 50, 132], as shown in Fig. 5.3. For the constructed Tx/Rx ferrite-cored solenoids the calculated and measured values of self-inductance, parasitic resistance and intrinsic quality factors are listed in Table 5.7.

The prototyped Tx/Rx FCC pair is designed to provide PTE of 45.62% when the coupling coefficient between the pair is $K = 0.2$. However, as described in section (3.4.1), the designed geometry maximises PTE over the range of $0 \leq K \leq 1$. To practically prove the concept, six sets of coil with laminated ferrite cores, each with different r_c values, have been constructed and their respective PTEs measured for the RIPT application. The calculated and measured PTEs of the constructed FCC geometries are plotted in Fig. 5.8. It should be noted that the PTE measurements have been carried out using the similar technique employed in section (5.5.1). In Fig. 5.8 three groups of different coloured solid and dashed curves correspond to calculated and measured PTEs for three K values between 0.1 to 0.2. The coupling coefficient range has been chosen again to facilitate practical, bench-

Figure 5.9: Comparison of PTE between practical measurements and theoretical results for the designed FCC pair over a d_t range from $22.5\,\text{mm}$ to $50.5\,\text{mm}$.
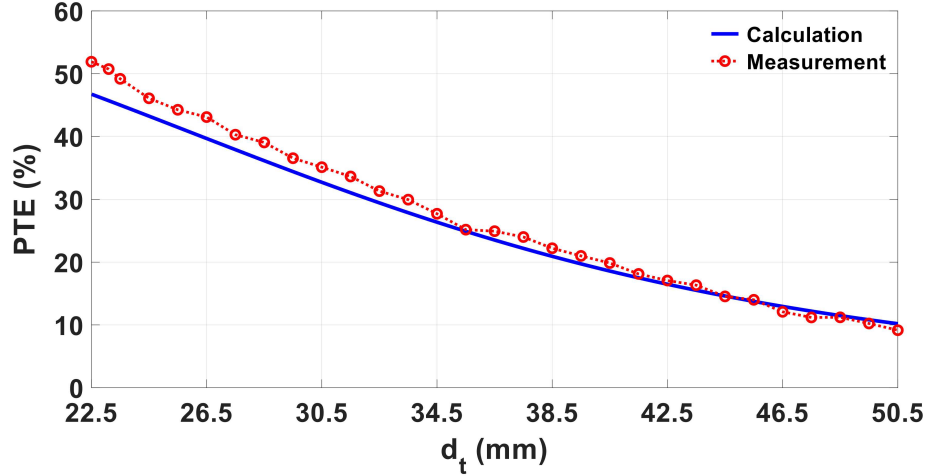
top, investigation and ease of results gathering. As can be seen in Fig. 5.8, with a fall in coupling coefficient, K, the link becomes more loosely-coupled but the maximum PTE becomes apparent as being around the designed ferrite-cored coil r_c value obtained from the novel algorithm developed in the research work (i.e.: $22.50\,\text{mm}$.). The experimental PTE value shows closeness to the analytical calculations using MATLAB. Practical tests on physical FCC geometries either side of $r_c = 22.50\,\text{mm}$ show falling PTE over different K values, thus validating the design method proposed.

It is worth mentioning that K is highly dependent on the relative distance between the Tx/Rx FCC pair. To evaluate the functionality of the designed geometry with variations of transmission distance, calculated and measured PTE values over a nominal d_t range from $22.5\,\text{mm}$ to $50.5\,\text{mm}$ (i.e.: $0.0612 \leq K \leq 0.2071$.) have been compared in Fig. 5.9. From Fig. 5.9 it can be deduced that with an increase in transmission distance, the practically measured PTE values attenuate, as can be predicted from the theoretical equations.

Furthermore, the maximum achievable PTE (i.e.: $\eta_{max_{\text{wf}}}$.) for the designed FCC geometry is 45.68% at $R_{L_{O_{\text{wf}}}} = 3.26\,\Omega$. Based on the physical circuit parameters developed in Table 5.6, for all load values between α_{wf} and β_{wf} (i.e.: $2.20\,\Omega \leq R_L \leq 4.82\,\Omega$.) the system's PTE will be within 3% of $\eta_{max_{\text{wf}}}$ (i.e.: $\geq 44.31\%$.). Fig. 5.10 shows the calcu-
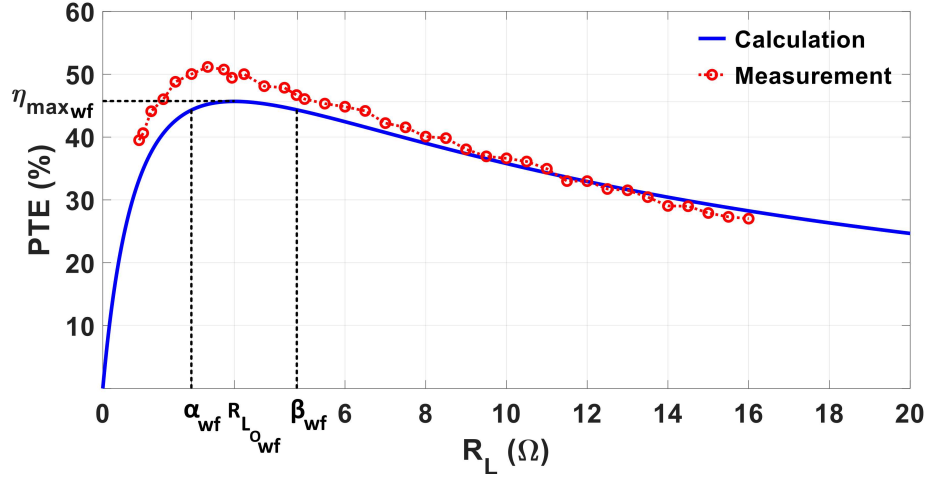
Figure 5.10: The calculated and measured PTE variations over a nominal range of load values. The $\eta_{max_{\text{wf}}}$, α_{wf} and β_{wf} values are indicated in Table 5.6 (state 5).

lated PTE against increasing R_L for the coil design; set beside this curve are the results taken from practical measurements as R_L is physically increased from $0.9\,\Omega$ to $16\,\Omega$. The measured values show that for all the load resistances within the α_{wf} and β_{wf} range, the system's PTE is higher than 46.68% (i.e.: within 2.19% of $\eta_{max_{\text{wf}}}$.). The measured results from the physical system show remarkable correlation with the calculated results. The calculated and measured PTE for the RIPT application (i.e.: $R_s = 3\,\Omega$ and $R_L = 3\,\Omega$.) are 45.62% and 50.74% respectively. The given RIPT system delivers $1.08\,\text{W}$ power to the load when $V_s = 2.47\,v_{rms}$.

With comparing the PTE measurements in Fig. 5.10, Fig. 5.8 and Fig. 5.9 a close correlation between the calculated values and measured results from the practical setup can be seen. It should be noted that employing laminated ferrite cores leads to constructing a FCC pair with parasitic resistances smaller than the calculated values thus providing higher PTE levels. As listed in Table 5.7, the measured values of $R_{p_{\text{wf}}}$ and $R_{s_{\text{wf}}}$ are respectively $0.36\,\Omega$ and $0.32\,\Omega$ smaller than the calculated resistance values. This difference in resistance values results in less power loss in the Tx/Rx FCC pair; hence, the PTE measurements on the physically constructed system can be higher than the calculated values.

5.5.3   Discussion

Comparing the experimental results in sections (5.5.1) and (5.5.2) shows that employing a FCC geometry designed using the advanced iterative algorithm presented in Fig. 5.2 maximises the RIPT system's overall PTE to the desired level. Also, it was shown that the designed FCC geometries demonstrate a consistent WPT performance over the low- and mid-frequency bands.

It is worth mentioning that manufacturing the FCC pair using ferrite cores that are customised for the designed geometry can reduce the slight mismatch between the calculated and measured PTE values.

5.6   Summary

In a RIPT system that operates in low- and mid-frequency bands, the maximum achievable PTE is limited to the system application and its spatial requirements. Adding ferrite cores to the Tx/Rx coil pair is considered as a solution to enable maximising PTE to the desired level.

In this chapter the analytical model of a ferrite-cored coil (FCC) is presented. With respect to the FCC's analytical model, a typical RIPT system operating at 1.06 MHz is exemplified to theoretically investigate the effects of adding ferrite cores (i.e.: magnetisation and demagnetisation effects.) on PTE. Considering these effects, an advanced iterative design algorithm is developed which maximises the PTE for the RIPT application and its requirements. Design examples of two nominal RIPT systems at resonant frequencies of 300 kHz and 10 kHz are used to theoretically investigate functionality of the advanced design algorithm, with successful results achieved.

The FCC geometry design method was validated by developing two prototype Tx/Rx FCC pairs with real-world applications, operating over low- and mid-frequency bands (i.e.: 50 kHz and 15 kHz.). Measurements presented from the Tx/Rx FCC pair in the RIPT link

operating at $50\,\text{kHz}$ show a difference of 0.75% between practical and calculated PTE values. Also, in the prototyped Tx/Rx FCC geometry which is designed for the RIPT link operating at $15\,\text{kHz}$, the calculated and measured PTE values are around 2% of each other. The remarkable correlation between the measured and calculated PTE values of the prototyped RIPT systems validate the advanced FCC design process over the low- and mid-frequency bands.

CHAPTER 6

CONCLUSION & FUTURE SCOPE

In this chapter, the results and scientific contributions of this thesis are summarised. This chapter also includes suggestions for future research areas which can lead to further development of resonant inductive power transmission and promote employment of WPT in a wider range of applications.

6.1 Conclusion

Wireless power transfer refers to cordless delivery of electrical energy from a power source to a target electric load. WPT techniques can be classified as near-field and far-field energy delivery approaches, which are extensively reviewed in chapter 2. In comparing these two techniques, it is shown that NF-WPT methods are more suitable for cordless energy delivery to electric-driven devices. Between different near-field WPT techniques, resonant inductive power transfer can provide the highest PTE level. Over the last two decades RIPT has been adapted for a wide range of NF-WPT applications [6, 8, 38].

The key challenge in development work on RIPT systems is maximising power transfer efficiency [1, 30]. In RIPT systems, PTE is influenced by:

- The inductive linkage between the Tx and Rx;

- The terminating circuitry at the primary and the secondary sides;

- The Tx/Rx coil geometry.

The available methods to maximise PTE with respect to these three impacting factors are comprehensively reviewed in chapter 2.

The RIPT systems usually operate at low- and mid-frequency bands [8, 12, 21, 35]. An efficient inductive power transmission at these frequency ranges necessitates employing a

physically large Tx/Rx coil pair. Utilising such coils with the associated energy loss inside the winding, significantly reduces the system PTE. Hence, geometrically optimising the Tx and Rx coils is an essential requirement when designing an efficient RIPT link [30–32, 39–43].

This thesis reports on a novel iterative algorithm developed for the geometrical design of Tx/Rx air-cored coil pairs, which yield maximum PTE in a RIPT system for use in applications with spatial limitations. Adding a ferrite core to the designed Tx/Rx air-cored coil pair can assist in increasing the system PTE to a desired level, especially in applications with highly restrictive spatial limitations. Hence, this thesis also provides an advanced iterative algorithm to design the geometrically optimum ferrite-cored coil pair which can further increase PTE to the desired level. The summary and results of these two design algorithms will be discussed further in sections (6.1.1) and (6.1.2).

6.1.1   The Optimum Air-cored Coil Geometry

Much work has been devoted to design the geometrically optimum Tx/Rx air-cored coil which can maximise PTE of the resonant inductive link's PTE [20, 21, 30, 31, 39–43, 56, 85, 101, 105–112]. A comprehensive review of these approaches has been included in chapter 2. The conventional geometry design techniques consider increasing Tx/Rx coil Q_i-factor as a means of maximising PTE [105–108]. Employing a Tx/Rx ACC pair with higher Q_i-factor can improve the energy transmission between the coils, however maximising the system's overall PTE requires compensating the loading effects of transmitter and receiver circuitries as well [113].

To maximise the source-to-load PTE, various iterative design algorithms have been proposed. In the conventional geometry optimisation algorithms, as a common approach, the equation for PTE is found based on RIPT system parameters (e.g.: K, R_s, R_L, etc.). Then, based on the derived PTE equation various design parameters (i.e.: FoM parameters.) are defined to help improve PTE. In these techniques, designing the optimum coil geometry,

which can maximise PTE, requires determining a proper numerical value for the set of FoM parameters. Depending on the number of FoMs, the available geometry design techniques are very time consuming [20, 31]. This research work has developed a method which builds upon previous techniques and accelerates the process of identifying the optimum Tx/Rx coil geometry. The key advancement in this work is the reduction in the number of design parameters to one, thus reducing the design complexity.

To determine the unique FoM parameter, which can maximise PTE, an analytical investigation of the RIPT system is necessary. Chapter 3 presents the physical parameters affecting PTE of the resonant inductive link. For this purpose, the analytical model to calculate L and R of the Tx/Rx ACC pair has been expressed. It should be noted that the previously reported geometry design techniques in the literature mainly focus on miniaturising spiral coils or low power (i.e.: $\ll 1$ W.) mm-sized solenoids. To fill the knowledge gap, this thesis focuses on designing the optimum Tx/Rx solenoid, which can be used for high-power (i.e.: $\geq$ several hundreds mW.) applications as well as for low-power RIPT systems.

Based on the equivalent model for the Tx/Rx ACC pair, the circuit model representing the RIPT system has been developed to investigate the requirements for a maximised resonant coupling. It is shown that maximising PTE in a resonant inductive link demands employing a series-series (SS) compensated RIPT system, given that only SS compensation provides a reactance-free link (i.e.: zero existence of reactive power in the link.) at f_o. For the considered SS-compensated inductive link the PTE equation is derived in chapter 3. From the derived equations it is concluded that maximising PTE requires a strong magnetic linkage between the Tx and Rx. In a RIPT system, having a strong magnetic resonant coupling demands an inductive link with high K value, Tx/Rx circuitry with high Q_L-factor and high quality Tx/Rx coils.

In chapter 3 of this dissertation, a unique figure-of-merit is developed by combining the PTE's affecting parameters. The new FoM parameter (P_{scf}) is called strong coupling

factor since its value indicates how strongly the Tx and Rx are linked together. The strong coupling factor is defined as $P_{scf} = K^2 Q_{L_p} Q_{L_s}$ and provides a guideline for designing the optimum Tx/Rx ACC geometry which can maximise the RIPT system's PTE. Designing the optimum ACC geometry requires identifying the numerical value of P_{scf} with respect to the RIPT application and its spatial limitations. Finding the most favourable numerical value for the FoM parameter demands analysing the effect of P_{scf} on PTE and the ACC's parasitic resistance, R. It should be noted that the value of R impacts the coil's physical size and the system's R_{L_O}.

In chapter 4, a typical RIPT system has been considered to analyse the effects of three typical investigative P_{scf} values on the coil's geometrical parameters, R_{L_O} and PTE. With respect to the impact of P_{scf} on the Tx/Rx ACC geometry and the RIPT link, a novel iterative design algorithm is developed in chapter 4 (i.e.: Fig. 4.4.) to assist in selecting the most favourable FoM value. The developed design algorithm in Fig. 4.4, through selecting the proper P_{scf} value, will provide an optimum Tx/Rx ACC geometry which maximises PTE for the required RIPT application.

Design examples of two nominal RIPT systems, operating at resonant frequencies of $300\,\text{kHz}$ (i.e.: mid-frequency.) and $10\,\text{kHz}$ (i.e.: low-frequency.), are used in chapter 4 to theoretically investigate the iterative design algorithm over the low- and mid-frequency bands. The theoretical results showed successful functionality of the novel design procedure. The ACC geometry design method is practically validated by developing four prototype Tx/Rx ACC pairs, operating over low- and mid-frequency bands (i.e.: $1.06\,\text{MHz}$, $100\,\text{kHz}$, $50\,\text{kHz}$ and $15\,\text{kHz}$.). PTE measurements from the practical setups across these frequencies are presented which closely follow the calculated PTE values. The correlation between the measured and calculated PTE values of all four prototyped RIPT systems validates the novel ACC geometry design process over these bands.

6.1.2   The Optimum Ferrite-cored Coil Geometry

In a resonant IPT system maximum achievable PTE is affected by the system application and its spatial limitations. Adding ferrite cores to the Tx/Rx ACC pair enables further enhancement of PTE. In a RIPT system with a Tx/Rx FCC pair, PTE is influenced by ferrite's magnetisation and demagnetisation effects. The ferrite's magnetisation effect enhances the Tx/Rx coil's self-inductance; hence, boosts the inductive link's PTE. On the contrary, ferrite's demagnetisation effect leads to a significant power loss inside the core and as a result reduces PTE. Thus in a RIPT system the challenge in adopting a Tx/Rx FCC pair is to design the optimum geometry which can maximise PTE with regards to ferrite's magnetisation and demagnetisation effects.

Designing the optimum FCC geometry demands having the analytical model to calculate FCC's self-inductance (L_{wf}) and parasitic resistance (R_{wf}), which has been expressed in chapter 5. From the FCC's analytical model, an observation is that L_{wf} and R_{wf} are highly influenced by the ACC's L and R. Hence, finding the optimal geometry for the Tx/Rx ferrite-cored coils requires having the optimum Tx/Rx ACC geometry (i.e.: optimum winding geometry.). As shown by numerical investigations in chapter 5, designing the optimum FCC pair also necessitates to verify if adding ferrite cores to the optimised Tx/Rx windings can maximise the RIPT system's PTE. Considering these requirements, various methods have been employed, in the literature [21, 27, 44, 47, 50–54], to design the optimum FCC geometry. A common technique is to initially design the optimum winding geometry and add ferrite core to the designed ACC pair. In the next step then the FCC geometry is adjusted to achieve a maximised PTE. Building upon the previous techniques, chapter 5 of this research work provides an advanced iterative algorithm to design the optimum FCC geometry, which maximises PTE with respect to the ferrite's magnetisation and demagnetisation effects. The advanced FCC design algorithm is developed based on the novel iterative algorithm, which is provided in chapter 4 to design the optimum air-cored solenoid pair.

In chapter 5, design examples of two nominal RIPT systems operating at resonant frequencies of $300\,\text{kHz}$ and $10\,\text{kHz}$ are presented to numerically analyse the advanced FCC design process over the low- and mid-frequency bands. The FCC geometries designed for these systems and their achievable maximum PTEs proved successful functionality of the advanced iterative algorithm. From the theoretical results it is also deduced that the FCC design process can reduce the system's physical size in addition to maximising PTE. To practically validate the advanced FCC design technique, two prototype Tx/Rx ferrite-cored solenoids are developed, which operate over low- and mid-frequency bands (i.e.: $50\,\text{kHz}$ and $15\,\text{kHz.}$). For both the prototyped RIPT setups, the calculated and practically measured PTE values are within 3% difference. This remarkable correlation validates the advanced FCC geometry design technique over the low- and mid-frequency bands.

6.1.3   Discussion

It is worth mentioning that the prototyped systems, which are used to validate functionality of the developed coil geometry design techniques (i.e.: design examples in sections (4.3.1) – (4.3.4) and (5.5.1) – (5.5.2).), are all selected from real-world RIPT applications. Hence, it can be concluded that the work undertaken in this thesis on development of a comprehensive method to design the optimum Tx/Rx coil geometry benefits industrial NF-WPT systems with reducing the application's physical size and improving its achievable PTE. It is expected that facilitating the existing WPT applications can encourage more industries to deliver/employ wire-free products.

6.2   Possible Future Research Directions

There are many research areas for further development of RIPT systems. From the author's perspective some of the future research directions in this area may include:

- Maximising PTE is a major challenge in RIPT systems. Recent investigations have considered employing metamaterials to further improve the RIPT system's PTE.

Metamaterials concentrate the Tx magnetic field on the Rx to enhance the magnetic flux density at the receiver, which yields a PTE improvement. There are works focusing on placing one-dimensional, 2-D and 3-D metamaterial slabs inside/outside the RIPT link. However, these studies are in early stages and further analysis and practical developments are still required. Further research is required to investigate the possibility of combining metamaterials with other techniques which also focus on enhancing PTE, such as designing optimum ACC and FCC geometries.

- Simultaneous power transmission to multi receivers has recently received much attention. Enhancement of multi-receiver RIPT systems can benefit different applications including WPT to household appliances in smart homes. Developing and constructing a physically compact RIPT system is a basic requirement for further development of the multi-receiver systems. The coil geometry design technique developed in this thesis could be studied further for RIPT to multi-receiver systems.

- With a significant increase in RIPT applications different industrial standards have been introduced to regulate operation of WPT systems; this can cause confusion with manufacturers and customers. Further investigations are required to develop a universal standard that can cover all the requirements in future WPT systems.

APPENDIX A

Finding the load range where η of the resonant IPT system stays within $X\%$ of the maximum achievable PTE requires solving the following inequality:

$$\eta \geq (1 - X)\,\eta_{max}\,. \tag{A.1}$$

Maximum PTE (i.e.: η_{max}.) can be achieved by substituting R_L with R_{L_O} in equation (3.17); hence, (A. 1) can be restated as:

$$
\begin{aligned}
&R_L(R_{L_O} + R)[(R_s + R)(R_{L_O} + R) + \omega_o^2 M^2] \\
&- (1 - X)R_{L_O}(R_L + R)[(R_s + R)(R_L + R) + \omega_o^2 M^2] \geq 0\,.
\end{aligned}
\tag{A.2}
$$

Rearranging (A. 2) based on R_L gives:

$$P_1 R_L^2 + P_2 R_L + P_3 \geq 0 \tag{A.3}$$

where;

$$
\begin{aligned}
P_1 =\ & -(1 - X)(R + R_s)R_{L_O} \\
P_2 =\ & (R + R_s)R_{L_O}^2 + (R + R_s)R^2 + 2RR_{L_O} + (X + 1)\omega_o^2 M^2 R R_{L_O} \\
& + 2(X - 1)R_{L_O}R^2 + 2(X - 1)R R_s R_{L_O} \\
P_3 =\ & (X - 1)(R + R_s)R_{L_O}R^2 + (X - 1)\omega_o^2 M^2 R R_{L_O}\,.
\end{aligned}
$$

Solving (A. 3) for R_L yields:

$$\alpha \leq R_L \leq \beta$$

where;

$$\alpha = \frac{-P_2 + \sqrt{(P_2)^2 - 4P_1P_3}}{2P_1} \tag{A.4}$$

$$\beta = \frac{-P_2 - \sqrt{(P_2)^2 - 4P_1P_3}}{2P_1} . \tag{A.5}$$

The circuit model for a series-series compensated RIPT system is shown in Fig. B. 1. The inductive link presented in Fig. B. 1 is similar to the RIPT system depicted in Fig. 3.4a, where the model of Tx/Rx air-cored coil pair has been replaced by its equivalent ferrite-cored coil model.

For the considered RIPT link the power transfer efficiency can be found as:

$$\eta_{\text{wf}} = \frac{R_L(\omega_o K L_{\text{wf}})^2}{(R_L + R_{\text{wf}})\left[(R_s + R_{\text{wf}})(R_L + R_{\text{wf}}) + (\omega_o K L_{\text{wf}})^2\right]}. \tag{B. 1}$$

The PTE equation presented in (B. 1) is the same as equation (3.17) where L and R have been substituted with L_{wf} and R_{wf} respectively.

By differentiating η_{wf} with respect to R_L the optimum load value which maximises PTE can be expressed as:

$$R_{L_{O_{\text{wf}}}} = R_{\text{wf}}\sqrt{1 + \frac{(\omega_o K L_{\text{wf}})^2}{R_{\text{wf}}(R_{\text{wf}} + R_s)}}. \tag{B. 2}$$

Also, finding the load range where η_{wf} of the resonant IPT system stays within $X\%$ of
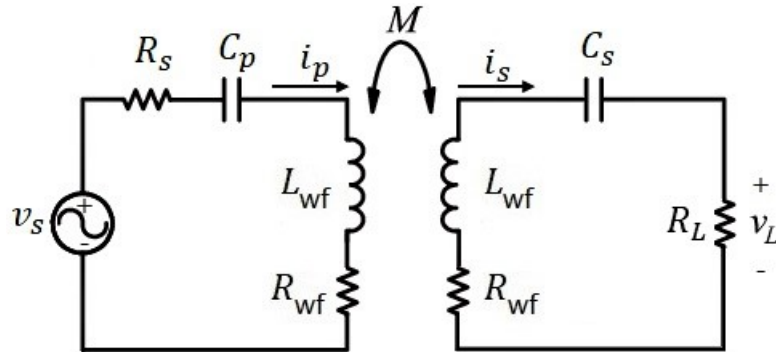

Figure B. 1: Configuration of a series-series compensated resonant IPT system with Tx/Rx ferrite-cored coils.

the maximum achievable PTE requires solving the following inequality:

$$\eta_{\text{wf}} \geq (1 - X)\,\eta_{max_{\text{wf}}}.$$ (B. 3)

Maximum PTE (i.e.: $\eta_{max_{\text{wf}}}$.) can be achieved by substituting R_L with $R_{L_{O_{\text{wf}}}}$ in equation (B. 1); hence, (B. 3) can be restated as:

$$
\begin{aligned}
& R_L(R_{L_{O_{\text{wf}}}} + R_{\text{wf}})[(R_s + R_{\text{wf}})(R_{L_{O_{\text{wf}}}} + R_{\text{wf}}) + (\omega_o K L_{\text{wf}})^2] \\
& - (1 - X)R_{L_{O_{\text{wf}}}}(R_L + R_{\text{wf}})[(R_s + R_{\text{wf}})(R_L + R_{\text{wf}}) + (\omega_o K L_{\text{wf}})^2] \geq 0 .
\end{aligned}
$$ (B. 4)

Rearranging (B. 4) based on R_L gives:

$$U_1 R_L^2 + U_2 R_L + U_3 \geq 0$$ (B. 5)

where;

$$
\begin{aligned}
U_1 = {}& -(1 - X)(R_{\text{wf}} + R_s)R_{L_{O_{\text{wf}}}} \\
U_2 = {}& (R_{\text{wf}} + R_s)R_{L_{O_{\text{wf}}}}^2 + (R_{\text{wf}} + R_s)R_{\text{wf}}^2 + 2R_{\text{wf}}R_{L_{O_{\text{wf}}}} + 2(X - 1)R_{L_{O_{\text{wf}}}}R_{\text{wf}}^2 \\
& + (X + 1)(\omega_o K L_{\text{wf}})^2 R_{\text{wf}}R_{L_{O_{\text{wf}}}} + 2(X - 1)R_{\text{wf}}R_s R_{L_{O_{\text{wf}}}} \\
U_3 = {}& (X - 1)(R_{\text{wf}} + R_s)R_{L_{O_{\text{wf}}}}R_{\text{wf}}^2 + (X - 1)(\omega_o K L_{\text{wf}})^2 R_{\text{wf}}R_{L_{O_{\text{wf}}}} .
\end{aligned}
$$

Solving (B. 5) for R_L yields:

$$\alpha_{\text{wf}} \leq R_L \leq \beta_{\text{wf}}$$

where;

$$\alpha_{\text{wf}} = \frac{-U_2 + \sqrt{(U_2)^2 - 4U_1 U_3}}{2U_1}$$ (B. 6)

$$\beta_{\text{wf}} = \frac{-U_2 - \sqrt{(U_2)^2 - 4U_1 U_3}}{2U_1} .$$ (B. 7)

REFERENCES

[1] Zhen Zhang et al. "Wireless power transfer—An overview". In: *IEEE Transactions on Industrial Electronics* 66.2 (2018), pp. 1044–1058.

[2] DM Vilathgamuwa and JPK Sampath. "Wireless power transfer (WPT) for electric vehicles (EVS)—Present and future trends". In: *Plug in electric vehicles in smart grids*. Springer, 2015, pp. 33–60.

[3] Wei Chen Cheah, Simon Andrew Watson, and Barry Lennox. "Limitations of wireless power transfer technologies for mobile robots". In: *Wireless Power Transfer* 6.2 (2019), pp. 175–189.

[4] Young-Sik Seo et al. "Wireless power transfer by inductive coupling for implantable batteryless stimulators". In: *2012 IEEE/MTT-S International Microwave Symposium Digest*. IEEE. 2012, pp. 1–3.

[5] Vinodkumar Etacheri et al. "Challenges in the development of advanced Li-ion batteries: a review". In: *Energy and Environmental Science* 4.9 (2011), pp. 3243–3262.

[6] S.Y. Ron Hui. "Magnetic Resonance for Wireless Power Transfer [A Look Back]". In: *IEEE Power Electronics Magazine* 3.1 (2016), pp. 14–31.

[7] Jaime Garnica, Raul A Chinga, and Jenshan Lin. "Wireless power transmission: From far field to near field". In: *Proceedings of the IEEE* 101.6 (2013), pp. 1321–1331.

[8] Shu Yuen Ron Hui, Wenxing Zhong, and Chi Kwan Lee. "A critical review of recent progress in mid-range wireless power transfer". In: *IEEE Transactions on Power Electronics* 29.9 (2013), pp. 4500–4511.

[9] M. Heidarian, S. J. Burgess, and R. Prabhu. "Improving the Design Approach to Developing Through-Metal Communications for Use in Subsea Pipeline Robots". In: *Global Oceans 2020: Singapore – U.S. Gulf Coast*. 2020, pp. 1–5.

[10] Michael J Moser and Hubert Zangl. "Temperature and pressure monitoring of a whipped cream device". In: *SENSORS, 2009 IEEE*. IEEE. 2009, pp. 683–686.

[11] Santhakumar Sampath et al. "A Real-Time, Non-Contact Method for In-Line Inspection of Oil and Gas Pipelines Using Optical Sensor Array". In: *Sensors* 19.16 (2019), p. 3615.

[12] Nathan Seongheon Jeong and Francesco Carobolante. "Wireless charging of a metal-body device". In: *IEEE Transactions on Microwave Theory and Techniques* 65.4 (2017), pp. 1077–1086.

[13] SY Hui. "Planar wireless charging technology for portable electronic products and Qi". In: *Proceedings of the IEEE* 101.6 (2013), pp. 1290–1301.

[14] Mingzhao Song, Pavel Belov, and Polina Kapitanova. "Wireless power transfer inspired by the modern trends in electromagnetics". In: *Applied physics reviews* 4.2 (2017), p. 021102.

[15] Valner J Brusamarello et al. "Power transfer with an inductive link and wireless tuning". In: *IEEE Transactions on Instrumentation and Measurement* 62.5 (2013), pp. 924–931.

[16] Alexey Filimonov and Andrey Somov. "Wireless power transfer to the sensors integrated in a wall". In: *2018 IEEE Industrial Cyber-Physical Systems (ICPS)*. IEEE. 2018, pp. 664–669.

[17] Xin Tan, Zhi Sun, and Pu Wang. "On localization for magnetic induction-based wireless sensor networks in pipeline environments". In: *2015 IEEE International Conference on Communications (ICC)*. IEEE. 2015, pp. 2780–2785.

[18] Chwei-Sen Wang, Oskar H Stielau, and Grant A Covic. "Design considerations for a contactless electric vehicle battery charger". In: *IEEE Transactions on industrial electronics* 52.5 (2005), pp. 1308–1314.

[19] Saleh Aghajan-Eshkevari et al. "Charging and Discharging of Electric Vehicles in Power Systems: An Updated and Detailed Review of Methods, Control Structures, Objectives, and Optimization Methodologies". In: *Sustainability* 14.4 (2022), p. 2137.

[20] Jesús Sallán et al. "Optimal design of ICPT systems applied to electric vehicle battery charge". In: *IEEE Transactions on Industrial Electronics* 56.6 (2009), pp. 2140–2149.

[21] Jiseong Kim et al. "Coil design and shielding methods for a magnetic resonant wireless power transfer system". In: *Proceedings of the IEEE* 101.6 (2013), pp. 1332–1342.

[22] Zhaocai Liu and Ziqi Song. "Robust planning of dynamic wireless charging infrastructure for battery electric buses". In: *Transportation Research Part C: Emerging Technologies* 83 (2017), pp. 77–103.

[23]   Hooman Kazemi, Keisuke Shinohara, and Curtis W Eckhardt. "Millimeter wave wireless power transmission-technologies and applications". In: *2019 IEEE Wireless Power Transfer Conference (WPTC)*. IEEE. 2019, pp. 282–286.

[24]   Candido Duarte et al. "A study on load modulation for underwater wireless power transfer". In: *OCEANS 2017-Aberdeen*. IEEE. 2017, pp. 1–4.

[25]   Junichi Sugiura and Stephen Jones. *Inductive coupling*. US Patent 10,119,343. 2018.

[26]   BA Potter and SA Shirsavar. "Design, implementation and characterisation of a contactless power transfer system for rotating applications". In: *IECON 2006-32nd Annual Conference on IEEE Industrial Electronics*. IEEE. 2006, pp. 2168–2173.

[27]   Jinyang Gao et al. "Design and testing of a motor-based capsule robot powered by wireless power transmission". In: *IEEE/ASME Transactions on Mechatronics* 21.2 (2015), pp. 683–693.

[28]   Zhi Yang, Wentai Liu, and Eric Basham. "Inductor modeling in wireless links for implantable electronics". In: *IEEE Transactions on Magnetics* 43.10 (2007), pp. 3851–3860.

[29]   Adrian E Rendon-Nava et al. "Study of the effect of distance and misalignment between magnetically coupled coils for wireless power transfer in intraocular pressure measurement". In: *The Scientific World Journal* 2014 (2014).

[30]   Uei-Ming Jow and Maysam Ghovanloo. "Design and optimization of printed spiral coils for efficient transcutaneous inductive power transmission". In: *IEEE Transactions on biomedical circuits and systems* 1.3 (2007), pp. 193–202.

[31]   Yuhua Cheng, Gaofeng Wang, and Maysam Ghovanloo. "Analytical modeling and optimization of small solenoid coils for millimeter-sized biomedical implants". In: *IEEE Transactions on Microwave Theory and Techniques* 65.3 (2016), pp. 1024–1035.

[32]   Hao Jiang et al. "A low-frequency versatile wireless power transfer technology for biomedical implants". In: *IEEE transactions on biomedical circuits and systems* 7.4 (2012), pp. 526–535.

[33]   A. Alemaryeen and S. Noghanian. "On-Body Low-Profile Textile Antenna With Artificial Magnetic Conductor". In: *IEEE Transactions on Antennas and Propagation* 67.6 (2019), pp. 3649–3656.

[34] Pyungwoo Yeon et al. "Optimal design of passive resonating wireless sensors for wearable and implantable devices". In: *IEEE Sensors Journal* 19.17 (2019), pp. 7460–7470.

[35] Alessandra Costanzo and Diego Masotti. "Energizing 5G: Near-and far-field wireless energy and data trantransfer as an enabling technology for the 5G IoT". In: *IEEE Microwave Magazine* 18.3 (2017), pp. 125–136.

[36] Marian P Kazmierkowski and Artur J Moradewicz. "Unplugged but connected: Review of contactless energy transfer systems". In: *IEEE Industrial Electronics Magazine* 6.4 (2012), pp. 47–55.

[37] Wenxing Zhong, Chi Kwan Lee, and SY Ron Hui. "General analysis on the use of Tesla's resonators in domino forms for wireless power transfer". In: *IEEE transactions on industrial electronics* 60.1 (2011), pp. 261–270.

[38] Grant A Covic and John T Boys. "Inductive power transfer". In: *Proceedings of the IEEE* 101.6 (2013), pp. 1276–1289.

[39] Ahmed Ibrahim and Mehdi Kiani. "A figure-of-merit for design and optimization of inductive power transmission links for millimeter-sized biomedical implants". In: *IEEE transactions on biomedical circuits and systems* 10.6 (2016), pp. 1100–1111.

[40] Mehdi Kiani and Maysam ghovanloo. "A figure-of-merit for designing high-performance inductive power transmission links". In: *IEEE Transactions on Industrial Electronics* 60.11 (2013), pp. 5292–5305.

[41] Mehdi Kiani, Uei-Ming Jow, and Maysam Ghovanloo. "Design and optimization of a 3-coil inductive link for efficient wireless power transmission". In: *IEEE transactions on biomedical circuits and systems* 5.6 (2011), pp. 579–591.

[42] Peilong Feng et al. "Chip-scale coils for millimeter-sized bio-implants". In: *IEEE transactions on biomedical circuits and systems* 12.5 (2018), pp. 1088–1099.

[43] Dukju Ahn and Maysam Ghovanloo. "Optimal design of wireless power transmission links for millimeter-sized biomedical implants". In: *IEEE transactions on biomedical circuits and systems* 10.1 (2015), pp. 125–137.

[44] Yuhua Cheng et al. "Analytical Modeling of Small, Solenoidal, and Implantable Coils With Ferrite Tube Core". In: *IEEE Microwave and Wireless Components Letters* 29.3 (2019), pp. 237–239.

[45] Constantine A Balanis. *Advanced engineering electromagnetics*. John Wiley and Sons, 2012.

[46] Klaus Finkenzeller. *RFID handbook: fundamentals and applications in contactless smart cards, radio frequency identification and near-field communication*. John wiley and sons, 2010.

[47] Mickel Budhia, Grant A Covic, and John T Boys. "Design and optimisation of magnetic structures for lumped inductive power transfer systems". In: *2009 IEEE Energy Conversion Congress and Exposition*. IEEE. 2009, pp. 2081–2088.

[48] Masato Yamakawa et al. "Wireless power transmission into a space enclosed by metal walls using magnetic resonance coupling". In: *Wireless Engineering and Technology* 2014 (2014).

[49] Tuan Anh Vu et al. "Wireless power transfer through metal using inductive link". In: *International Journal of Power Electronics and Drive Systems (IJPEDS)* 10.4 (2019).

[50] Jiangfeng Wu and Kamal Sarabandi. "Super-miniaturized MF antenna for borehole". In: *2013 IEEE Antennas and Propagation Society International Symposium (APSURSI)*. IEEE. 2013, pp. 1386–1387.

[51] Changbyung Park et al. "Innovative 5-m-off-distance inductive power transfer systems with optimally shaped dipole coils". In: *IEEE transactions on power electronics* 30.2 (2014), pp. 817–827.

[52] Roman Bosshard et al. "Modeling and η - α -Pareto Optimization of Inductive Power Transfer Coils for Electric Vehicles". In: *IEEE Journal of Emerging and Selected Topics in Power Electronics* 3.1 (2015), pp. 50–64.

[53] Meng Wang et al. "Demagnetization weakening and magnetic field concentration with ferrite core characterization for efficient wireless power transfer". In: *IEEE Transactions on Industrial Electronics* 66.3 (2018), pp. 1842–1851.

[54] Zhongyu Dai et al. "Optimal design of magnetic coupling wireless power supply system for monitoring equipment". In: *IEEE Access* 6 (2018), pp. 58600–58608.

[55] Marinos N Vouvakis et al. "Ferrite-loaded cavity-backed antennas including nonuniform and nonlinear magnetization effects". In: *IEEE Transactions on Antennas and Propagation* 51.5 (2003), pp. 1000–1010.

[56] Young Jin Hwang and Jae Young Jang. "Design and Analysis of a Novel Magnetic Coupler of an In-Wheel Wireless Power Transfer System for Electric Vehicles". In: *Energies* 13.2 (2020), p. 332.

[57] Gabriele Grandi et al. "Model of laminated iron-core inductors for high frequencies". In: *IEEE Transactions on magnetics* 40.4 (2004), pp. 1839–1845.

[58] Paul T Theilmann and Peter M Asbeck. "An analytical model for inductively coupled implantable biomedical devices with ferrite rods". In: *IEEE transactions on biomedical circuits and systems* 3.1 (2008), pp. 43–52.

[59] Qin Yu, Thomas W Holmes, and Krishna Naishadham. "RF equivalent circuit modeling of ferrite-core inductors and characterization of core materials". In: *IEEE Transactions on Electromagnetic Compatibility* 44.1 (2002), pp. 258–262.

[60] Constantine A Balanis. *Antenna theory: analysis and design*. John wiley and sons, 2016.

[61] Mohammed H Alsharif et al. "Toward 6G communication networks: Terahertz frequency challenges and open research issues". In: *Computers, Materials and Continua* 66.3 (2021), pp. 2831–2842.

[62] Andre Kurs et al. "Wireless power transfer via strongly coupled magnetic resonances". In: *science* 317.5834 (2007), pp. 83–86.

[63] "IEEE Standard for Safety Levels with Respect to Human Exposure to Radio Frequency Electromagnetic Fields, 3 kHz to 300 GHz". In: *IEEE Std C95.1-2005 (Revision of IEEE Std C95.1-1991)* (2006), pp. 1–238.

[64] Qingwen Liu et al. "Charging unplugged: Will distributed laser charging for mobile wireless power transfer work?" In: *IEEE Vehicular Technology Magazine* 11.4 (2016), pp. 36–45.

[65] Maurice GL Roes et al. "Acoustic energy transfer: A review". In: *IEEE Transactions on Industrial Electronics* 60.1 (2012), pp. 242–248.

[66] David J Graham, Jeffrey A Neasham, and Bayan S Sharif. "Investigation of methods for data communication and power delivery through metals". In: *IEEE Transactions on industrial electronics* 58.10 (2011), pp. 4972–4980.

[67] Sadeque Reza Khan et al. "Wireless Power Transfer Techniques for Implantable Medical Devices: A Review". In: *Sensors* 20.12 (2020), p. 3487.

[68] Michael P Theodoridis. "Effective capacitive power transfer". In: *IEEE Transactions on Power Electronics* 27.12 (2012), pp. 4906–4913.

[69] Susanna Vital de Campos de Freitas et al. "Contactless power transfer using capacitive resonant single-conductor structure". In: *2018 IEEE Wireless Power Transfer Conference (WPTC)*. IEEE. 2018, pp. 1–4.

[70] Aqeel Mahmood Jawad et al. "Opportunities and challenges for near-field wireless power transfer: A review". In: *Energies* 10.7 (2017), p. 1022.

[71] Liang Huang et al. "An overview of capacitively coupled power transfer—A new contactless power transfer solution". In: *2013 IEEE 8th conference on industrial electronics and applications (ICIEA)*. IEEE. 2013, pp. 461–465.

[72] WX Zhong and SYR Hui. "Maximum energy efficiency tracking for wireless power transfer systems". In: *IEEE Transactions on Power Electronics* 30.7 (2014), pp. 4025–4034.

[73] Umar Azad, Hengzhen Crystal Jing, and Yuanxun Ethan Wang. "Link budget and capacity performance of inductively coupled resonant loops". In: *IEEE transactions on antennas and propagation* 60.5 (2012), pp. 2453–2461.

[74] JC Schuler. "High-level electromagnetic energy transfer through a closed chest wall". In: *IRE International Conv. Rec. pt 9* 9 (1961), pp. 119–126.

[75] Aristeidis Karalis, John D Joannopoulos, and Marin Soljačić. "Efficient wireless non-radiative mid-range energy transfer". In: *Annals of physics* 323.1 (2008), pp. 34–48.

[76] Meysam Zargham and P Glenn Gulak. "Maximum achievable efficiency in near-field coupled power-transfer systems". In: *IEEE Transactions on Biomedical Circuits and Systems* 6.3 (2012), pp. 228–245.

[77] Michael J Moser and Hubert Zangl. "Temperature and pressure monitoring of a whipped cream device". In: *SENSORS, 2009 IEEE*. IEEE. 2009, pp. 683–686.

[78] Nathan S Jeong and Francesco Carobolante. "Enabling wireless power transfer though a metal encased handheld device". In: *2016 IEEE Wireless Power Transfer Conference (WPTC)*. IEEE. 2016, pp. 1–3.

[79] Susanna Vital de Campos de Freitas et al. "A novel method for data and power transmission through metallic structures". In: *IEEE Transactions on Industrial Electronics* 64.5 (2016), pp. 4027–4036.

[80] Hongzhi Guo and Kyo D Song. "Reliable Through-Metal Wireless Communication Using Magnetic Induction". In: *IEEE Access* 7 (2019), pp. 115428–115439.

[81] Wenxing Zhong and SYR Hui. "Maximum energy efficiency operation of series-series resonant wireless power transfer systems using on-off keying modulation". In: *IEEE Transactions on Power Electronics* 33.4 (2017), pp. 3595–3603.

[82] Abdul Basir and Hyoungsuk Yoo. "Efficient Wireless Power Transfer System With a Miniaturized Quad-Band Implantable Antenna for Deep-Body Multitasking Implants". In: *IEEE Transactions on Microwave Theory and Techniques* 68.5 (2020), pp. 1943–1953.

[83] Reem Shadid et al. "Hybrid inductive power transfer and wireless antenna system for biomedical implanted devices". In: *Progress in Electromagnetics Research C* 88 (2018), p. 77.

[84] Jaehoon Kim and Yahya Rahmat-Samii. "Implanted antennas inside a human body: Simulations, designs, and characterizations". In: *IEEE Transactions on microwave theory and techniques* 52.8 (2004), pp. 1934–1943.

[85] M. Heidarian and S. J. Burgess. "A Design Technique for Optimizing Resonant Coils and the Energy Transfer of Inductive Links". In: *IEEE Transactions on Microwave Theory and Techniques* 69.1 (2021), pp. 399–408.

[86] Alexandre Robichaud, Martin Boudreault, and Dominic Deslandes. "Comparison between inductance topologies for resonant wireless power transmission applications". In: *2012 Asia Pacific Microwave Conference Proceedings*. IEEE. 2012, pp. 397–399.

[87] Aqueel Ahmad, Mohammad Saad Alam, and Ahmed AS Mohamed. "Design and Interoperability Analysis of Quadruple Pad Structure for Electric Vehicle Wireless Charging Application". In: *IEEE Transactions on Transportation Electrification* (2019).

[88] Subhadeep Bhattacharya and YK Tan. "Design of static wireless charging coils for integration into electric vehicle". In: *2012 IEEE Third International Conference on Sustainable Energy Technologies (ICSET)*. IEEE. 2012, pp. 146–151.

[89] OdunAyo Imoru et al. "An inductive power transfer through metal object". In: *2013 1st International Future Energy Electronics Conference (IFEEC)*. IEEE. 2013, pp. 246–251.

[90] Hubert Zangl et al. "Low Frequency and High Frequency semi-active wireless sensors". In: *SENSORS, 2008 IEEE*. IEEE. 2008, pp. 534–537.

[91] David J Graham. "Investigation of methods for data communication and power delivery through metals". PhD thesis. University of Newcastle upon Tyne, Newcastle upon Tyne, UK, 2012.

[92] Chi Van Pham, Anh-Vu Pham, and Christopher S Gardner. "Development of Helical circular coils for wireless through-metal inductive power transfer". In: *2017 IEEE Wireless Power Transfer Conference (WPTC)*. IEEE. 2017, pp. 1–3.

[93] Wei Zhou et al. "Wireless power transfer across a metal barrier by combined capacitive and inductive coupling". In: *IEEE Transactions on Industrial Electronics* 66.5 (2018), pp. 4031–4041.

[94]   Young-Sik Seo et al. "Investigation of wireless power transfer in through-wall applications". In: *2012 Asia Pacific Microwave Conference Proceedings*. IEEE. 2012, pp. 403–405.

[95]   Dukju Ahn and Songcheol Hong. "A study on magnetic field repeater in wireless power transfer". In: *IEEE Transactions on Industrial Electronics* 60.1 (2012), pp. 360–371.

[96]   Yongseok Lim et al. "An adaptive impedance-matching network based on a novel capacitor matrix for wireless power transfer". In: *IEEE Transactions on Power Electronics* 29.8 (2013), pp. 4403–4413.

[97]   Jungsik Kim and Jinho Jeong. "Range-adaptive wireless power transfer using multiloop and tunable matching techniques". In: *IEEE Transactions on Industrial Electronics* 62.10 (2015), pp. 6233–6241.

[98]   Xiaofang Yu et al. "Wireless energy transfer with the presence of metallic planes". In: *Applied Physics Letters* 99.21 (2011), p. 214102.

[99]   Mohammadreza F Imani and Anthony Grbic. "Unidirectional wireless power transfer using near-field plates". In: *Journal of Applied Physics* 117.18 (2015), p. 184903.

[100]   Jaemyung Lim, Byunghun Lee, and Maysam Ghovanloo. "Optimal design of a resonance-based voltage boosting rectifier for wireless power transmission". In: *IEEE Transactions on Industrial Electronics* 65.2 (2017), pp. 1645–1654.

[101]   Maryam Heidarian et al. "Maximising Inductive Power Transmission using a Novel Analytical Coil Design Approach". In: *2019 IEEE Wireless Power Transfer Conference (WPTC)*. IEEE. 2019, pp. 158–161.

[102]   Hongchang Li et al. "Pulse density modulation for maximum efficiency point tracking of wireless power transfer systems". In: *IEEE Transactions on Power Electronics* 33.6 (2017), pp. 5492–5501.

[103]   Mehdi Kiani et al. "A Q-modulation technique for efficient inductive power transmission". In: *IEEE journal of solid-state circuits* 50.12 (2015), pp. 2839–2848.

[104]   Liqiang Yuan et al. "Maximum efficiency point tracking of the wireless power transfer system for the battery charging in electric vehicles". In: *2015 18th International Conference on Electrical Machines and Systems (ICEMS)*. IEEE. 2015, pp. 1101–1107.

[105]   Xu Huang, KDT Ngo, and G Bloom. "Design techniques for planar windings with low resistances". In: *Proceedings of 1995 IEEE Applied Power Electronics Conference and Exposition-APEC'95*. Vol. 2. IEEE. 1995, pp. 533–539.

[106]   Jan Craninckx and Michiel SJ Steyaert. "A 1.8-GHz low-phase-noise CMOS VCO using optimized hollow spiral inductors". In: *IEEE Journal of solid-state circuits* 32.5 (1997), pp. 736–744.

[107]   Samuel R Cove et al. "Improving wireless power transfer efficiency using hollow windings with track-width-ratio". In: *IEEE Transactions on Power Electronics* 31.9 (2015), pp. 6524–6533.

[108]   Yipeng Su et al. "On the relationship of quality factor and hollow winding structure of coreless printed spiral winding (CPSW) inductor". In: *IEEE transactions on Power Electronics* 27.6 (2011), pp. 3050–3056.

[109]   Farid Jolani, Yiqiang Yu, and Zhizhang Chen. "A planar magnetically coupled resonant wireless power transfer system using printed spiral coils". In: *IEEE Antennas and Wireless Propagation Letters* 13 (2014), pp. 1648–1651.

[110]   Wen H Ko, Sheau P Liang, and Cliff DF Fung. "Design of radio-frequency powered coils for implant instruments". In: *Medical and Biological Engineering and Computing* 15.6 (1977), pp. 634–640.

[111]   N de N Donaldson and TA Perkins. "Analysis of resonant coupled coils in the design of radio frequency transcutaneous links". In: *Medical and Biological Engineering and computing* 21.5 (1983), pp. 612–627.

[112]   Maryam Heidarian et al. "Optimal Coil Design for Maximum Power Transfer Efficiency in Resonantly Coupled Systems". In: *2019 USNC-URSI Radio Science Meeting (Joint with AP-S Symposium)*. IEEE. 2019, pp. 73–74.

[113]   Seung-Hwan Lee and Robert D Lorenz. "Development and validation of model for 95%-efficiency 220-W wireless power transfer over a 30-cm air gap". In: *IEEE Transactions on industry applications* 47.6 (2011), pp. 2495–2504.

[114]   Iman Ghotbi et al. "3-Coil orientation insensitive wireless power transfer for capsule endoscope". In: *2015 23rd Iranian Conference on Electrical Engineering*. IEEE. 2015, pp. 1249–1254.

[115]   C Fernandez et al. "Design issues of a core-less transformer for a contact-less application". In: *APEC. Seventeenth Annual IEEE Applied Power Electronics Conference and Exposition (Cat. No. 02CH37335)*. Vol. 1. IEEE. 2002, pp. 339–345.

[116]   Wenxing Zhong and SY Hui. "Reconfigurable wireless power transfer systems with high energy efficiency over wide load range". In: *IEEE Transactions on Power Electronics* 33.7 (2017), pp. 6379–6390.

[117]   Matthew NO Sadiku. *Elements of electromagnetics*. Oxford university press, 2018.

[118] Constantine A Balanis. *Antenna theory: analysis and design*. John wiley and sons, 2015.

[119] Youbok Lee. "RFID coil design". In: *Microchip Technol. Inc. Appl. Note* (1998).

[120] Youbok Lee et al. "Antenna circuit design for RFID applications". In: *AN710, Microchip Technology Inc* (2003).

[121] K Fujimoto et al. *Small Antennas*. John wiley and sons, 1987.

[122] Xun Liu et al. "Optimal operation of contactless transformers with resonance in secondary circuits". In: *2008 Twenty-Third Annual IEEE Applied Power Electronics Conference and Exposition*. IEEE. 2008, pp. 645–650.

[123] Nathan O Sokal and Alan D Sokal. "Class EA new class of high-efficiency tuned single-ended switching power amplifiers". In: *IEEE Journal of solid-state circuits* 10.3 (1975), pp. 168–176.

[124] Pengde Wu et al. "High-efficient rectifier with extended input power range based on self-tuning impedance matching". In: *IEEE Microwave and Wireless Components Letters* 28.12 (2018), pp. 1116–1118.

[125] Yong Huang, Naoki Shinohara, and Tomohiko Mitani. "Impedance matching in wireless power transfer". In: *IEEE Transactions on Microwave Theory and Techniques* 65.2 (2016), pp. 582–590.

[126] Chwei-Sen Wang, Grant A Covic, and Oskar H Stielau. "General stability criterions for zero phase angle controlled loosely coupled inductive power transfer systems". In: *IECON'01. 27th Annual Conference of the IEEE Industrial Electronics Society (Cat. No. 37243)*. Vol. 2. IEEE. 2001, pp. 1049–1054.

[127] Mehdi Kiani and Maysam Ghovanloo. "The circuit theory behind coupled-mode magnetic resonance-based wireless power transmission". In: *IEEE Transactions on Circuits and Systems I: Regular Papers* 59.9 (2012), pp. 2065–2074.

[128] Grant A Covic et al. "The design of a contact-less energy transfer system for a people mover system". In: *PowerCon 2000. 2000 International Conference on Power System Technology. Proceedings (Cat. No. 00EX409)*. Vol. 1. IEEE. 2000, pp. 79–84.

[129] Jongwook Kim et al. "An Efficient Modeling for Underwater Wireless Power Transfer Using Z-Parameters". In: *IEEE Transactions on Electromagnetic Compatibility* 61.6 (2019), pp. 2006–2014.

[130] David Keun Cheng et al. *Field and wave electromagnetics*. Pearson Education India, 1989.

[131] *Fair-Rite Soft Ferrites*. Wallkill, NY, USA: Fair-Rite, 2005.

[132] Gerald E Loeb et al. "BION system for distributed neural prosthetic interfaces". In: *Medical engineering & physics* 23.1 (2001), pp. 9–18.